Bidirectional embedded battery charger with V2G capabilities

Nisith Bhowmick

Communauté
UNIVERSITÉ Grenoble Alpes

THÈSE

Pour obtenir le grade de

DOCTEUR DE LA COMMUNAUTE UNIVERSITE GRENOBLE ALPES

Spécialité : **Génie Electrique**

Arrêté ministériel : 16 Décembre 2016

Présentée par

Nisith BHOWMICK

Thèse dirigée par **Seddik BACHA** et
Co-dirigée par **David FREY, Mustapha DEBBOU et Jihen SAKLY**

Préparée au sein du **Laboratoire de Génie Electrique de Grenoble (G2ELab)**
dans le cadre de **l'École Doctorale Electronique, Electrotechnique, Automatique et Traitement du Signal (EEATS)**

Chargeur de batterie réversible embarqué avec fonctionnalités V2G

Thèse soutenue publiquement le **06 April 2021**
Devant le jury composé de :

Mme. Xuefang LIN SHI
Professeur à Laboratoire Ampère Lyon, Président du jury
M. Jean-Paul GAUBERT
Professeur à Université de Poitiers, Rapporteur
M. Abdelkrim BENCHAIB
R&D Manager à Supergrid Institute Lyon, Rapporteur
M. Seddik BACHA
Professeur à l'Université Grenoble Alpes (G2Elab), Directeur de thèse
M. David FREY
Maitre de Conférences à l'Université Grenoble Alpes (G2Elab), Co-encadrant de thèse
M. Mustapha DEBBOU
Research Engineer, Thales Group, Co-encadrant de thèse
Mme. Jihen SAKLY
Research Engineer, Institut VEDECOM, Co-encadrant de thèse

Dedicated

To my parents

Acknowledgements

It is a pleasure to thank many people who have made this thesis possible. My thesis work would not have been possible without the constant support from my advisors, labmates, family members and friends.

First, I would like to thank to my PhD supervisors from G2ELab, Mr. David FREY and Mr. Seddik BACHA, who guided me with their amazing supervisions during these three years. They provided me great ideas and thoughts, and really taught me how research work should be conducted. They spent a lot of time with me despite of their busy schedule. I would also like to thank Mr. Mustapha DEBBOU, Mme. Jihen SAKLEY, Mr. Francois COLET and Mr. Christophe RIPOLL from Institut VEDECOM who guided me throughout this thesis. Then I would like to thank all the Jury members, Mme. Xuefang LIN SHI, Mr. Jean-Paul GAUBERT and Mr. Abdelkrim BENCHAIB, who carefully read this work and proposed improvements for defending the thesis.

Then, I address my deep thanks to all the members of G2ELab for advanced academic support and Institut VEDECOM for providing me financial and industrial support. Both of them gave me the opportunity to join inter-company meetings, which happened to be very helpful not only for my PhD but also for my personal achievements. Then, I would like to thank Mr. Alexis DERBEY and Mr. Benoit SARRAZIN, two engineers from G2ELab, who helped me a lot with my experimental test bench.

I would also like to thank Mr. Raphael CAIRE, Professor from Université Grenoble Alpes and Mr. Jean-Paul GAUBERT, Professor from Université de Poitiers for reviewing my progress in year of PhD through Comité de Suivi Individuel (CSI) meeting.

The best way to improve one's research work is to question it. In that sense, I would like to thank deeply to all other PhD students and Postdocs of G2ELab, namely Diana, Andressa, Uyen, Adrien, Antoine, Soleiman, Andre, Theo, Luciano, Lucas and Nasreddine. Their valuable suggestions and comments helped me a lot in improving this thesis. I would like to thank Severine, who becomes an expert in V2G technology due to our day-to-day discussion at home.

Last but not the least, I would like to thank my parents who always support me, in particular during some difficult - sometimes-lonely - moments.

Abstract

Electric Vehicles (EV) are growing at a rapid pace in transport sectors because of increasing concerns on environment. Successful and rapid integration of EVs potentially reduce CO2 emissions. However, due to high penetration in the transport sector, EVs also represent substantial challenges for the Distribution System Operator (DSO). More specifically, the low-voltage grid operation becomes challenging due to sudden demand of energy as uncontrolled EV charging may coincides with the peak load demand. Thus, it results a severe voltage deviation, if energy systems are not managed in an organized way.

Vehicle-to-Grid (V2G) is a technology, where EVs discharge their stored energy and inject that onto the grid during peak load period. Thus, it should not only be considered as passive loads but also energy sources while being in idle state. V2G technology also holds potential for providing ancillary services in energy sectors, such as, voltage regulation, voltage shaving, reactive power compensation and distributed generation. If managed properly, EV becomes an attractive asset for DSO. Thus, the battery charger of EVs should provide below functionalities:

1. Charging of battery (Primary function): In this case, power is transferred from grid to vehicle, called G2V operation.
2. Discharging of battery (Secondary function): In this case, storage unit of EV, i.e., battery is considered as energy source and power is transferred from vehicle to grid.
3. Network balancing capability (Tertiary function): EVs can provide ancillary services to the grid, such as, reactive power or unbalance current consumption/injection for helping to balance and sustain the network without additional battery cycling.

The first two functionalities had already been addressed by previous researchers (also in G2ELab by Dr. Mounir Marzouk). This thesis focuses on the mentioned third functionality that can be provided by EVs.

These three functionalities necessitate the bidirectional battery charger for EV, which is capable of sinking or sourcing real and reactive power. Power Electronics part of the EV battery charger should combines AC/DC converter for maintaining near unity power factor of the grid and DC/DC converter for regulating battery current and voltage. One of the main objectives of the thesis is to compensate and mitigate unbalance active and reactive powers exchange between supplies of the 3-phases with the help of bidirectional EV battery charger. As the charger should also be onboard type, constraints are weight and volume for developing this type of charger.

In this thesis, Neutral Point Clamp (NPC) converter and Triple Active Bridge (TAB) have been proposed and analyzed for AC/DC and DC/DC converter respectively. Objectives of this thesis have been analyzed and verified by the help of Matlab/Simulink results and Hardware-in-the-Loop (HIL) simulation results.

Résumé

Les véhicules électriques (VE) se développent à un rythme rapide dans les secteurs des transports en raison des préoccupations croissantes en matière d'environnement. L'intégration réussie et rapide des véhicules électriques réduit potentiellement les émissions de CO2. Cependant, en raison de la forte pénétration dans le secteur des transports, les véhicules électriques représentent également des défis importants pour le gestionnaire de réseau de distribution (GRD). Plus précisément, le fonctionnement du réseau basse tension devient difficile en raison d'une demande soudaine d'énergie, car la charge incontrôlée des VE peut coïncider avec la demande de charge de pointe. Ainsi, il en résulte une déviation de tension sévère, si les systèmes énergétiques ne sont pas gérés de manière organisée.

Vehicle-to-Grid (V2G) est une technologie dans laquelle les VE déchargent leur énergie stockée et l'injectent sur le réseau pendant la période de charge de pointe. Ainsi, il ne doit pas seulement être considéré comme des charges passives mais aussi comme des sources d'énergie tout en étant au repos. La technologie V2G offre également un potentiel pour fournir des services auxiliaires dans les secteurs de l'énergie, tels que la régulation de tension, le rasage de tension, la compensation de puissance réactive et la production distribuée. S'il est bien géré, EV devient un atout attractif pour DSO. Ainsi, le chargeur de batterie des VE devrait fournir les fonctionnalités ci-dessous:

1. Chargement de la batterie (fonction principale): Dans ce cas, la puissance est transférée du réseau au véhicule, appelée opération G2V.
2. Décharge de la batterie (fonction secondaire): Dans ce cas, l'unité de stockage d'EV, c'est-à-dire la batterie, est considérée comme une source d'énergie et la puissance est transférée du véhicule au réseau.
3. Capacité d'équilibrage du réseau (fonction tertiaire): les véhicules électriques peuvent fournir des services auxiliaires au réseau, tels que la puissance réactive ou le déséquilibre de la consommation / injection de courant pour aider à équilibrer et maintenir le réseau sans cyclage de batterie supplémentaire.

Les deux premières fonctionnalités avaient déjà été abordées par des chercheurs précédents (également dans G2ELab par le Dr Mounir Marzouk). Cette thèse se concentre sur la troisième fonctionnalité mentionnée qui peut être fournie par les véhicules électriques.

Ces trois fonctionnalités nécessitent le chargeur de batterie bidirectionnel pour EV, capable d'absorber ou de générer de la puissance réelle et réactive. La partie électronique de puissance du chargeur de batterie EV doit combiner un convertisseur AC / DC pour maintenir un facteur de puissance proche de l'unité du réseau et un convertisseur DC / DC pour réguler le courant et la tension de la batterie. L'un des principaux objectifs de la thèse est de compenser et d'atténuer les déséquilibres des puissances actives et réactives échangées entre les alimentations des 3 phases à l'aide d'un chargeur EV bidirectionnel. Le chargeur devant

également être de type embarqué, les contraintes sont le poids et le volume pour développer ce type de chargeur.
Dans cette thèse, le convertisseur NPC (Neutral Point Clamp) et le Triple Active Bridge (TAB) ont été proposés et analysés respectivement pour les convertisseurs AC / DC et DC / DC. Les objectifs de cette thèse ont été analysés et vérifiés à l'aide des résultats Matlab / Simulink et des résultats de simulation Hardware-in-the-Loop (HIL).

CONTENTS

Publications

Acronymes

List of Tables

List of Figures

CHAPTER 1 : Introduction

PUBLICATIONS

Conferences:

1. N. Bhowmick, D. Frey, S. Bacha, M. Debbou and F. Colet, "A Comparative Study of Capacitive Middle Point Voltage Oscillations for 3 Phase 2-Level and 3-Level Converters in Unbalanced Current Injection," *2017 IEEE Vehicle Power and Propulsion Conference (VPPC)*, 2017, pp. 1-6, doi: 10.1109/VPPC.2017.8331033.
2. Nisith Bhowmick, David Frey, Seddik Bacha, Mustapha Debbou, François Colet, "Evaluation des ondulations de tension au point milieu capacitif pour les convertisseurs à deux et à trois niveaux, " Symposium de Génie Electrique, Jul 2018, Nancy, France.

Patents:

1. M. Debbou, D. Frey, S. Bacha and N. Bhowmick, "Contrôleur de commande de convertisseur électrique et convertisseur électrique, notamment pour une intégration dans un véhicule électrique", INPI [B9] WO2020188189 (A1), 2020.
2. M. Debbou, D. Frey, N. Bhowmick, F. Collet and S. Bacha, "Convertisseur NPC Quatre Bras pour les Véhicules électriques et Chargeur bidirectionnel comprenant une tel convertisseur", INPI [B7] WO2019186078A1 (A1), 2019.

ACRONYMES

AC	*Alternative Current*
BMS	*Battery Management System*
CHB	*Cascaded H-Bridge*
CMV	*Common Mode Voltage*
DAB	*Dual Active Bridge*
DC	*Direct Current*
DSP	*Digital Signal Processor*
EV	*Electric Vehicle*
EVSE	*Electric Vehicle Supply Equipment*
FCC	*Flying Capacitor Converter*
FCEV	*Fuel Cell Electric vehicle*
FFT	*Fast Fourier Transform*
FPGA	*Field Programmable Gate Array*
GaN	*Gallium Nitride*
G2V	*Grid-to-Vehicle*
HEV	*Hybrid Electric Vehicles*
HF	*High Frequency*
HIL	*Hardware-in-the-Loop*
ICE	*Internal Combustion Engines*
IEC	*International Electrotechnical Commission*
IEEE	*Institute of Electrical and Electronics Engineers*
IGBT	*Insulated Gate Bipolar Transistor*
MOSFET	*Metal Oxide Semiconductor Field Effect Transistor*
NPC	*Neutral Point Clamp*
PDPWM	*Phase Disposition Pulse Width Modulation*
PHEV	*Plug-in Hybrid Electric Vehicles*
PI	*Proportional Integral*
PID	*Proportional Integral Derivative*
PLL	*Phase Locked Loop*
PR	*Proportional Resonant*
PSPWM	*Phase Shifted Pulse Width Modulation*
REEV	*Range Extended Electric Vehicle*
RMS	*Root Mean Square*
R&D	*Research and Development*
SiC	*Silicon Carbide*
SPWM	*Sinusoidal Pulse Width Modulation*
TAB	*Triple Active Bridge*
THD	*Total Harmonic Distortion*
VSC	*Voltage Source Converter*
V2G	*Vehicle-to-Grid*
ZCS	*Zero Current Switching*
ZVS	*Zero Voltage Switching*

List of Tables

List of Figures

Chapter 1

INTRODUCTION

This chapter introduces the general background, context and the motivation for this research. The key contributions of the thesis are also highlighted followed by the outline of the thesis.

1. General introduction

Due to industrialization and exponential increase in world population, consumption of fossil fuel is also increasing. Environmental hazards, such as, greenhouse gas emission and increase in global temperature are the effects of increased consumption of fossil fuels [1]. It draws the attention of Research and Development (R&D) community and leads the governments throughout the world to come up with policies to address this issue.

Different preventives have been taken in order to reduce greenhouse gas emission. Such as green power generation from renewable sources of energy (wind, hydro, solar, geothermal and tidal etc.) are favored, as well as more efficient methods of consumption and the storage of the generated energy are adopted [2] [3]. Electric vehicles (EVs), discussed in detail in the next section, also help nature, as they have no tailpipe emissions. In fact, they do not even have an exhaust. Considering the impact of generating the electricity used, pure EVs can still produce substantially lower greenhouse gases than petrol or diesel cars [4] [5]. These emissions will be reduced further as the world switches to more renewable and nuclear electricity generation.

1.1 Electric vehicles (EVs)

Transportation sector, depending on combustion engines, contributes to a large amount of CO_2 in the atmosphere [6]. Recently, electrification of transportation sector has caught attention worldwide as potential and promising solution for aforementioned problems. As a result, the interest in EVs has increased rapidly over the past few years and this trend seems to keep growing in near future [7]. These alternative vehicle technologies, that include Hybrid Electric Vehicles (HEVs), Plug-in HEVs (PHEVs), Range Extended EVs (REEV) and EVs, have gained popularity thanks to their advantages, such as more eco-friendly, less noisy and more efficient [8] [9].

Among all these types of EVs, HEVs are powered by the combination of electric motors and Internal Combustion Engines (ICE) [10]. Normally, the low-speed acceleration is supported by electric motor and it is powered by battery pack. The ICE, which is driven by gasoline, diesel or natural gases, is used for higher speed. During regenerative braking, the battery packs are charged by the electric motor while it is charged through the ICE during motoring. An electric outlet cannot charge these battery packs. PHEVs are also driven by the combination of electric motors and ICE. Additionally to the charging possibilities present in the HEV, the battery packs can be charged thanks to an electric outlet when the car is parked. Range Extended EVs also use both ICE and electric motor [11]. However, unlike HEVs and PHEVs, they use electric motor for all the driving cycles. The purpose of ICE is to charge the battery during low on charge. EVs use electric motors for traction purposes and are powered solely by battery packs [12]. These motors are more powerful than the motors find in HEV or PHEV. Another type of

battery operated EVs are hydrogen-powered EVs, called the Fuel Cell Electric vehicle (FCEV) [13]. FCEVs generate electric power by using O_2 from the air and compressed H_2 to drive the electric motors. In normal operation, FCEVs are 12 times more expensive than conventional gasoline powered vehicles. Many automobile manufacturers like Renault, Peugeot, Nissan, Mitsubishi, Tesla, Hyundai, BMW, Volkswagen, Volvo and Mercedes, as shown in Fig. 1.1, have at this point developed and commercialized their modern electric models, proving that the electric drive is technically viable, eco-friendly and affordable.

Fig. 1.1 Different models of EVs

Global EV outlook report 2019 reported that the global stock of electric passenger cars passed 5million in 2018 with an increase of 63% from the previous year, as shown in Fig.1.2. Market share of the EVs on road in 2018 comprises mostly by China with 45%, followed by Europe and USA with 24% and 22% respectively [14], as shown in Fig.1.3. But only a handful of countries have significant market share of EVs in transport sector.

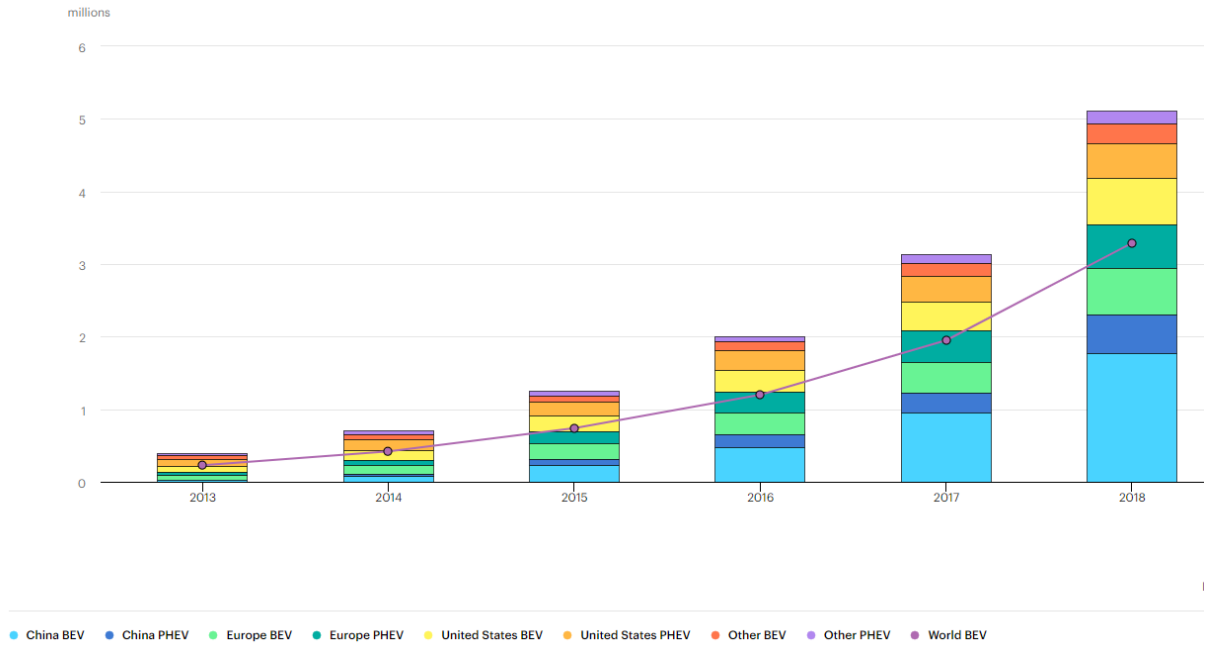

Fig. 1.2_Deployment of EVs in selected countries, 2013-2018 [14]

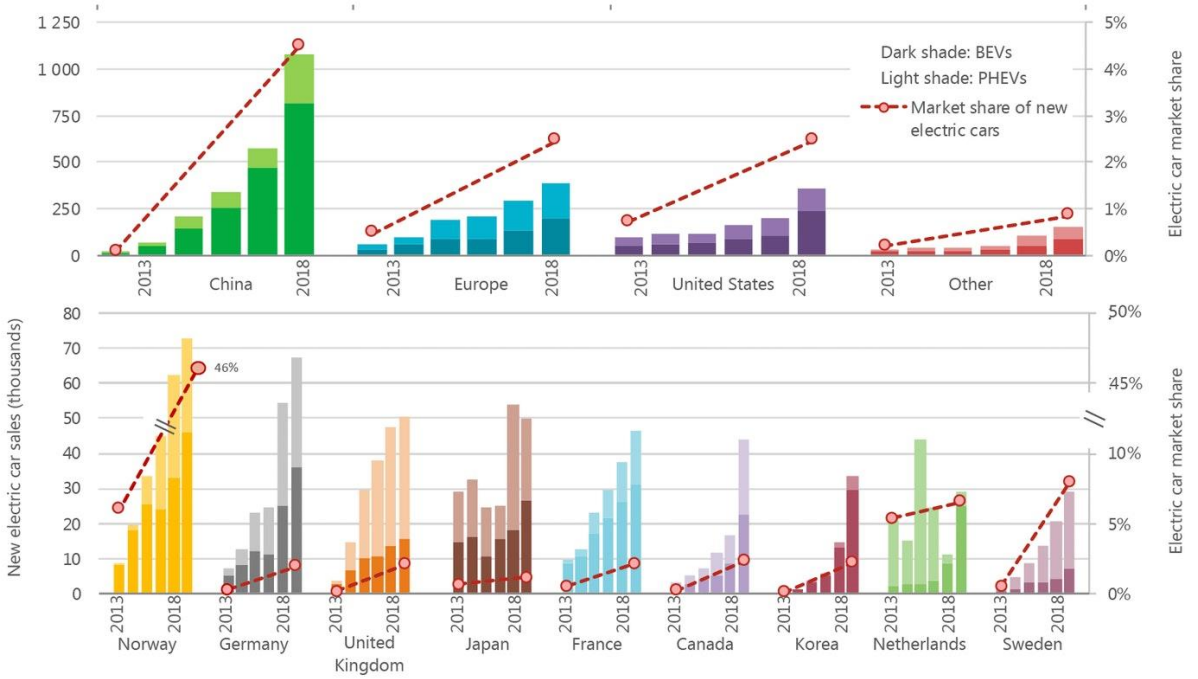

Fig.1.3 Global EV sales and market share, 2013-2018 [14]

1.1.1 EV chargers

There are mainly three families of EV charging systems, which are, off-board, on-board and contactless battery charger [15].

a. **Off-board EV battery charger** : The off-board charging systems are capable of transferring higher amount of power to EVs with DC current and it requires a more sophisticated Battery Management System (BMS). Also AC/DC conversion hardware can be put in the external hardware, which will reduce the weight and volume of EVs [16]. This in turn increases the overall efficiency of the EVs. However, off-board EV battery chargers introduce an additional cost for developing the infrastructure of the charging stations. Examples of some of these chargers are CHAdeMO – worldwide, CCS-Combo2 – Europe, SAE-CCS-Combo1 -North America and GB/T – China [17].

b. **On-board EV battery charger:** In case of on-board charger both AC/DC and DC/DC converters are present within EVs. This in turn increases the weight and volume of the cars [18]. However, on-board charger provides more flexibility. EVs are able to charge in residential as well as many other locations where an AC power source is available. On-board chargers are categorised into 2-levels :
    i) Single phase where the power rating is around 7.4 kW with JSAE1772 socket, popular in North America and Japan.
    ii) 3-phase where the power rating is upto 44kW with Mennekes or VDE-AR-E socket, popular in Germany [19].
    iii) Single phase of power level up to 7.4kW and 3-phase of power level upto 22kW with CCS-Combo socket are popular options in France [20].

c. **Wireless EV battery charger:** Wireless power transfer, also known as inductive charging, is an emerging technology that allows EV to recharge without cable connection as shown in Fig.1.4. This technology also allows the possibility to charge the vehicle during movement, however, it requires high infrastructure cost. This charging system uses two induction coils: transmitting and receiving. Transmitting coil at the charging base station generates alternating electromagnetic field while the receiving coil in PHEV receives power from electromagnetic field for generating electrical current to charge the battery [21]. But it is not widely used as conductive type chargers due to lower efficiency and high cost.

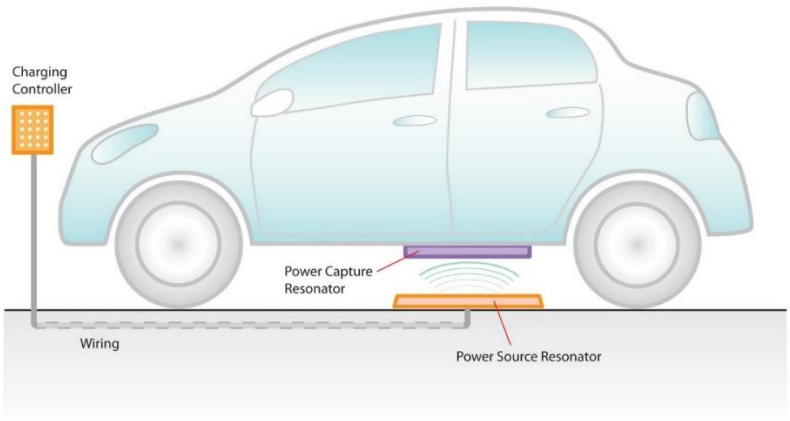

Fig.1.4 Wireless EV charging

1.1.2 Battery charger: Grid-to-Vehicle (G2V) and Vehicle-to-Grid (V2G) technology

The main purpose of EV battery charger is to transfer power to the battery (G2V) but there is a possibility to use the bidirectional battery charger and provide some network ancillary services, discussed in Sec. 1.3. Only for G2V operation, converters with unidirectional power transfer capability are used. However, bidirectional battery charger can support both G2V as well as reverse power flow from EV battery to the power grid, i.e., V2G technology. This concept is well presented in Fig.1.5 [22] [23].

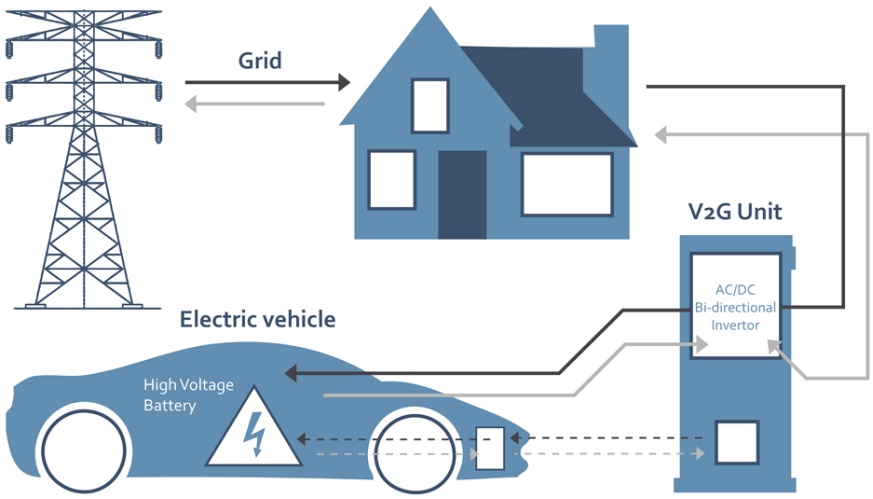

Fig.1.5 Concept of bidirectional power flow between EV and grid

Typical topology of the bidirectional EV battery charger has been shown in Fig.1.6. Bidirectional EV battery charger consists of two stages. First stage consists of an AC/DC converter, which facilitates the bidirectional power flow from the grid to the internal DC link. In addition, it can maintain unity power factor, if required. The second stage consists of DC/DC converter, which regulates the battery current and voltage [24] [25] [26].

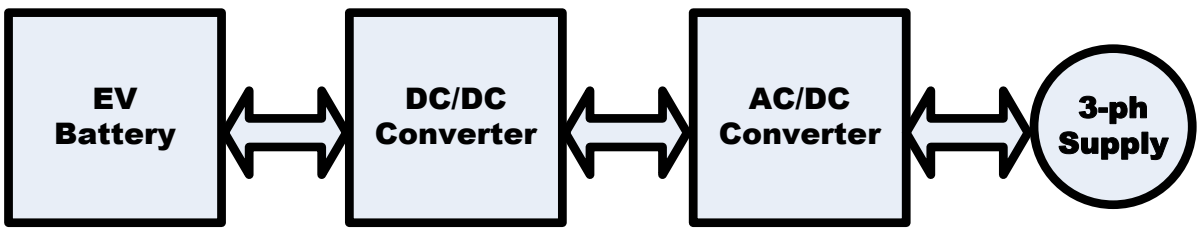

Fig.1.6 Topology of bidirectional EV battery charger

Depending on power level, generally single-phase half/full bridge, three phase full bridge or multilevel converter topologies are used for grid connected AC/DC converter [27]. Based on DC/DC converter, charger can be classified as isolated or non-isolated. In case of isolated charger, a high frequency (HF) isolation transformer has been incorporated into the DC/DC

converter. Examples of non-isolated bidirectional DC-DC converters that are commonly used include half-bridge, Ćuk, SEPIC and cascade buck-boost converters [28]. Isolated bidirectional DC/DC converters can either be half bridge, full bridge topologies, Dual Active Bridge (DAB) converter [29] and full bridge resonant type converters.

1.2 Literature review on bidirectional topologies of EV battery charger

Battery chargers, with unidirectional converter topology, allow only the primary requirement which is G2V operation. For both G2V and V2G applications, bidirectional converter topology must be used in EV battery charger. This section illustrates different possible topologies of EV battery chargers for bidirectional power flow. Bidirectional EV battery chargers are generally based on two independent power structures connected together. This section contains different configurations of two-stage EV battery charger. Fig.1.7, Fig.1.8 and Fig.1.9 represent different configurations of the first stage (AC/DC) of the whole bidirectional converter topology while Fig.1.10, Fig.1.11 and Fig.1.12 represent different configurations of the second stage (DC/DC) of the bidirectional EV battery charger.

1.2.1 AC/DC conversion stage

Single-phase and three-phase AC/DC converter topologies can have different configurations: half bridge and full bridge. They can also be categorized into two-level and multi-level converters. Single/three-phase half/full bridge two-level AC/DC converters, as seen as in Fig.1.7 and Fig.1.8, are the mostly used AC/DC converter topologies. Though half-bridge configuration is less complex and has less number of semiconductor switches compared to full-bridge configuration but the voltage stress is higher in the semiconductor switches present in half-bridge configuration for same power rating. In case of half-bridge configuration, capacitive middle point voltage fluctuation is another problem and that can leads to a significant size of the capacitors. The capacitors are also problematic in terms of reliability, especially in case of high temperatures. Both the converters are generating high frequency current harmonics, so additional passive element like AC-current inductor is necessary for filtering [30].

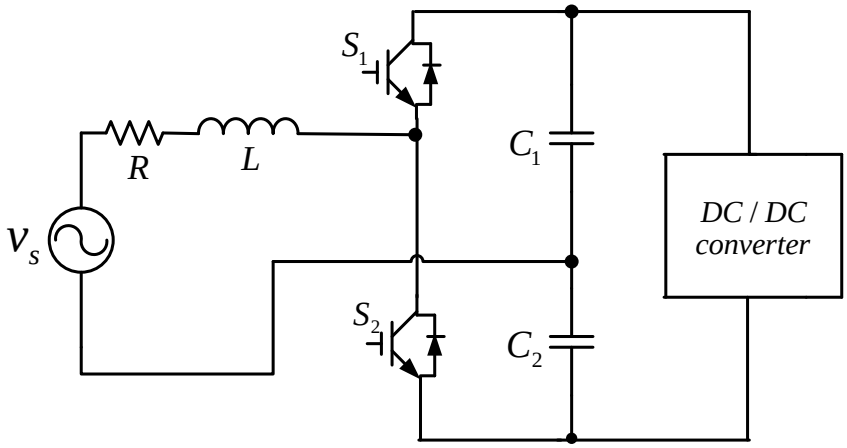

Fig.1.7 Single-phase half-bridge bidirectional AC/DC converter

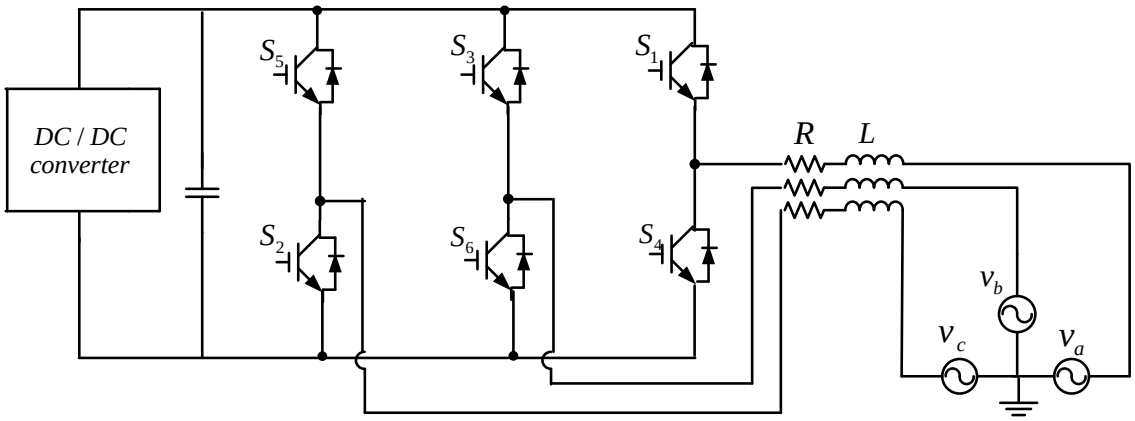

Fig.1.8 Three-phase full-bridge bidirectional AC/DC converter

Three phase Neutral Point Clamp (NPC) inverter, as seen in Fig.1.9, is a multilevel bidirectional AC/DC converter that can be used for high power rating. Multilevel topologies, such as NPC, Cascaded H-Bridge converter (CHB) or Flying Capacitor Converter (FCC) [31] [32], have some advantages over two-level converter such as : lower semiconductor voltage stress, higher switching frequency because of lower switching losses and smaller filter due to better harmonic performance [33].

But it has structural drawback due to present of capacitive middle point in the DC-bus. Bigger size capacitors or additional control circuit is required in order to maintain the voltage difference within the allowed limit at the middle point of the DC-bus.

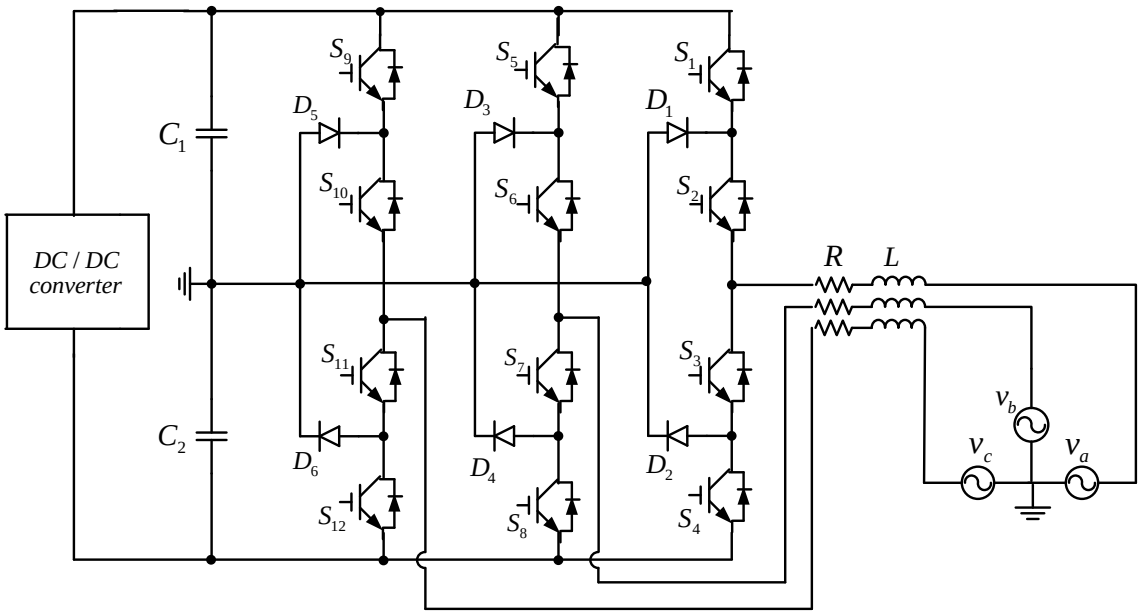

Fig.1.9 Three-phase three-level bidirectional AC/DC converter

1.2.2 DC/DC conversion stage

Bidirectional DC/DC converter can be two types: isolated and non-isolated [34]. Two-quadrant bidirectional DC/DC converter, shown in Fig.1.10, is very simple to control. Direction of power exchange, i.e., G2V or V2G mode of operation depends on the duty cycle of the controlled switches ($S_1 and\ S_2$) and the$\frac{V_{DC}}{V_{BAT}}$.

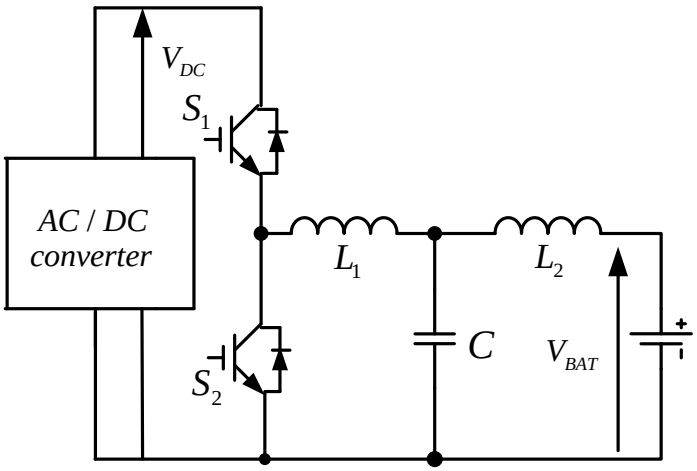

Fig.1.10 Two-quadrant bidirectional DC/DC converter

Fig.1.11 shows an interleaved bidirectional DC/DC converter where two parallel buck-boost converters are operating at 180° out of phase. With this configuration, higher power level can be achieved. Battery current ripple will also be reduced due to the operation of the converter and the phase shift between the signals [35].

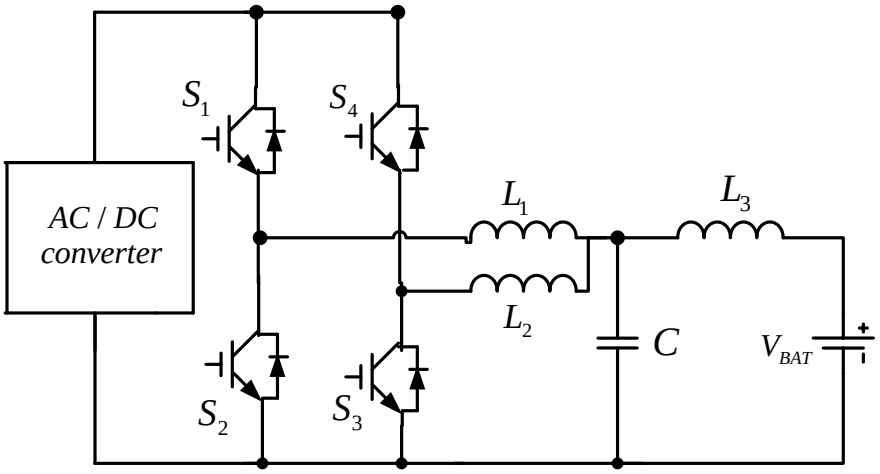

Fig.1.11 Interleaved bidirectional DC/DC converter

In order to simplify the safety requirements, the insulation of the battery and the network can be useful. Therefore, these configurations are not the preferred ones. Fig.1.12 represents an insulated bidirectional DC/DC converter, the Dual Active Bridge (DAB). In this configuration, two active bridges are linked with the help of a High Frequency (HF) transformer. This HF transformer is used for isolation purpose [36]. Power flow in DAB can be possible by Phase Shift Modulation (PSM) method between the two bridges. In primary bridge of DAB, identical gate signals with 50% duty cycle are applied to S_1 andS_2. Similar gate signals with 50% duty cycle are applied to S_3 andS_4. The gate signals of S_1 and S_3 are complementary. In PSM method, power flow between two bridges of DAB can be possible by shifting the gate pulses of S_5 and S_6 with respect to S_1 and S_2 and gate pulses of S_7 and S_8 with respect to S_3 and S_4 [37]. Direction of the power flow depends on the angle of shifting(δ). Power will flow from primary to secondary active bridge with + δ and in reverse direction with – δ.

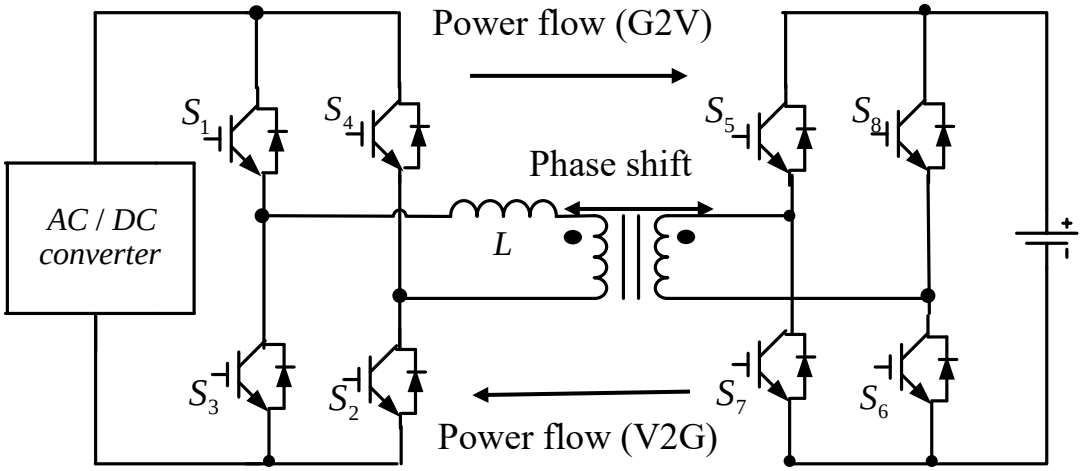

Fig.1.12 Dual Active Bridge

Efficiency of the DAB can also be increased by using Dual Active Bridge Series Resonant Converter (DABSRC) topology. In this topology, a capacitor is connected in series with inductor in primary bridge of the DAB [38].

1.3 Ancillary services of V2G technology

"Ancillary services" refers to a variety of operations provided by the electricity grid that are required to support the continuous flow of electricity as shown in Fig.1.13. This ensures stability and security in the electricity grid. The energy storage will play a pivotal role in delivering important grid services in future. In practice, most of the cars traveling on the road only for 4-5% of the day and spend the rest of time at parking. We can utilize such EVs to facilitate the ancillary services in V2G system [39]. Possible ancillary services provided by V2G technology have been listed below.

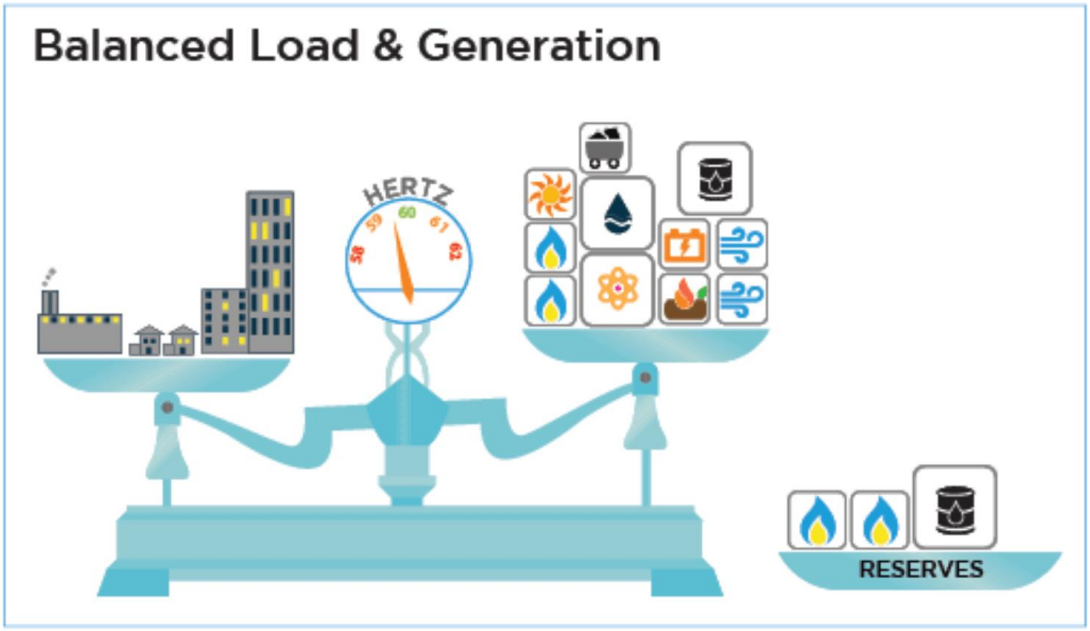

Fig.1.13 Continuous supply of electricity to the load [40]

a. **Peak power shaving:** Peak-shaving and valley-filling are two important services that V2G can provide. During peak load period, different types of power plant need to be turned on quickly in order to provide the extra power. Normally, these power plants are more expensive to operate. During off-load period, EVs can charge their battery.

b. **Regulation:** V2G system can regulate the voltage and frequency of the power grid. At each point in time, the generation of electricity produced by grid must exactly match the amount of energy taken from the grid by consumers (households, factories, buildings, EVs, etc.). Else, the nominal frequency of the grid (50 Hz in Europe or 60 Hz in the U.S.) will exceed the threshold and can turn into a blackout. In this sudden increment of frequency due to more generation of power, EVs can help by charging their batteries. On the other hand, if the frequency is too low, it can be regulated either

by disconnecting EVs from grid or by discharging a number of EVs connected to the grid.

A large group of EVs can also help the power grid to regulate voltage by adjusting (injecting or consuming) reactive power across the power grid. EV battery chargers with their power electronic structure can help by changing their reactive and active power load, without any major impact on their battery life. This makes reactive power compensation a very promising ancillary service in the future V2G systems [41].

c. **Supporting renewable energy integration:** Due to the stochastic and intermittent nature of solar and wind-power generation, their large scale integration into the current power grid requires large-capacity storage systems [42]. EVs can be used as a storage unit during higher generation of renewable energy and both of them together can increase the stability and the reliability of the grid.

d. **Revenue generation for EV users:** Depending on the regulations of each country, EV users can generate revenue by discharging EV batteries during peak-load period at higher electricity price and recharge the battery during off-load period at reduced electricity price.

1.4 Motivation and main contribution of the thesis

EVs, as alternatives to traditional thermal engine vehicles, are gaining popularity over the last decades due to zero emission during their use. For G2V technology, research on smart and safe charging, multiplexing of EVSE have been studied extensively. Questions regarding how EV charging can be better managed to either lower the charging cost or creating less impact to the power grid can be understood with these studies.

On the other hand, by enabling bidirectional power flow with V2G technology, EVs are not only considered as load to the grid, but also act as distributed storage and generation systems. Considering all the benefits of EVs and the ancillary services provided by V2G technology, the integration of EVs to power grid has brought new technical and economic challenges as well as opportunities. Since EVs can be used as active and reactive power generating unit, we want to go further in the capabilities allowed by them. By allowing active and reactive power exchange, V2G technology ensures the previously mentioned ancillary services as presented in the PhD thesis of Mounir Marzouk where a 3-phase 22kW bidirectional battery charger for hybrid trucks was developed [43]. However, these exchanges are in balanced condition, which means the power exchange is almost same between all three phases.

In this thesis, we want to investigate the possibility to use the charger in unbalanced power exchange conditions. Thus, the main motivation for this research work is to **compensate and**

mitigate the unbalance active (P) and reactive (Q) power exchange between supply of three phases.

However, in low voltage networks, lots of loads are single phase ones which introduces very common issues in these networks. This creates unbalance in power consumption($P_1 \neq P_2 \neq P_3$), which in turn creates unbalance in current in the network as shown in Fig.1.14 and possibly unbalances in voltage due to the line/transformer impedances [44] [45]. Red arrow represents an example of unbalanced power consumption due to single-phase loads.

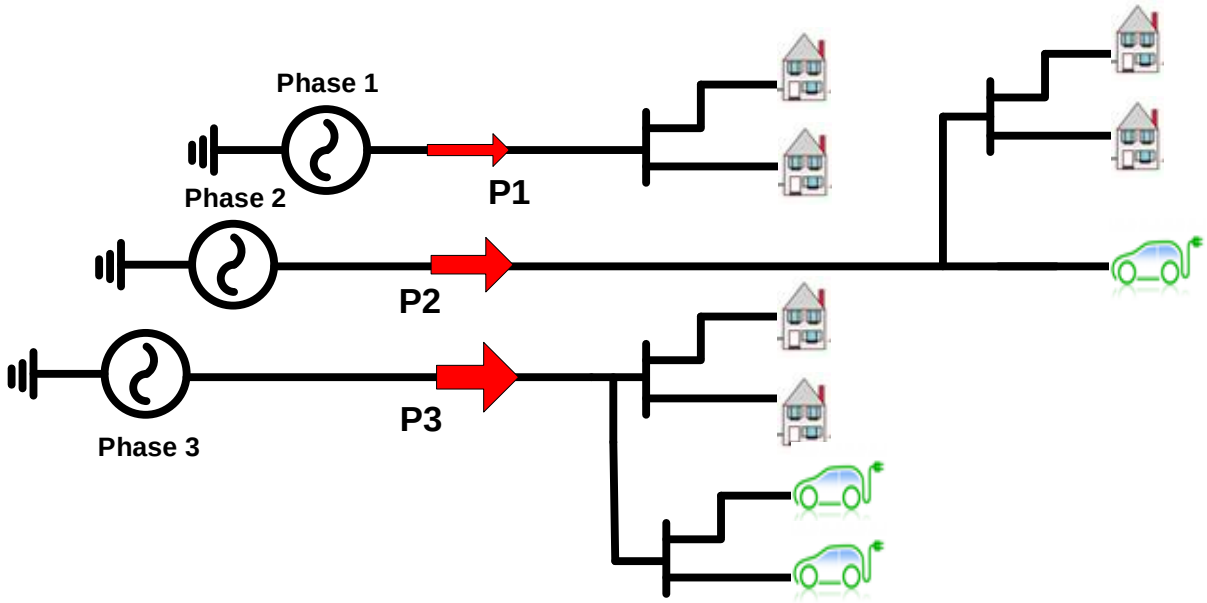

Fig.1.14 Unbalance in the network due to unequal power consumption by single phase load

This current unbalance has negative impacts on the grid, such as,

- Increase in neutral current and that can create an overheating and insulation failure of the line conductor.
- Can generate voltage unbalances between the phases and reduces the efficiencies of transformers, transmission line and machines on the load side [46] [47].

In order to mitigate the current unbalance, required active or reactive power should be injected to the grid from outside storage unit, which can be EV battery with bidirectional converter. It can redistribute currents by injecting or absorbing right amount of active and reactive power from each phase as shown in Fig.1.15. This figure indicates that the converter absorbs the active power and injects reactive power to each phase independently.

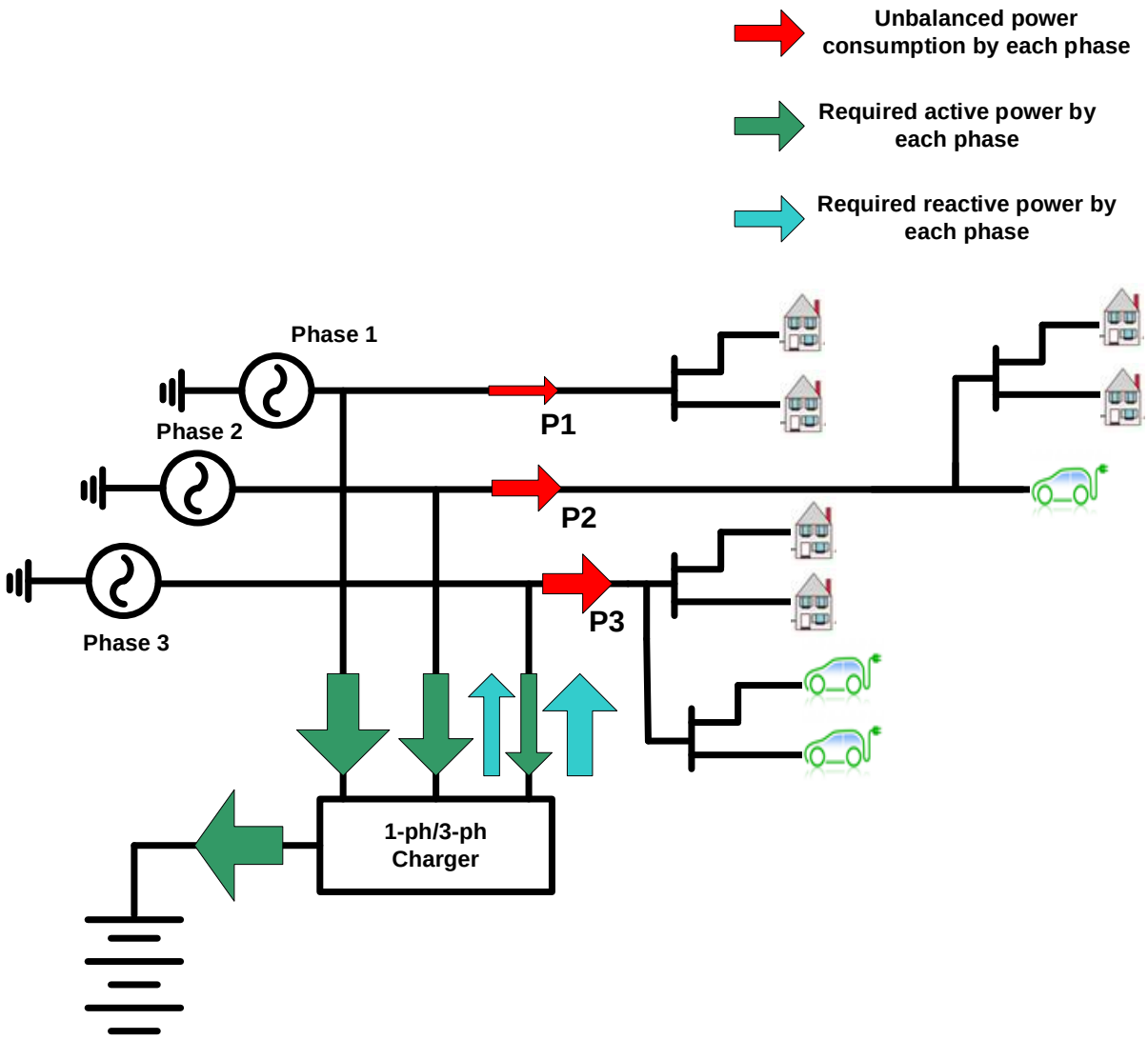

Fig.1.15 Mitigation of current unbalance by consuming & injecting active & reactive powers to the network

This compensation and mitigation of currents unbalance provides the following grid-supporting services, which is one of the main motivations of V2G applications:

- Shifting of neutral point and its associated problems can be solved [48].
- Since the currents are balanced, their average will be lower and it will reduce the grid loss, heating problem and grid voltage fluctuation [49].

Based on the motivations of research work, the contributions of this thesis can be summarized as follows:

i) Comparison between different configuration of AC/DC bidirectional converters in terms of size of the passive elements, harmonic contents and THD.

ii) Selection of AC/DC bidirectional converter that can support unbalance current injection situation.

iii) Selection of the insulated bidirectional DC/DC converter configuration.

iv) Modelling and control of the selected dual stage bidirectional EV charger.

1.5 Outline of the thesis

Chapter 1 introduced the general discussions on EVs, concept of G2V and V2G applications, ancillary services of EVs and different topologies of both unidirectional and bidirectional EV battery chargers. Comparison of different configurations, their constraints and corresponding modelling of the bidirectional AC/DC converters for EV battery charger will be discussed in Chapter 2. Control strategy, design of the controllers and validation of the corresponding results in Matlab/Simulink of the bidirectional AC/DC converter in unbalance current injection scenario for EV battery charger will be presented in Chapter 3. In Chapter 4, the comparison of different configurations of bidirectional insulated DC/DC converter, their control strategies and corresponding results in Matlab/Simulink will be presented. Chapter 5 presents the integration of the full bidirectional converter used in EV battery charger, test of the whole converter in different scenarios in HIL simulations. It also compares the proposed solution in terms of sizing of passive elements, THD of the network, r.m.s current and losses in the converter.

1.6 Conclusion

However, EVs and V2G are emerging technologies with lot of benefits but there are some issues that can act as barriers, such as,

1. Driving range: The current EVs can travel around 70-200 miles with a single charge and that is less compared to fossil-fuelled car [46]. However, HEVs can reduce range anxiety a lot as the electric motor works in tandem with ICE.

2. Recharge time: Compare to fossil-fuelled car, EV takes a lot of time for recharging. A typical EV (60kWh battery) takes just under 8 hours to charge from empty-to-full with a 7kW charging point. Even a rapid charge takes around 20-30 minutes while refilling of petrol/diesel will take maximum 5 minutes [50].

3. Battery life: Additional battery cycles due to V2G operation can shorter the life span of the battery [51].

4. Cost: EVs are generally costlier than fossil-fuelled car. However, with V2G technology car owner can earn by selling electricity during peak-load period which can help to mitigate the higher price of the V2G chargers.

In this chapter the context of the thesis has been established. The EV, V2G technology and their prospective have been discussed. Existing configurations of the converters and their working principle have been explained. The scope and contributions of this thesis are also described. In the following chapter, comparison between different configurations of AC/DC bidirectional converters will be presented. Based on comparison, thanks to analytical models in Mathcad and their validation in Simulink, suitable configuration will be chosen for bidirectional EV battery charger.

Chapter 2

AC/DC CONVERTER

This chapter introduces the comparison and selection of AC/DC bidirectional converter that is suitable for onboard EV charger with V2G application in case of unbalance current injection situation.

2. Introduction

Conversion between AC to DC or vice versa is an important issue in a microgrid system. Normally, battery of EVs and renewable energy sources produce DC power while the conventional electricity grid uses AC power. In order to have V2G operation, bidirectional Voltage Source Converter (VSC) is required to generate the desired AC or DC output voltage or current according to the grid codes of EU. There are several configurations of the three-phase grid connected bidirectional VSC, discussed in Sec. 2.1.

2.1 Configurations of three-phase voltage source converters

Several configurations of 3-phase grid connected VSCs have been proposed in the literatures in recent years. In the following sections, description and comparison of the different configurations (2-level/multilevel and 3-legs/4-legs) of AC/DC bidirectional converters have been made.

In classical 3-phase topologies, only the three phases are connected to the converter. Nevertheless, one of the main objectives of this research activity is to compensate and mitigate the unbalance active and reactive power exchanges between 3-ph grid supply, i.e., to operate the bidirectional EV battery charger under current unbalance situation. In order to be able to inject unbalanced currents into the grid, it is necessary to have the neutral point connected to the converter structure [52]. There are some solutions to connect the grid neutral with the converter, such as,

i) Using three H-Bridges
ii) Splitting the converter DC-bus
iii) Converter with fourth leg [53]

Three H-bridges can be connected to the 3-phase 4-wire grid by using three isolation transformers as shown in Fig.2.1. However, this converter structure can fully control all the phase currents in the grid and the transformers can act as a filter but the drawbacks of the structure are the use of large number of semiconductor switches and several low frequency transformers, which are heavy, bulky and difficult to integrate in a vehicle.

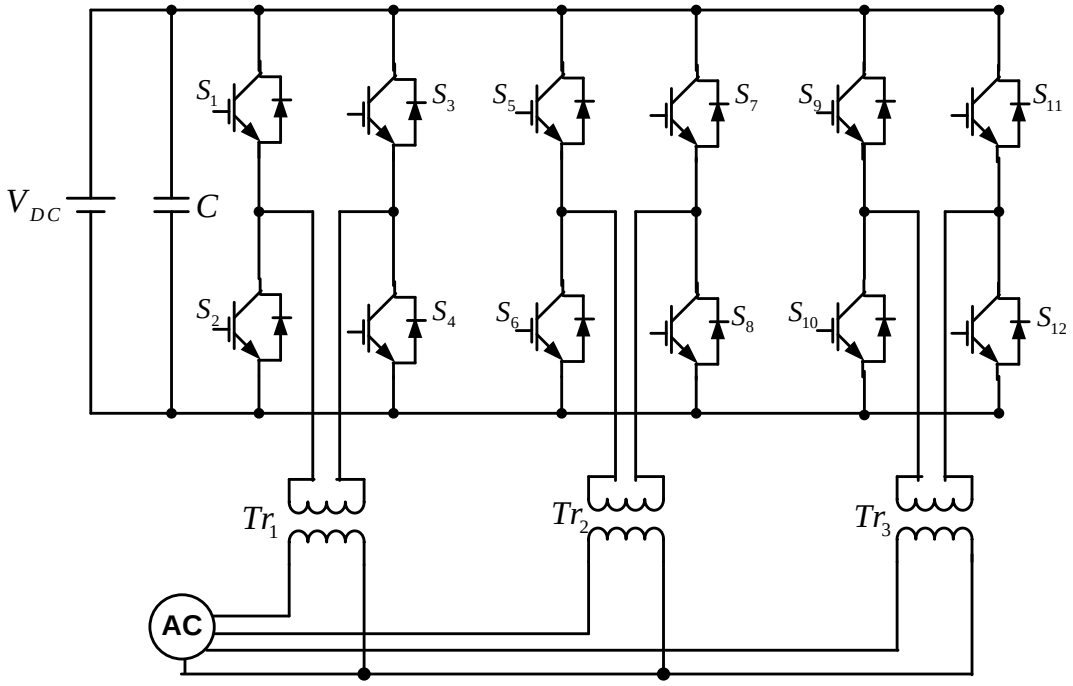

Fig.2.1 H-bridge converter configuration with a neutral connection

Splitting the DC-bus capacitors and connecting the neutral point at the middle point of the DC-bus is an easy and low cost solution. With this solution, 3-ph 4-wire converter topology is required. In case of the 2-level VSC, 3-ph 4-wire configuration can be possible by splitting the DC bus capacitor into two parts as shown in Fig.2.2. In case of NPC, this middle point of the DC bus already exists due to the converter structure and it is shown in Fig.2.3. 3-ph 4-wire converter topology also provides safety on flowing of leakage current between EVSE and the car.

Major challenges with 3-legs 4-wires 2-level or 3-level converter are to balance the voltage of the middle point of the DC-bus capacitors as well as to control the voltage oscillation happens in the whole DC-bus during unbalance current injection condition. Due to the injected currents, the difference between the two capacitor voltages can increase/decrease (depends on the direction of neutral current) and that will create an oscillation (due to deviation from the true midpoint of the DC source) at the middle point of the DC bus. This oscillation has to be limited in order to ensure correct current injections. This oscillation can be limited by increasing the size of the DC bus capacitors but that will increase the overall size and weight of the onboard charger.

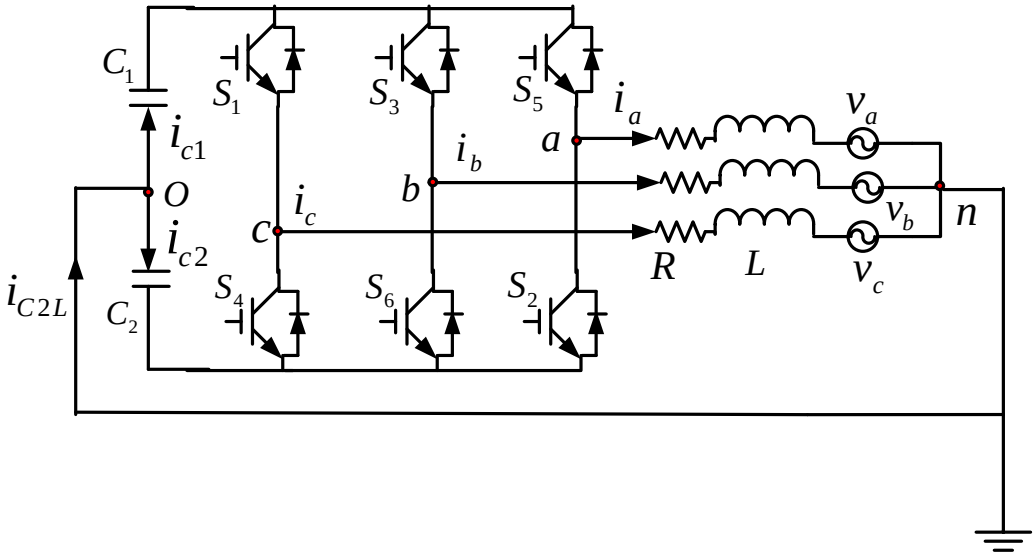

Fig.2.2 3-phase 3-legs 4-wires 2-level bidirectional VSC

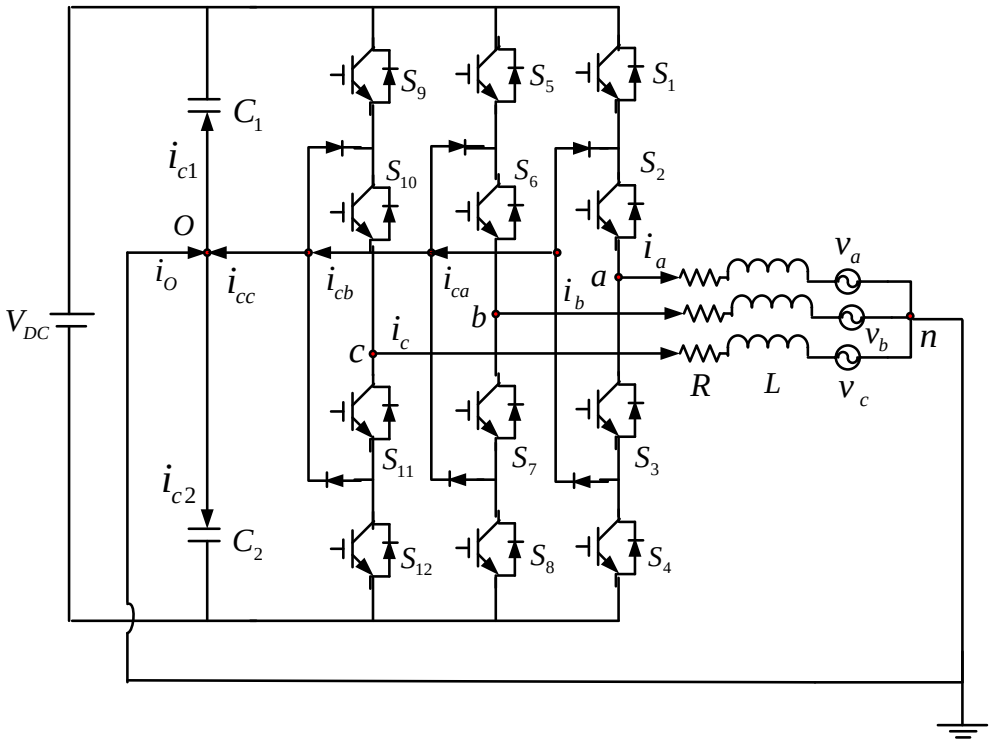

Fig.2.3 3-phase 3-legs 4-wires 3-level bidirectional VSC

The drawbacks of these two configurations can partially be solved (elaborated in Sec. 2.5) by adding a fully controllable fourth leg and connecting the neutral point to that leg as shown in Fig.2.4 [54]. The drawbacks with this configuration are:

- Decrease in reliability due to more semiconductor switches and associated gate drivers.
- Increase the complexity in control circuit of the converter.
- Additional inductance on the neutral.

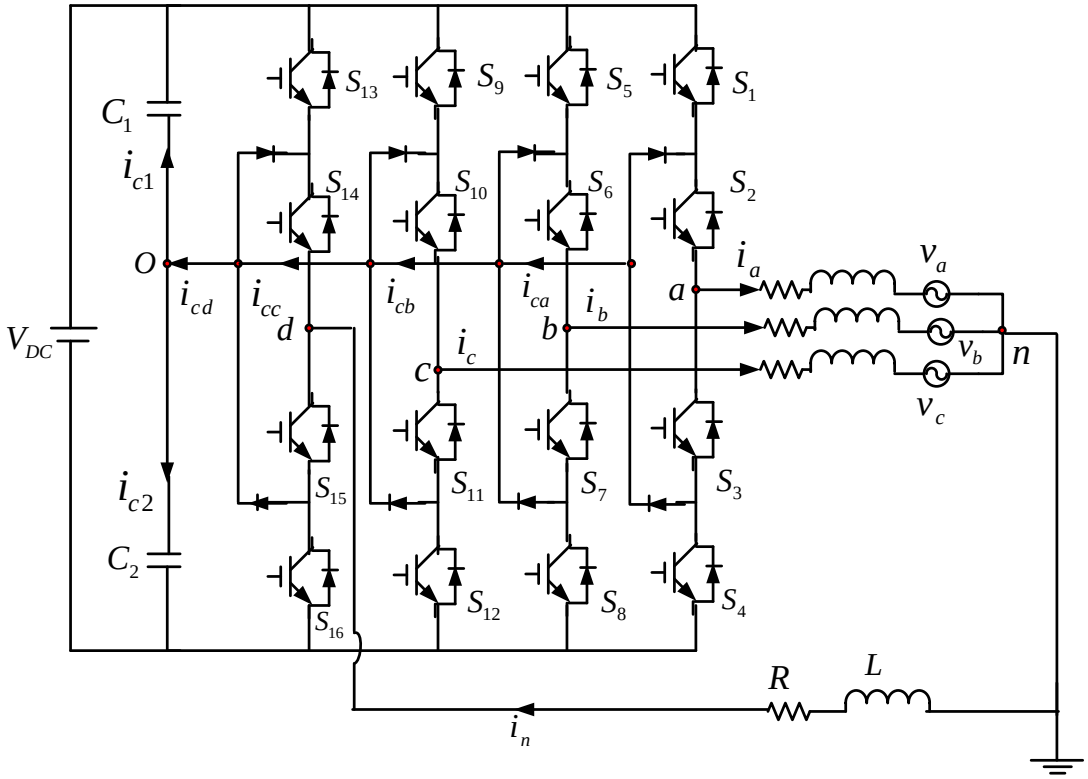

Fig.2.4 3-phase 4-legs 4-wires 3-level bidirectional VSC

Next section compares different configurations of the 3-ph 4-wire AC/DC converter and after that the most suitable configuration has been chosen for our application.

2.1.1 Comparison between 2-level and multilevel voltage source converters

A 2-level VSC is the preferred topology in low-voltage applications (<500V and <100kW) [55]. Generally, this type of converters have some benefits, such as:

- Low cost and simple structure
- High safety and robustness.

However, the weaknesses of the converters are mainly higher EMI disturbances due to higher harmonics. This needs bigger filters in order to respect the EMC standards and this in turn increases the volume and weight of the converter.

The multilevel converter plays an incredible role in handling high power and high voltage applications in flexible power systems [56] [57]. The fundamental purpose of considering multilevel inverter instead of more classical 2- level VSC is due to the higher value of DC-link voltages that are required for future applications (around 600 – 800V). In addition, it is beneficial to connect the switches having lower voltage ratings in series instead of using switches with higher voltage ratings. Because of lower on-resistances and faster switching of these series connected switches, the global losses reduce and therefore enhance the efficiency [58]. It is possible to use fast MOSFET semiconductors, based on wide band gap semiconductor

technology with a nominal voltage compatible with the 3-level operation instead of classical IGBTs, due to reduced voltage stress [59].

Furthermore, because of the stepwise output voltage, multilevel converters present many advantages in comparison with conventional 2-level converters. Volume and weight are the main constraints for onboard EV battery chargers. The size of the input filters on AC side has been reduced due to higher signal quality in the multilevel converters. This in turn reduces the volume and weight of the overall charger.

There are several multilevel converters structures, which have been introduced but the basic and well-known topologies are the Neutral Point-Clamped Multilevel Converter (NPC) [60], Flying Capacitor Multilevel Converter (FCC) [61] and Cascaded H-Bridge multilevel converter (CHB) [62] [63]. These three basic topologies have been widely accepted for industrial applications. Beside of all the advantages of multilevel converters over 2-level converter, the major drawback is that it requires more power semiconductor switches and associated gate driver circuits to achieve higher output levels [64]. This will affect the reliability of the battery charger.

In the following sections of this Chapter 2, comparison and selection between 3-phase 3-legs 4-wires 2-level and NPC inverter has been done in different conditions. In the 3-leg converter topology, the voltage oscillation at the middle point of the DC bus capacitors is important and has to be checked and limited.

2.2 Circuit configurations and their mathematical model

In this section, mathematical modelling of 2-level and NPC converters have been done. With the help of these models, the most suitable bidirectional AC/DC converter structure for the onboard EV battery charger has been selected.

2.2.1 Mathematical representation of 3-ph network

Considering, 3-phase balanced network of phase-to-phase voltage at 400V, phase to neutral voltages are represented as:

$$\boldsymbol{v_{sa}(t) = V_m sin\omega t} \quad \textbf{(1)}$$

$$\boldsymbol{v_{sb}(t) = V_m sin(\omega t - \frac{2\pi}{3})} \quad \textbf{(2)}$$

$$\boldsymbol{v_{sc}(t) = V_m sin(\omega t + \frac{2\pi}{3})} \quad \textbf{(3)}$$

Operating in balanced network conditions, three active powers($P_a, P_b\ and\ P_c$), reactive powers ($Q_a, Q_b\ and\ Q_c$) and corresponding apparent powers ($S_a, S_b\ and\ S_c$) components are considered. Root-Mean-Square (RMS) currents in each phase are expressed in Equ. 4-6.

$$I_{aeff} = \frac{S_a}{V_{eff}} \quad (4)$$

$$I_{beff} = \frac{S_b}{V_{eff}} \quad (5)$$

$$I_{ceff} = \frac{S_c}{V_{eff}} \quad (6)$$

Three line and neutral currents can be written as:

$$i_{sa}(t) = \sqrt{2} I_{aeff} sin(\omega t - \varphi_a) \quad (7)$$

$$i_{sb}(t) = \sqrt{2} I_{beff} sin(\omega t - \frac{2\pi}{3} - \varphi_b) \quad (8)$$

$$i_{sc}(t) = \sqrt{2} I_{ceff} sin(\omega t + \frac{2\pi}{3} - \varphi_c) \quad (9)$$

$$i_{sn}(t) = -[i_{sa}(t) + i_{sb}(t) + i_{sc}(t)] \quad (10)$$

2.2.2 Determination of the middle point current and voltage variations for 2-level VSC

In 2-level VSC, as shown in Fig.2.2, capacitor current (i_{C2L}), which is equal to the neutral current (i_{sn}), will flow through the middle point (O) of the DC-bus capacitors. Half of i_{C2L} will flow through the upper capacitor (C_1) while the remaining half will flow through lower capacitor(C_2), considering $C_1 = C_2 = C$ (4.7 mF in the experimental test bench). Magnitudes of the voltage oscillations ($\frac{dV_{c1}}{dt}$ and $\frac{dV_{c2}}{dt}$) across the DC-bus capacitors are expressed as,

$$\frac{dV_{c1}}{dt} = \frac{i_{C2L}}{2C} \quad (7)$$

$$\frac{dV_{c2}}{dt} = -\frac{i_{C2L}}{2C} \quad (8)$$

In case of balanced energy exchange between three phases, as$i_{C2L} = i_{sn} = 0$,

$$\frac{dV_{c1}}{dt} = \frac{dV_{c2}}{dt} = 0 \quad (13)$$

In case of unbalance network, these oscillations will not be equal to zero as$i_{sn} = i_n \neq 0$. The current flowing through each capacitor will be expressed as,

$$i_{C1} = i_{C2} = \frac{i_{C2L}}{2} = \frac{-\sqrt{2} I_{aeff} sin(\omega t - \varphi_a) - \sqrt{2} I_{beff} sin\left(\omega t - \frac{2\pi}{3} - \varphi_b\right) - \sqrt{2} I_{ceff} sin(\omega t + \frac{2\pi}{3} - \varphi_c)}{2} \quad (14)$$

Voltage variation at the capacitive middle point will be calculated as,

$$\Delta v_{2L}(i) = \frac{1}{2C} \int_0^t i_{c2L}(t) dt \quad (15)$$

[Considering$C_1 = C_2 = C$]

Thanks to the numeric integral algorithm in Mathcad, this Equ. 15 was solved.

2.2.3 Determination of the middle point current and voltage variations for 3-level VSC

In case of 3-phase 3-legs 4-wires NPC, as shown in Fig.2.3, the capacitor current at the middle point of the DC-bus is not only composed of the neutral current but also of a current generated by each phase (i_{ca}, i_{cb} and i_{cc}). Mathematical modelling of 3 phase 3- legs NPC has been described below.

The modulation index can be presented as,

$$\boldsymbol{m_x(t) = 0.5 + \frac{v_{conx}(t)}{E}} \quad \textbf{(16)}$$

Where $x \in a, b, c$ and E= DC bus voltage [32].

As instantaneous voltages and currents are known, the converter side voltages can also be calculated as,

$$\boldsymbol{v_{cona}(t) = v_{sa}(t) + L\frac{di_{sa}(t)}{dt}}$$

$$\boldsymbol{= V_m sin\omega t + \sqrt{2} I_{aeff} L\omega \cos(\omega t - \varphi_a)} \quad \textbf{(17)}$$

$$\boldsymbol{v_{conb}(t) = v_{sb}(t) + L\frac{di_{sb}(t)}{dt}}$$

$$\boldsymbol{= V_m \sin(\omega t - \frac{2\pi}{3}) + \sqrt{2} I_{beff} L\omega \cos(\omega t - \frac{2\pi}{3} - \varphi_b)} \quad \textbf{(18)}$$

$$\boldsymbol{v_{conc}(t) = v_{sc}(t) + L\frac{di_{sc}(t)}{dt}}$$

$$\boldsymbol{= V_m \sin(\omega t + \frac{2\pi}{3}) + \sqrt{2} I_{ceff} L\omega \cos(\omega t + \frac{2\pi}{3} - \varphi_c)} \quad \textbf{(19)}$$

Putting these values in Equ. 16, modulation indices can be expressed as,

$$\boldsymbol{m_a(t) = 0.5 + \frac{V_m sin\omega t + \sqrt{2} I_{aeff} L\omega \cos(\omega t - \varphi_a)}{E}} \quad \textbf{(20)}$$

$$\boldsymbol{m_b(t) = 0.5 + \frac{V_m sin(\omega t - \frac{2\pi}{3}) + \sqrt{2} I_{beff} L\omega \cos(\omega t - \frac{2\pi}{3} - \varphi_b)}{E}} \quad \textbf{(21)}$$

$$\boldsymbol{m_c(t) = 0.5 + \frac{V_m sin(\omega t + \frac{2\pi}{3}) + \sqrt{2} I_{ceff} L\omega \cos(\omega t + \frac{2\pi}{3} - \varphi_c)}{E}} \quad \textbf{(22)}$$

Contribution of each phase current to the capacitor middle point current can be expressed as,

$$\boldsymbol{i_{ca}(t) = \sqrt{2} I_{aeff} \sin(\omega t - \varphi_a) * (1 - 2|m_a(t) - 0.5|)}$$

$$\boldsymbol{= \sqrt{2} I_{aeff} \sin(\omega t - \varphi_a) * (1 - \frac{2 * |V_m \sin \omega t + \sqrt{2} I_{aeff} L\omega \cos(\omega t - \varphi_a)|}{|E|})} \quad \textbf{(23)}$$

$$\boldsymbol{i_{cb}(t) = \sqrt{2} I_{beff} \sin\left(\omega t - \frac{2\pi}{3} - \varphi_b\right) * (1 - 2|m_b(t) - 0.5|)}$$

$$\boldsymbol{= \sqrt{2} I_{beff} \sin\left(\omega t - \frac{2\pi}{3} - \varphi_b\right) * (1 - \frac{2 * |V_m \sin(\omega t - \frac{2\pi}{3}) + \sqrt{2} I_{beff} L\omega \cos(\omega t - \frac{2\pi}{3} - \varphi_b)|}{|E|})} \quad \textbf{(24)}$$

$$\boldsymbol{i_{cc}(t) = \sqrt{2} I_{ceff} \sin\left(\omega t + \frac{2\pi}{3} - \varphi_c\right) * (1 - 2|m_c(t) - 0.5|)}$$

$$\boldsymbol{= \sqrt{2} I_{ceff} \sin\left(\omega t + \frac{2\pi}{3} - \varphi_c\right) * (1 - \frac{2 * |V_m \sin(\omega t + \frac{2\pi}{3}) + \sqrt{2} I_{ceff} L\omega \cos(\omega t + \frac{2\pi}{3} - \varphi_c)|}{|E|})} \quad \textbf{(25)}$$

From Equ. 23-25, it can be concluded that for each phase, the capacitor current depends on the line currents and the modulation index. The total current at the middle point of the DC bus is the sum of all three currents with the neutral current. The global current (i_{c3L}) at the middle point of the DC-bus in NPC inverter can be expressed as,

$$\boldsymbol{i_{C3L}(t) = i_{sc}(t) + i_{ca}(t) + i_{cb}(t) + i_{cc}(t)}$$

$$\boldsymbol{= -i_{sa}(t) - i_{sb}(t) - i_{sc}(t) + i_{ca}(t) + i_{cb}(t) + i_{cc}(t)} \quad \textbf{(96)}$$

From this current, the voltage of the capacitive middle point of the DC bus can also be calculated by using following formula,

$$\Delta v_{3L}(i) = \frac{1}{2C}\int_0^t i_{c3L}(t)dt \quad \textbf{(27)}$$

[Considering$C_1 = C_2 = C$]

Similar to 2-level converter, Equ. 27 was also solved by the numeric integral algorithm in Mathcad.

2.3 Comparison of 3-phase 3-legs 4-wires converters in different network conditions

In this section, we compare the voltage oscillations at the middle point of the DC-bus for both 2-level and 3-level VSC in different network conditions, thanks to Mathcad, Matlab/Simulink and experimental results. Different situations will be studied as the converter can operate in different modes, such as, single phase, three phase balanced and three phase unbalanced. After analyzing these results, it can be possible to conclude whether 2-level or 3-level VSC is better in terms of DC-bus middle point voltage oscillations. Based on this comparison, selection of suitable bidirectional AC/DC converter topology has been done that can be used in EV onboard battery charger.

2.3.1 Network with balance power exchange between phases

As reported in Equ. 15 and Equ. 27, zero current will flow at the middle point of the D.C bus in 2-level VSC during balance power exchange between phases. Whereas, due to the structure of NPC, 150Hz (3 times of the fundamental current frequency) current component is present at the middle point of the D.C bus capacitors during balance power exchange between phases. In order to verify the analytical formulation, an experimental test bench has been performed with the available test bench in the laboratory, as shown in Fig.2.5.

This test bench is equipped with four 3-level NPC legs and six 2-level legs sharing the same DC-link and controlled by an embedded controller based on both real-time processor and FPGA. For generating the gate pulses, the Xilinx FPGA processor, programmed by LabVIEW software, has been used.

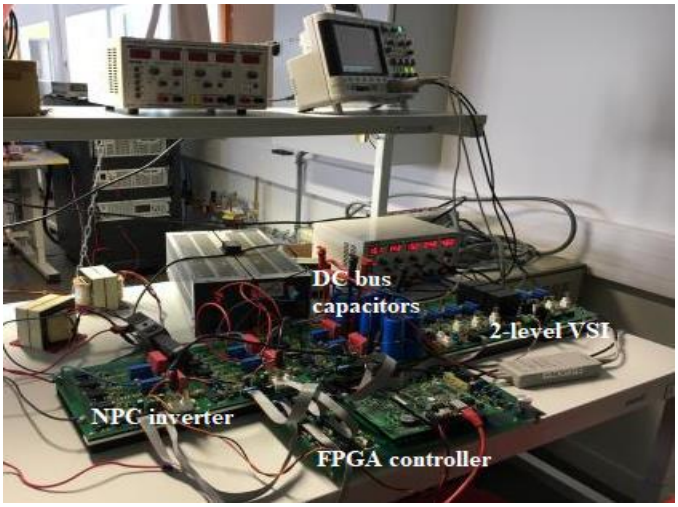

Fig.2.5 Experimental setup of 3-phase 4-wires 2-level and 3-level VSC

In this first experimental test, 2-level VSC is used as VSI which is supplied by a constant DC-supply voltage ($V_{dc} = 200V$) and connected to 3-phase star-fashioned RL-load where$R = 100\Omega$ *and* $L = 5mH$ (*due to the availabilty in the laboratory*). Fig.2.6 represents the schematic version of the experimental set-up. Same model with same operating conditions has been developed in Matlab/Simulink environment for validating the experimental tests.

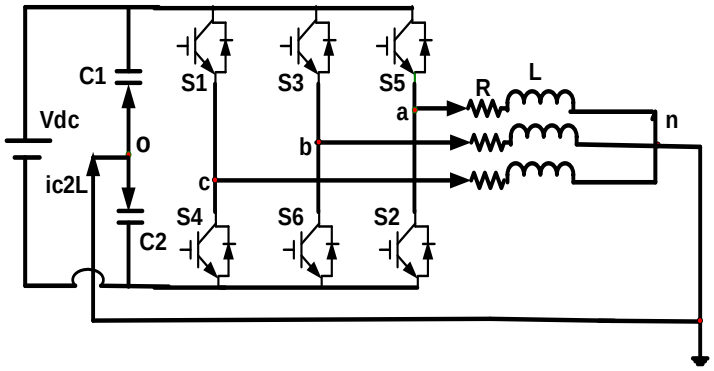

Fig.2.6 Schematic representation of the experimental tests on 3-phase 4-wires 2-level VSI during balanced power exchange condition between three output phases

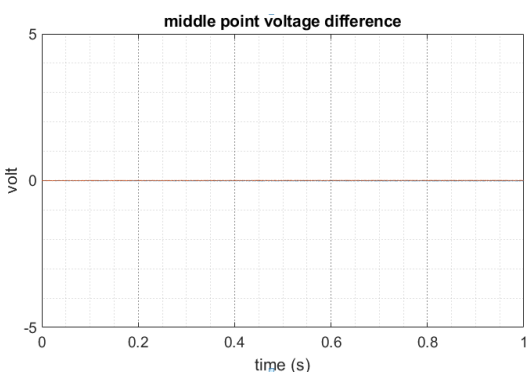

(a)

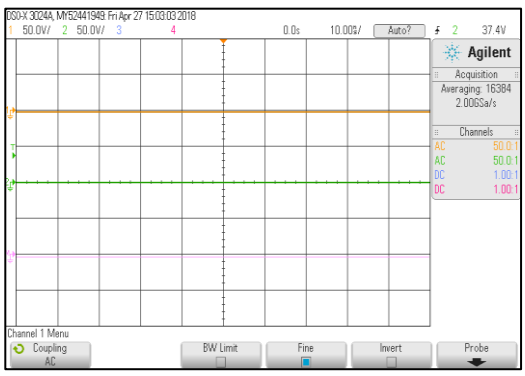

(b)

Fig.2.7 DC-bus upper and lower capacitor voltages during the experimental tests on 3-phase 4-wires 2-level VSI during balanced power exchange condition between output three phases: a. time-domain simulation result b. experimental result

During the experimental test, oscilloscope channels are set in AC-coupling mode for measuring the ripples only. From Fig.2.7, it is observed that upper, lower capacitor voltages and their difference are set at zero in both simulation and experimental test. This is in accordance to our analytical study of 2-level VSC during balanced mode operation.

Similar experiment has been performed and Matlab/Simulink model has been developed for NPC with $V_{DC} = 200V$ and 3-phase star-connected RL-load where$R = 100\Omega$ *and* $L = 5mH$. Fig.2.8 represents the schematic version of the experimental set-up.

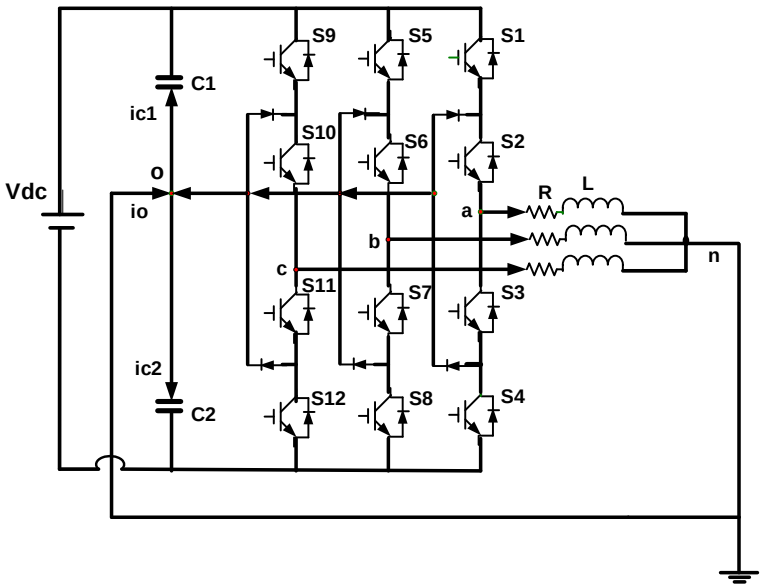

Fig.2.8 Schematic representation of the experimental tests on 3-phase 4-wires NPC during balanced power exchange condition between three output phases

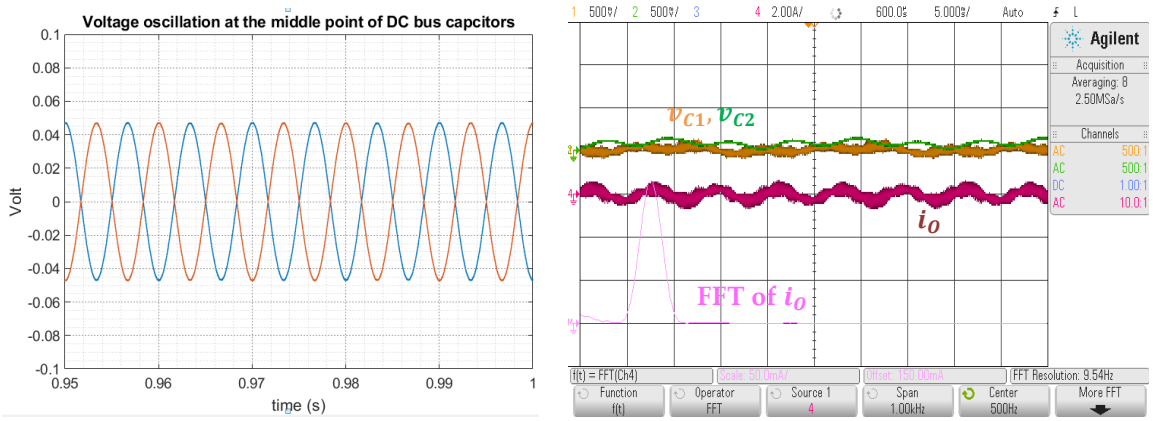

(a) (b)

Fig.2.9 DC-bus upper and lower capacitor voltages during the experimental tests on 3-phase 4-wires NPC during balanced power exchange condition between output three phases: a. time-domain simulation result b. experimental result

From Fig.2.9, it is observed that there are ±0.045V voltage oscillations at the middle point of the DC bus capacitors in NPC with the 3-phase balanced RL-load of 5mH and 100Ω for both in Matlab/Simulink and experimental test. During experimental test, oscilloscope channels 1 and 2 are set in AC coupling mode in order to measure only the ripples of the DC-bus capacitor voltages and channel 4 measures the current flowing between middle point of the DC bus and the inverter load terminal. This oscillation arises due to the structure of the NPC inverter where 150Hz current component is flowing between middle point of the DC bus and the inverter load terminal. As observed in Fig.2.9.b, Fast Fourier Transform (FFT) of this current (represented by pink waveform) includes only the 150Hz component as the FFT function of the oscilloscope has been set at the span of 1kHz.

Fig.2.10 compares the DC bus middle point voltage variation both in 2-level and 3-level VSC in balanced network condition. For the sake of comparison, resistive value to the RL-load has gradually been decreased from 100Ω to 40Ω with four test points in between, keeping all other conditions constant. As a result, current in the middle point of the DC-bus will increase and it will change the voltage variation accordingly. It is observed that there is no voltage oscillation at the middle point of the D.C bus in 2-level VSC with increase in phase current. However, voltage oscillation at the middle point of the DC-bus capacitors has been observed in 3-level VSC. This oscillation increases in 3-level VSC with increase in phase current. This result is normal due to the structure of both the inverters and the operating conditions. It has also to be noted that the oscillation of the NPC converter is at a frequency of 150Hz (3 times of the fundamental frequency). The capacitors, which can have an impact on the output current quality, have therefore been sized in order to limit this voltage variation in 3-level VSC.

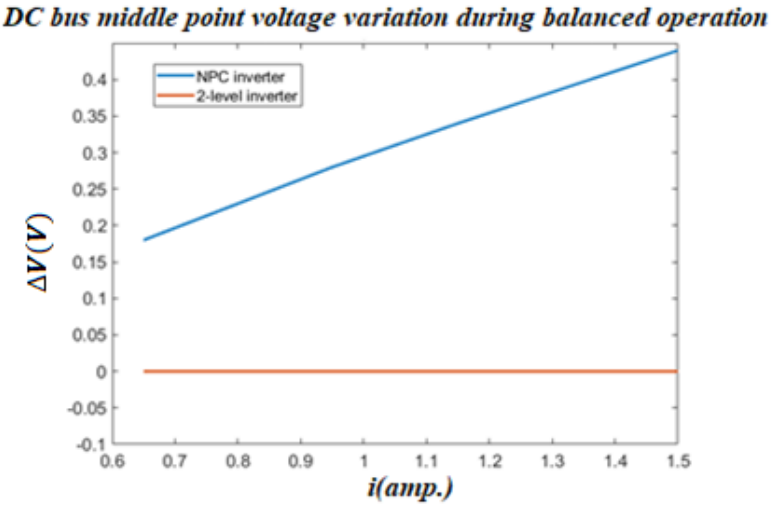

Fig.2.10 Comparison of voltage oscillations at the middle point of the DC-bus for both 2-level and 3-level VSI in balanced operating condition with experimental data

2.3.2 Single phase operation between one phase and the neutral point

In this case, single-phase operation is considered between one phase (for an e.g. a-phase) and the neutral point for 2-level and 3-level VSI (VSC is used as VSI). In this way, the single phase current is injected at the middle point (O) of the DC bus capacitors (C_1 andC_2). Fig.2.11 and Fig.2.12 represent the schematic of single phase operation for 2-level and 3-level VSI respectively.

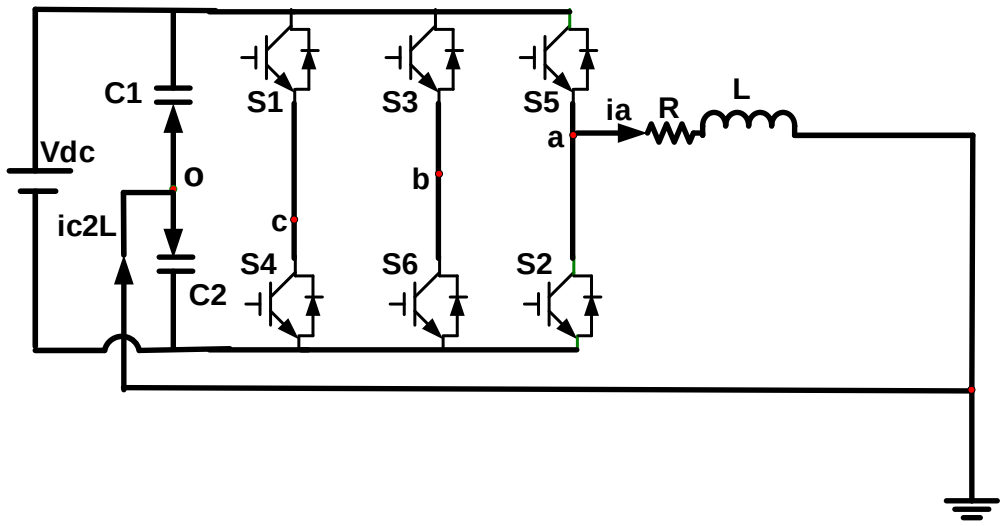

Fig.2.11 Single phase operation (e.g. a-phase) of 2-level VSI

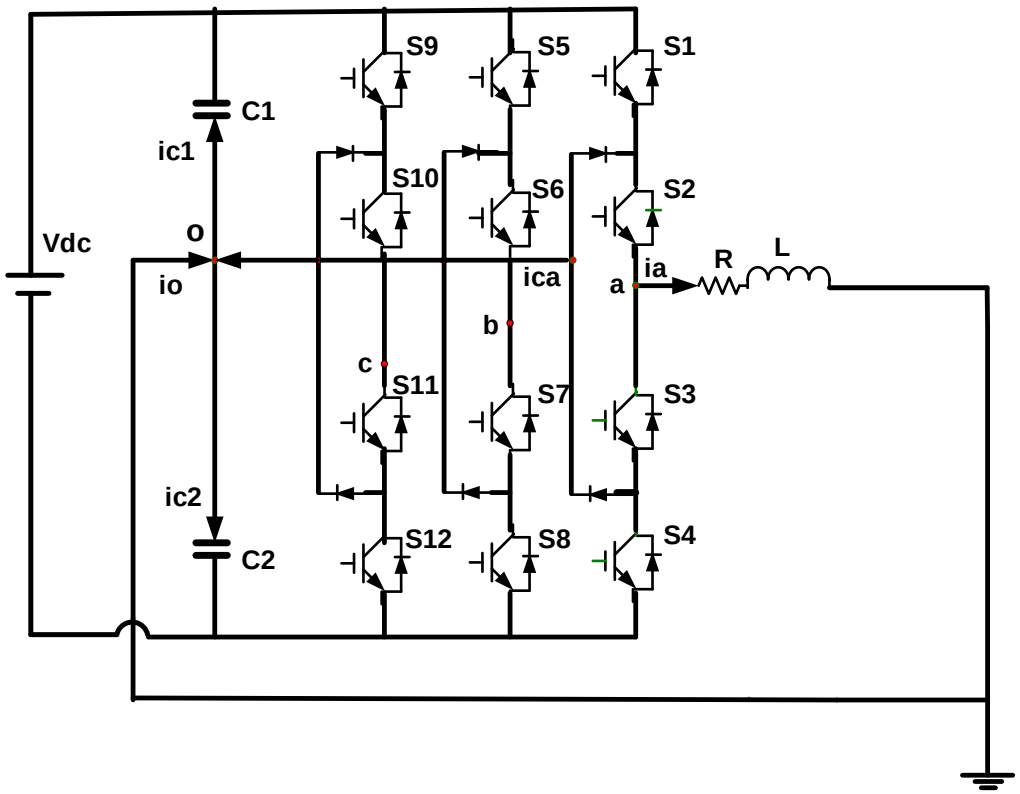

Fig.2.12 Single phase operation (e.g. a-phase) in 3-level VSI

Single-phase experimental tests have been performed for both 2-level and NPC VSI by connecting RL-load only to phase 'a'. Resistive values of the a-phase load are varied between 40Ω and100Ω, while inductor is constant at 5mH. DC- bus voltage is kept constant at 200V. Fig.2.13 presents the AC-voltage variations across C_1 and C_2 and their difference ($\Delta V = v_{c1} - v_{c2}$) in the middle point of the DC bus of 2-level VSI during test of single-phase operation with a 100Ω load. ΔV is varying between ±0.25V to ±0.35V in experimental measurements. These oscillations are due to the 50Hz current (i_{C2L}) in the neutral wire, connected to the middle point of the DC bus as shown in Fig.2.11.

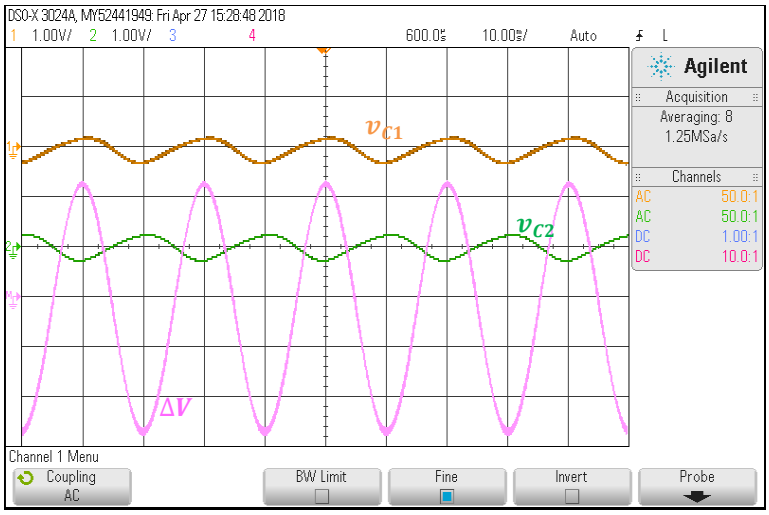

Fig.2.13 Voltage oscillations at the middle point of the DC-bus for 2-level VSI in single phase operation

Fig.2.14 presents the AC-voltage variation across C_1 andC_2, their difference ($\Delta V = v_{c1} - v_{c2}$) and FFT of ΔV in the middle point of the DC bus of 3-level VSI in experimental test of 1-ph operation. From FFT, it is observed that voltage oscillation at the middle point of the DC-bus occurs predominantly due to 50Hz current component of a-phase along with 150Hz current component that is coming from a-phase clamping diodes as the FFT function of the oscilloscope has been set at the span of 1 kHz. In test bench measurement, ΔV is varying between ±0.22V.

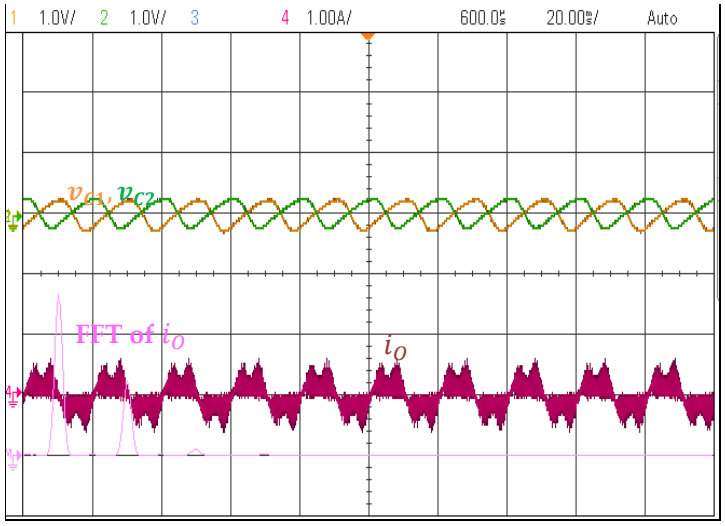

Fig.2.14 Voltage oscillations at the middle point of the DC-bus for 3-level VSI in single phase operation

As stated earlier, experiments with single phase load for both 2-level and 3-level VSI have been performed and ΔV values have been recorded for different operating points by varying the load resistance between 40Ω to100Ω. With these experiments, effect of 50Hz current component in 2-level inverter and both 50Hz and 150Hz current components in NPC on the voltage oscillation at the middle point of the DC-bus have been studied. From Fig.2.15, it is observed that the voltage oscillations at the middle point of DC bus is less in case of 3-level VSI compared to 2-level VSI. In addition, the rate of increment of ΔV is greater in 2-level inverter compared to NPC, with increment of power. This is because in case of 2-level VSI, full i_a current, which will increase with the increment of power, flows through 'O'. Whereas in case of NPC, there is a compensation effect on the current, which is flowing through 'O', by i_{ca} due to its' neutral connection. Thus, capacitors of higher ratings should be needed for 2-level VSI in comparison with 3-level VSI in order to limit ΔV. This in turn can increase the weight and the volume of the 2-level VSI. Thus, it can be concluded that 3-level VSI is better than 2-level VSI during single-phase operation for this particular point.

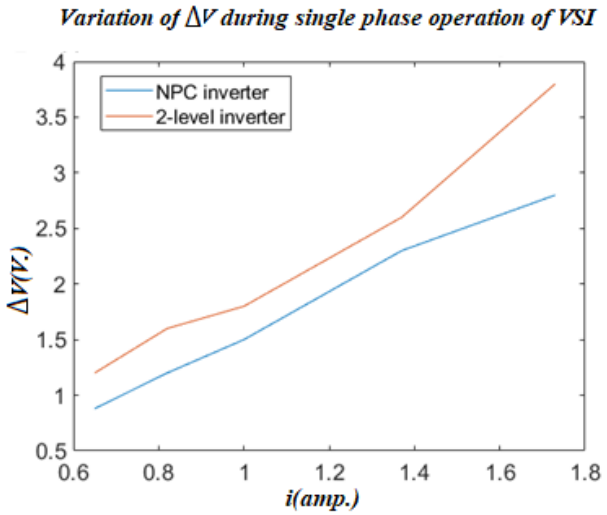

Fig.2.15 Comparison of voltage oscillations at the middle point of the DC-bus for both 2-level and 3-level VSI in single phase operation with experimental data

2.3.3 Unbalance power injection

In this case, study has been done on the impact of the injection of unbalanced current to the network on the middle point of the DC bus capacitors. For creating unbalance condition, different values of three active powers (P_1, P_2 and P_3) have been considered. The aim of injecting this current is to study the unbalances mitigation by the structure. For creating this scenario, a and b-phase loads are connected while disconnecting the c-phase load to do set-up like, $P_1 = P_2 = P\,W \neq P_3 = 0W$ due to the available test capacities. Fig.2.16 and Fig.2.17 represent the AC-voltage variations (v_{C2} and v_{C2}) across DC bus capacitors for 2-level and 3-level VSI respectively, considering $V_{\mathrm{DC}} = 200V$ and 100Ω, 5mH RL-load at 'a' and 'b'-phase while c-phase is kept open.

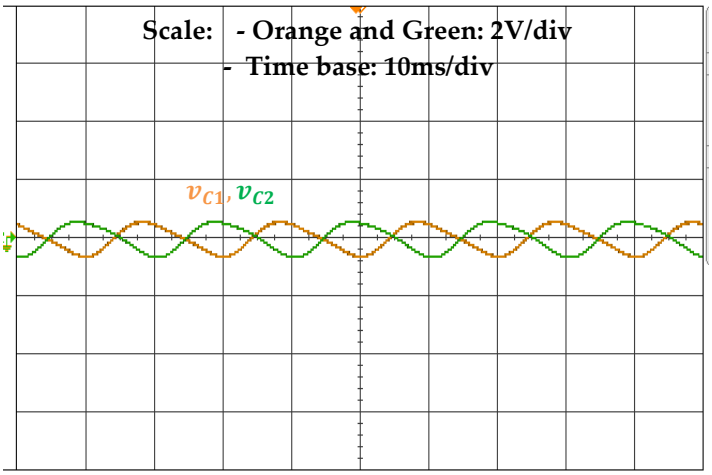

Fig.2.16 Voltage oscillations at the middle point of the DC-bus for 2-level VSI

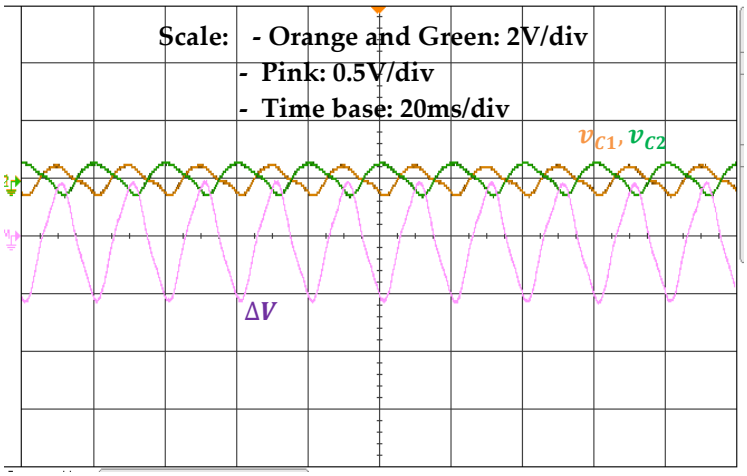

Fig.2.17 Voltage oscillations at the middle point of the DC-bus for 3-level VSI

Experiment has been performed and ΔV values have been recorded by injecting different values of power and therefore neutral current by changing the load from 100Ω to 40Ω at both 'a' and 'b' phases with four intermediate test points. From Fig.2.18, it is observed that the voltage oscillations at the middle point of DC bus is less in case of NPC compared to 2-level

VSC. In addition, the rate of increment of ΔV is greater in 2-level converter, with increment of power. Therefore, similar to single- phase operation, the unbalances have a more important effect on 2-level VSI than NPC.

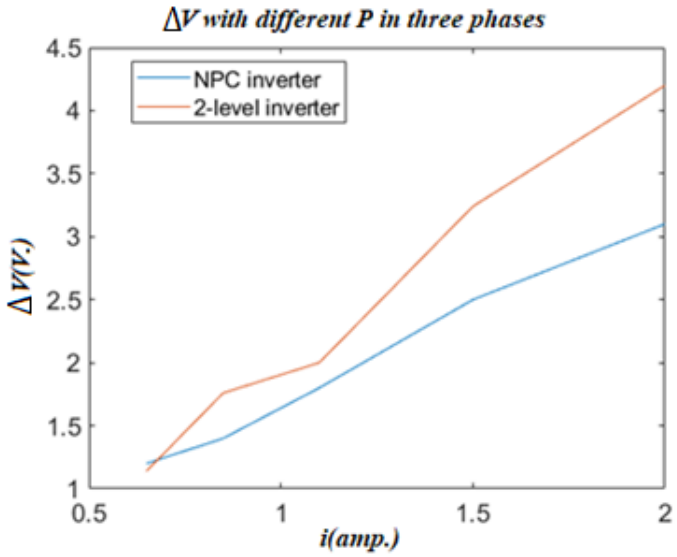

Fig.2.18 Comparison of voltage oscillations at the middle point of the DC-bus for both 2-level and 3-level VSI for different power injections in three phases with experimental data

In order to validate the developed model in Matlab/Simulink, comparisons have been done between simulation and experimental results for both 2-level and 3-level converters with same test parameters and shown in Fig.2.19. It is observed that the values and trend of increment of ΔV, for both time-domain simulation and the experimental results, are almost overlapping with each other and this in turn validates our developed time-domain model with the test bench.

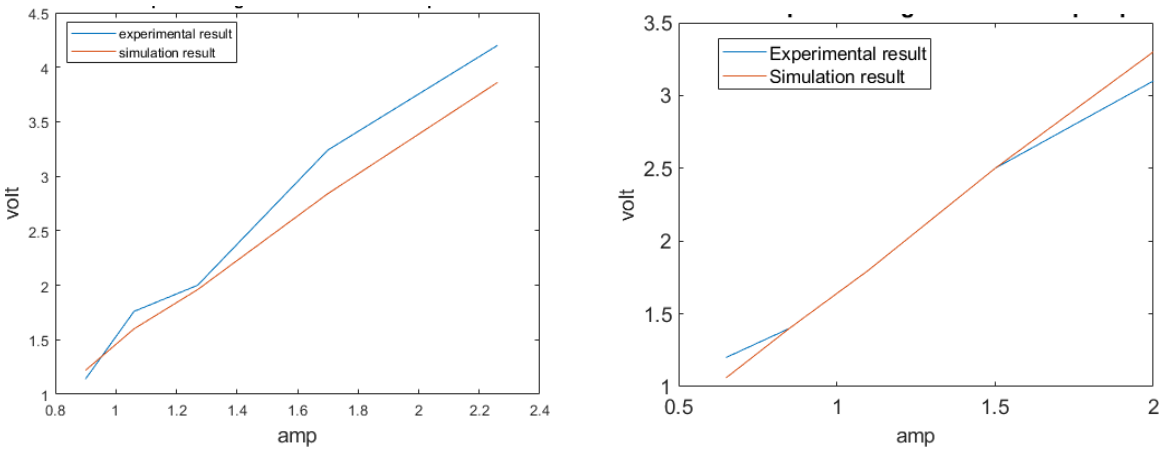

(a) (b)

Fig.2.19 Comparison of simulation and experimental results on voltage oscillations at the middle point of the DC-bus for different power injections a. 2-level b. 3-level VSI

Single-phase charging or future ancillary services can necessitate the injection of unbalanced currents into the grid and therefore it is necessary to add a neutral connection and to limit the capacitive middle point variation. With the help of analytical formulation, confirmed by the

time-domain based simulation as well as experimental tests, it can be concluded that in terms of oscillation at the middle point of the DC-bus, NPC is better than 2-level VSC during single phase operation and unbalance active and reactive powers [32] [65]. It will therefore allow using smaller capacitors in NPC for a specified ripple and making the integration easier. Thanks to Mathcad model, comparison between 4-wire 2-level and 3-level VSI has been done for different power exchanges, keeping$V_{DC} = 800V$. Minimum value of DC-bus capacitors are taken, considering the threshold of $\Delta v_C \leq 5\%\ of\ V_{DC} = 40V$ for NPC.

$C\ (\mu F)$	$P_1(kW)$	$P_2(kW)$	$P_3(kW)$	$Q_1(kVar)$	$Q_2(kVar)$	$Q_3(kVar)$	$\Delta v_{C3L}(V)$	$\Delta v_{C2L}(V)$
758	**7.36**	**0**	**0**	**0**	**0**	**0**	**40**	**86.2**
547	**7.36**	**3.68**	**3.68**	**0**	**0**	**0**	**40**	**74.7**
841	**7.36**	**0**	**0**	**0**	**-3.68**	**-3.68**	**40**	**95.4**
292	**2.3**	**-1.16**	**-1.16**	**0**	**-2.01**	**2.01**	**40**	**65.6**

Table 1: Comparison of DC-bus voltage oscillations between 4-wire 2-level and 3-level VSI in different power exchange conditions with different capacitors

2.4 DC-bus voltage calculation and passive elements design of the converter

In this section, DC-bus voltage of VSC has been calculated and designing of passive elements of the converter has been discussed. These are very important aspects concerning the amplitude of the sinusoidal output of VSC and weight and volume of the onboard EV battery charger.

2.4.1 Calculation of DC bus voltage of VSC

In order to have the right current across the phase, specific converter voltage need to be generated. The voltage current relationship in one phase (for an e.g. a) can be represented by below equivalent circuit:

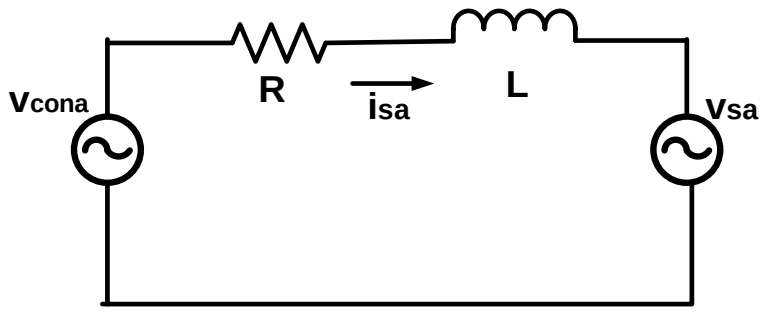

Fig.2.20 Simplified per phase equivalent circuit to represent the power transfer between AC/DC converter and the AC-grid

Normally AC/DC grid connected converter is working also as PFC. But in our case, we want to inject the reactive power also, if required by the grid. As a result, there will be a phase shift

(depending on the reactive power, it can be lag or lead) between supply voltage and current. Fig.2.21 represents the vector diagrams of the Fig.2.20. Usually voltage drop due to supply resistance is insignificant compared to the voltage drop across the source inductance, so it can be neglected.

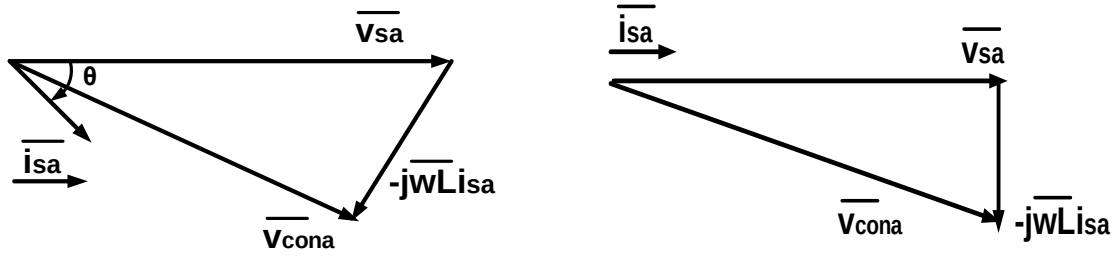

(a) *(b)*

Fig.2.21 Vector diagrams of the per phase equivalent circuit a. general case considering reactive power b. unity power factor operation considering zero reactive power

In general using Fig.2.21.a, $(\boldsymbol{v_{cona}})^2 = (\boldsymbol{v_{sa}})^2 + (\boldsymbol{\omega L i_{sa}})^2 + \mathbf{2} * \boldsymbol{v_{sa}} * \boldsymbol{\omega L i_{sa}} * \boldsymbol{sin\theta}$, where v_{cona} will change, depending on the reactive power.

However using Fig.2.21.b, we can write:

$$(\boldsymbol{v_{sa}})^2 + (\boldsymbol{\omega L i_{sa}})^2 = (\boldsymbol{v_{cona}})^2 \quad \textbf{(28)}$$

In our project, battery voltage and power of the converter are considered as 800V and 22kW respectively. So r.m.s value of per phase AC-current will be 32A. Considering$v_{sa} = 230V\ (r.m.s)$ and L=5mH, $v_{cona} = 235V$

The amplitude of the converter output directly depends on the voltage level of the DC-bus. The fundamental AC voltage equation of the inverter having split DC-bus (as shown in Fig.2.2 and Fig.2.3) and operated with SPWM strategy is given by [66]:

$$\boldsymbol{V_{cona}(rms)} = \mathbf{0.612} * \boldsymbol{m} * \frac{\boldsymbol{E}}{\mathbf{2}} \quad \textbf{(29)}$$

Where m: modulation index E: DC-bus voltage

Therefore, assuming a maximum modulation index of 0.9, $\boldsymbol{E \geq 853V}$

To verify the analytical formula of the relation between DC- bus voltage and the modulation index, simulation has been performed with$E = 800V, v_{acrms} = 230V$ and 22kW 3-ph active power exchange. In simulation, there is no voltage fluctuation or no loss occurred due to use of ideal devices or drivers. Thus analytical value of m, according to Equ. 29, will be 0.93 and this value is approximately equal with the obtained simulation result, shown in Fig.2.22.

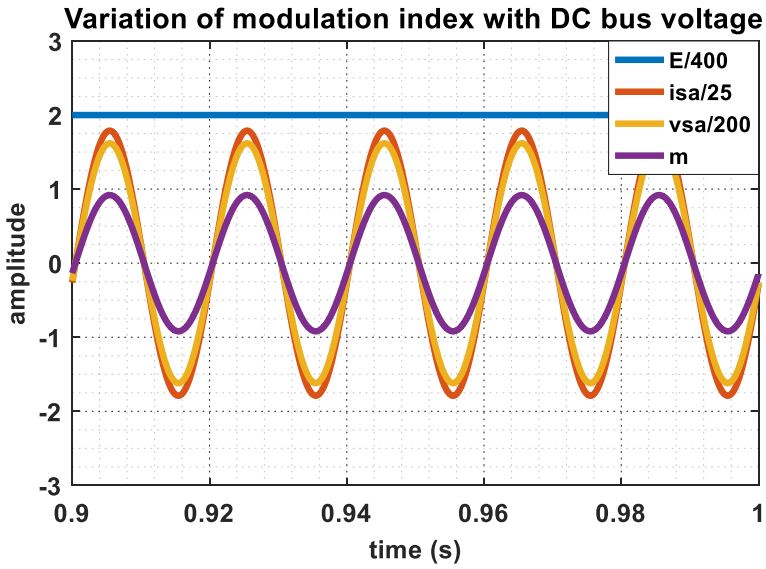

Fig.2.22 Variation of modulation index with change in DC bus voltage: $V_{DC} = 800V \quad m = 0.93$

2.4.2 Selection of grid side AC-inductor

AC filter is connected between IGBT/MOSFET based power converters and the grid. This filter is used for three purposes [67]:

1. Commercial grid-connected converters can be classified as voltage source/sinks while the AC grid side is also a voltage sink. In the definition of two port electrical component, if the input is the voltage, the output must be the current and vice-versa. This means a voltage source cannot be directly connected to a voltage sink. The AC-side inductor(L), connected between the converter and the grid, acts as a current source in order to connect the two separate voltages: converter output voltage (v_{conx}) and the grid voltage (v_{sx}).

2. It also filters the output current by attenuating high frequency current components, generated due to PWM switching and allows to have a state variable to control the input current and therefore power.

3. It helps to protect the converter switches (IGBTs/MOSFETs) from transients.

Design of the inductor depends on the switching frequency of the converter and the allowed current ripple, which is considered as 4.5% of the maximum current in our case.

The voltage across the inductor (v_L) is written as:

$$\boldsymbol{v_L = L\frac{di_L}{dt}}$$

Or, $$\boldsymbol{(v_{conx}(t) - v_{sx}(t)) = L\frac{di_L(t)}{dt}} \quad \textbf{(30)}$$

Where $x \in a, b \; and \; c$

i_L : Current flowing through the inductor

For half bridge inverter with one switching cycle, it can be written as:

$$\left(\boldsymbol{V_{DC} - d * \frac{V_{DC}}{2}}\right) = \boldsymbol{L\frac{\Delta i_{pp}}{dT_{SW}}}$$

$$\boldsymbol{Or, \Delta i_{pp} = \frac{dT_{SW} * \left(V_{DC} - d * \frac{V_{DC}}{2}\right)}{L}} \quad \textbf{(31)}$$

Where $T_{SW} = \frac{1}{f_{SW}}$, switching period and d: duty cycle

Considering Sinusoidal Pulse Width Modulation (SPWM) strategy,

$$\boldsymbol{d(\omega t) = m \sin \omega t} \quad \textbf{(32)}$$

Putting all these expressions in Equ. 31,

$$\boldsymbol{\Delta i_{pp} = \frac{m \sin \omega t * V_{DC} * (2 - m \sin \omega t)}{2 * L * f_{SW}}} \quad \textbf{(33)}$$

For calculation of extremum ripple,

$$\boldsymbol{\frac{d(\Delta i_{pp})}{dt} = 0} \quad \textbf{(34)}$$

Considering $K = \frac{m * V_{DC}}{2\omega L} = constant$,

$$\boldsymbol{\frac{d(\Delta i_{pp})}{dt} = K\{\cos \omega t\,(2 - m * \sin \omega t) - m * \sin \omega t * \cos \omega t\} = 0}$$

$$\boldsymbol{Or,\ \sin \omega t = \frac{1}{m}} \quad \textbf{(35)}$$

Putting the value of $\sin \omega t$ in Equ. 33,

$$\boldsymbol{\Delta i_{pp}\big|_{max} = \frac{V_{DC}}{2 * L * f_{SW}}}$$

$$\boldsymbol{Or,\ L = \frac{V_{DC}}{2 * f_{SW} * \Delta i_{pp}\big|_{max}}} \quad \textbf{(36)}$$

In case of multilevel inverter,

$$\boldsymbol{L_m = \frac{1}{n-1} * L} \quad \textbf{(37)}$$

Where n: level of the inverter [68]

To verify the analytical formula of designing grid connected AC-inductor for both 2-level and 3-level VSC, simulation has been performed considering same parameters in both the cases, which are:

1. 3-ph converter of 22kW
2. Per phase grid voltage: 230V (r.m.s)
3. Inductor of 5mH is connected between each phase of the converter and the grid
4. DC bus voltage (V_{DC}) = $800V$
5. Switching frequency of the converter (f_{SW})=20 kHz

Thus, per phase current flowing through the inductor:

$$i_L(rms) = \frac{22000}{3 * 230} = 32A$$

According to Equ. 36, calculated current ripple for 2-level inverter is:

$$\Delta i_{pp}\big|max = \frac{800 * 10^3}{2 * 20000 * 5} = 4A$$

According to Equ. 37, calculated current ripple for 3-level inverter is:

$$\Delta i_{pp}\big|max = \frac{800 * 10^3}{2 * 2 * 20000 * 5} = 2A$$

In order to verify these calculated results, simulation has been performed and the results have been shown in Fig.2.23 and Fig.2.24 for both 4-wire 2-level and 3-level VSC respectively.

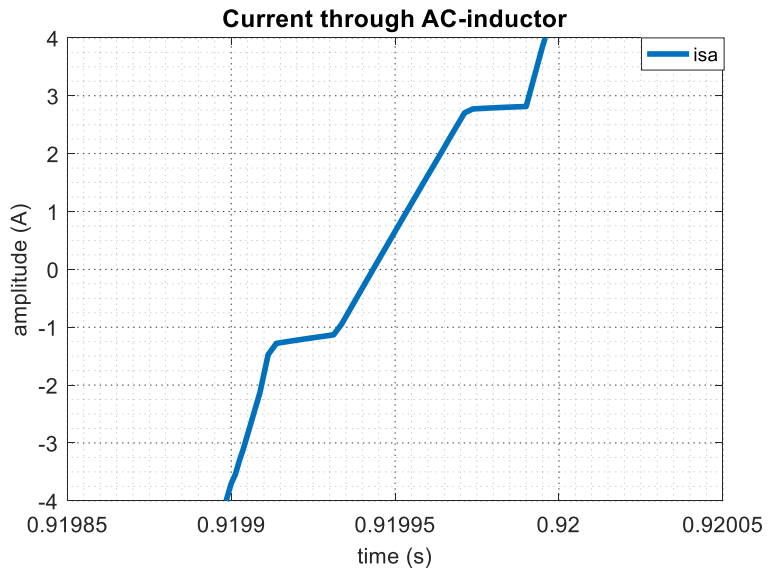

Fig.2.23 Current through AC- inductor in 2-level VSC

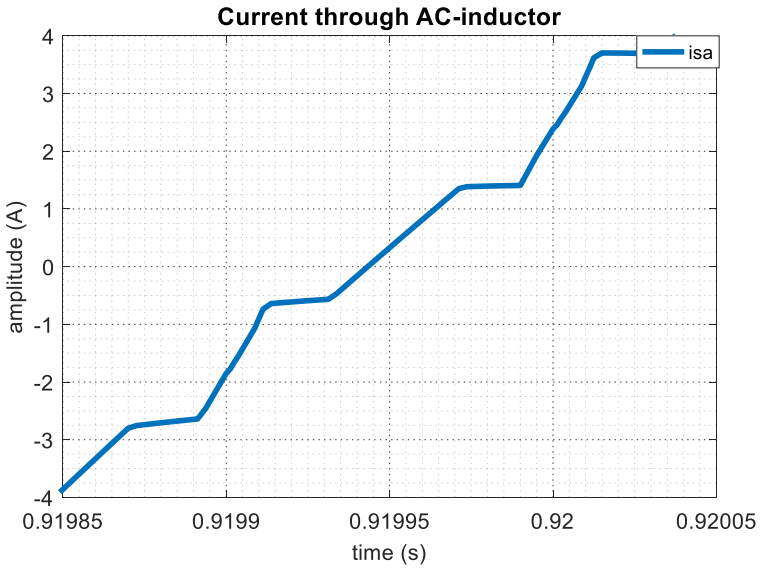

Fig.2.24 Current through AC- inductor in 3-level VSC

It is observed that simulated $\Delta i_{pp}|max = 3.85A$ and $1.9A$ for 2-level and 3-level VSC respectively and these values are in accordance to the calculated results.

Size of the inductor is very important for onboard battery charger. From the above simulation results, it is observed that the size of the AC-side inductor is half in NPC compared to that of 2-level converter for same percentage of allowed current ripple.

2.4.3 Design of DC-bus capacitor

Dimensioning of the DC-bus capacitors depends on the magnitude and frequency of the current flowing through the capacitor and the allowed voltage ripple. In NPC, two different currents with different frequencies exist:

- One current linked to the middle point of the DC-bus
- Another current linked to the DC-bus and the pulsed power

In NPC, summation of currents from each leg of the converter will flow through DC-bus capacitors. As discussed in Sec. 2.3.1, this current has a frequency of 150Hz (3-times of fundamental frequency) in balanced condition, which in turn creates the voltage fluctuation of 3ω in DC-bus capacitors. Analytical calculations of DC-bus capacitors and their validation in Matlab/Simulink have been done in the below section.

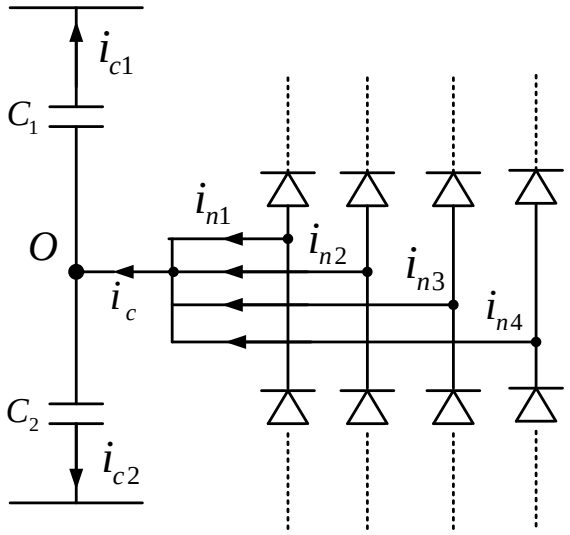

Fig.2.25 Different current components flowing through DC-bus capacitors in NPC

For 4-leg NPC,

$$\boldsymbol{i_{C1} = i_{C2} = \frac{i_C + i_n}{2} = \frac{i_{n1} + i_{n2} + i_{n3} + i_{n4}}{2}}$$

$$\boldsymbol{Or, i_{C1} = i_{C2} = \frac{S_a * i_a + S_b * i_b + S_c * i_c + S_n * i_{n4}}{2}} \quad \textbf{(38)}$$

2.4.3.1 Balanced power exchange condition

In balanced power exchange condition, $i_{n4} = 0$ as neutral current$i_n = 0$.
Current coming from a, b and c phases consisting of clamping diodes is expressed as:

$$\boldsymbol{i_{n1}}(\theta) = (\mathbf{1} - \boldsymbol{m}|\mathbf{sin}\,\theta|) * \boldsymbol{I_m}\,\mathbf{sin}\,\theta \quad \textbf{(39)}$$

According to Kirchhoff's Current Law (KCL),

$$\boldsymbol{i_C}(\theta) = \boldsymbol{i_{n1}}(\theta) + \boldsymbol{i_{n2}}(\theta) + \boldsymbol{i_{n3}}(\theta) \quad \textbf{(40)}$$

As $i_C(\Theta)$ consists of 150Hz component, the 3^{rd} harmonic component of $i_{n1}(\Theta)$ can be calculated by using Fourier series as shown below:

$$\boldsymbol{A_{in1\_H3} = \frac{2}{\pi}\int_0^{\pi} i_{n1}(\Theta).\cos(3\Theta)d\Theta}$$
$$\boldsymbol{Or, A_{in1\_H3} = \frac{2}{\pi}\int_0^{\pi}(1 - m|\sin\Theta|) * I_m \sin\Theta.\cos(3\Theta)d\Theta = 0} \quad \textbf{(41)}$$

$$\boldsymbol{B_{in1\_H3} = \frac{2}{\pi}\int_0^{\pi} i_{n1}(\Theta).\sin(3\Theta)d\Theta}$$
$$\boldsymbol{Or, B_{in1\_H3} = \frac{2}{\pi}\int_0^{\pi}(1 - m|\sin\Theta|) * I_m \sin\Theta.\sin(3\Theta)d\Theta = \frac{8m}{15\pi} * I_m} \quad \textbf{(42)}$$

Considering contribution of all 3-phases, total 3^{rd} harmonic component can be expressed as:

$$\boldsymbol{i_{C\_H3} = 3 * B_{in1_{H3}} = \frac{8m}{5\pi} * I_m} \quad \textbf{(43)}$$

The voltage ripple across the capacitor can be written as:

$$\boldsymbol{\Delta v_C = \frac{i_C}{C * 3\omega}}$$
$$\textbf{Or, } \boldsymbol{\Delta v_C = \frac{8m}{5\pi C * 3\omega} * I_m} \quad \textbf{(44)}$$

According to Equ. 29, calculated $m = 0.93$ for$E = 800V$ *and* $v_{acrms} = 230V$.

For 3-ph converter with 21kW power, current in each phase $(I_m) = \frac{7000*\sqrt{2}}{230} = 43A$

Considering allowed voltage ripple through DC-bus capacitor is 5% of E, i.e., $\Delta V_{pp} = 20V$

Thus, required capacitor will be: $C_1 = C_2 = \frac{8*0.93*43}{600\pi^2*50}$ =1.1mF

Considering C=4.7mF (as this capacitor is available for the test bench),

$$\Delta V_{pp} = \frac{8 * 0.93 * 43 * 10^3}{7050 * \pi^2} = 4.6V$$

Also from simulation result, shown in Fig.2.26, it is observed that the oscillation is around 4.4V, which validates our analytical calculations.

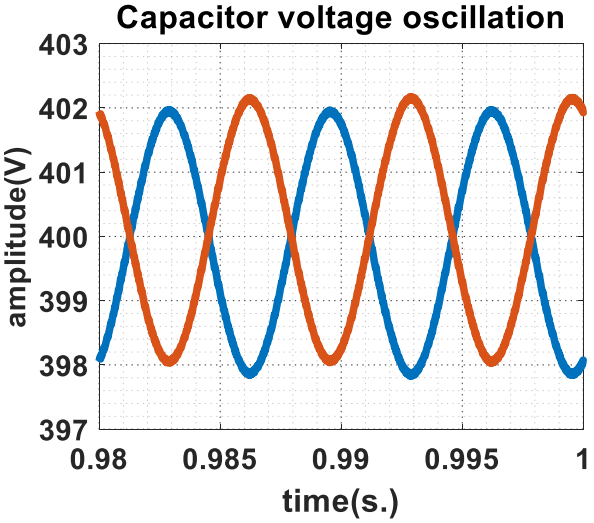

Fig.2.26 Voltage ripple through DC-bus capacitors in NPC during balanced power exchange

2.4.3.2 Unbalanced power exchange condition

In case of unbalance current injection condition, instantaneous power transfer theory is used to determine the capacitor rating.

Considering lossless converter,

$$\boldsymbol{p_{iac}(t) = p_{idc}(t)} \quad \textbf{(45)}$$

Where, $p_{iac}(t)$ = AC-side total instantaneous power

$p_{idc}(t)$ = DC-side total instantaneous power

$$\boldsymbol{p_{iac}(t) = \sum_{x=a,b,c} v_{ix}(t) * i_{ix}(t)} \quad \textbf{(46)}$$

Using Equ. 4-9, instantaneous AC-currents can be written as:

$$\boldsymbol{i_x(t) = I_{xm}\,\sin[(\omega t - \varphi_x) \pm \frac{2\pi}{3}\Big|_{c,b}]}$$

$$\boldsymbol{= \frac{\sqrt{2(P_x^2+Q_x^2)}}{v_x}\,\sin[\left(\omega t - tan^{-1}\frac{Q_x}{P_x}\right) \pm \frac{2\pi}{3}\Big|_{c,b}]} \quad \textbf{(47)}$$

Where $x \in a, b \text{ and } c$

Thus, instantaneous AC-power in each three phase can be calculated as:

$$\boldsymbol{p_{ix}(t) = \sqrt{(P_x^2 + Q_x^2)} * [cos\left(tan^{-1}\frac{Q_x}{P_x}\right) - cos\left((2\omega t - tan^{-1}\frac{Q_x}{P_x}) \pm \frac{4\pi}{3}\Big|_{c,b}\right)]} \quad \textbf{(48)}$$

Total instantaneous AC-power :

$$\boldsymbol{p_{itot}(t) = p_{ia}(t) + p_{ib}(t) + p_{ic}(t)}$$

$$\boldsymbol{= \left\{\sqrt{(P_a^2 + Q_a^2)} * cos\left(tan^{-1}\frac{Q_a}{P_a}\right) + \sqrt{(P_b^2 + Q_b^2)} * cos\left(tan^{-1}\frac{Q_b}{P_b}\right) + \sqrt{(P_c^2 + Q_c^2)} *\right.}$$

$$\boldsymbol{cos\left(tan^{-1}\frac{Q_c}{P_c}\right)\Big\} - \Big\{\sqrt{(P_a^2 + Q_a^2)} * cos\left(2\omega t - tan^{-1}\frac{Q_a}{P_a}\right) + \sqrt{(P_b^2 + Q_b^2)} * cos\left(2\omega t - \frac{4\pi}{3} -\right.}$$

$$\boldsymbol{\left.tan^{-1}\frac{Q_b}{P_b}\right) + \sqrt{(P_c^2 + Q_c^2)} * cos\left(2\omega t + \frac{4\pi}{3} - tan^{-1}\frac{Q_c}{P_c}\right)\Big\}} \quad \textbf{(49)}$$

$$\textbf{Or, } \boldsymbol{p_{itot}(t) = P + \tilde{p}(t)}$$

According to Equ. 49, this total power will come to the DC-side of the converter. But DC component (P) will flow through the battery whereas,$\tilde{p}$ that includes 100Hz component, will flow through the DC-bus capacitors.

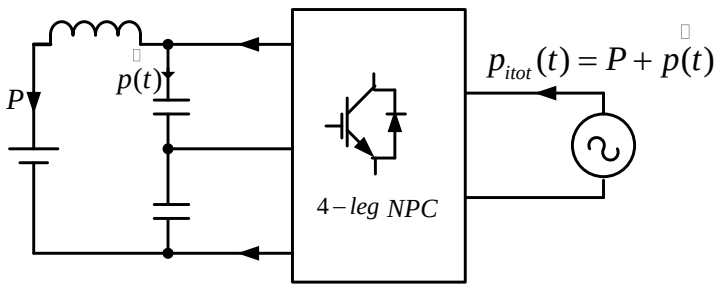

Fig.2.27 Instantaneous power transfer through NPC

The 100 Hz AC-component that creates the oscillation in the DC-bus capacitors is:

$$\tilde{p}(t) = -\left\{\sqrt{(P_a^2 + Q_a^2)} * cos\left(2\omega t - tan^{-1}\frac{Q_a}{P_a}\right) + \sqrt{(P_b^2 + Q_b^2)} * cos\left(2\omega t - \frac{4\pi}{3} - tan^{-1}\frac{Q_b}{P_b}\right) + \sqrt{(P_c^2 + Q_c^2)} * cos\left(2\omega t + \frac{4\pi}{3} - tan^{-1}\frac{Q_c}{P_c}\right)\right\} \quad (50)$$

Current flowing through DC-bus capacitors can be written as:

$$i_c(t) = \frac{\tilde{p}(t)}{V_{DC}} \quad (51)$$

Thus, the voltage ripple across the capacitor can be written as:

$$\Delta v_C = \frac{-1}{2\omega C V_{DC}}\left(\sqrt{(P_a^2 + Q_a^2)} * sin\left(2\omega t - tan^{-1}\frac{Q_a}{P_a}\right) + \sqrt{(P_b^2 + Q_b^2)} * sin\left(2\omega t - \frac{4\pi}{3} - tan^{-1}\frac{Q_b}{P_b}\right) + \sqrt{(P_c^2 + Q_c^2)} * sin\left(2\omega t + \frac{4\pi}{3} - tan^{-1}\frac{Q_c}{P_c}\right)\right) \quad (52)$$

Thanks to Mathcad model, minimum value of DC-bus capacitors can be calculated considering the threshold of $\Delta v_C \leq 5\%\ of\ V_{DC} = 40V$ where$V_{DC} = 800V$.

2.5 Conclusion

In this chapter, comparisons have been done amongst different configurations of AC/DC bidirectional VSCs. Different passive elements of VSC have also been designed in different network conditions. Based on these comparisons and ratings of the passive elements, NPC converter has been selected over 2-level VSC that will be suitable for AC/DC conversion part of bidirectional onboard EV battery charger. In addition, calculation has been done for DC-bus voltage level of VSC for achieving desired converter output.

Next chapter will introduce the comparison between 3-leg and 4-leg NPC converter. Apart from the additional opportunities provided by 4-leg NPC, neutral point voltage oscillation may further be reduced with the help of its control strategy. For this purpose, closed loop control strategy of the 4-leg NPC with its validation in both Matlab/Simulink and Hardware-in-Loop (HIL) [69] simulation has been presented in Chapter 3.

Chapter 3

AC/DC CONVERTER CONTROL

This chapter introduces the control strategy of the proposed 4-leg NPC converter, which is used as AC/DC bidirectional converter part of the onboard EV charger with V2G application.

3. Introduction

Power electronic converters are intermediate black box that connect various loads to the power sources (it can be either AC or DC sources). In our case, it will connect the battery system to the grid in order to allow the desired services. Suitable control strategy must be developed for operating these converters. In this chapter, control strategy and design of the controllers for the 4-leg NPC, which has been used as an AC/DC converter in bidirectional EV battery charger, have been discussed.

3.1 Generation of switching pulses for 3-level NPC converter

There are several modulation techniques for generating the gate pulses of the converter switches in order to convert the applied DC input voltage to an AC output voltage and also vice versa as shown in Fig.3.1 [70] [71] [72]. Also, we want a strategy that can generate higher switching frequency for easy filtering of higher order harmonics. SVPWM strategy, which can generate higher switching frequency, is not suitable in our case as sometimes it is tricky to implement when converter has a neutral connection. With this neutral connection configuration of the converter, SVPWM strategy can inject third harmonic voltage which induces third harmonic current in the neutral. Considering these criteria, SPWM modulation technique has been chosen that is easy to implement and can be used in higher-level converter topologies.

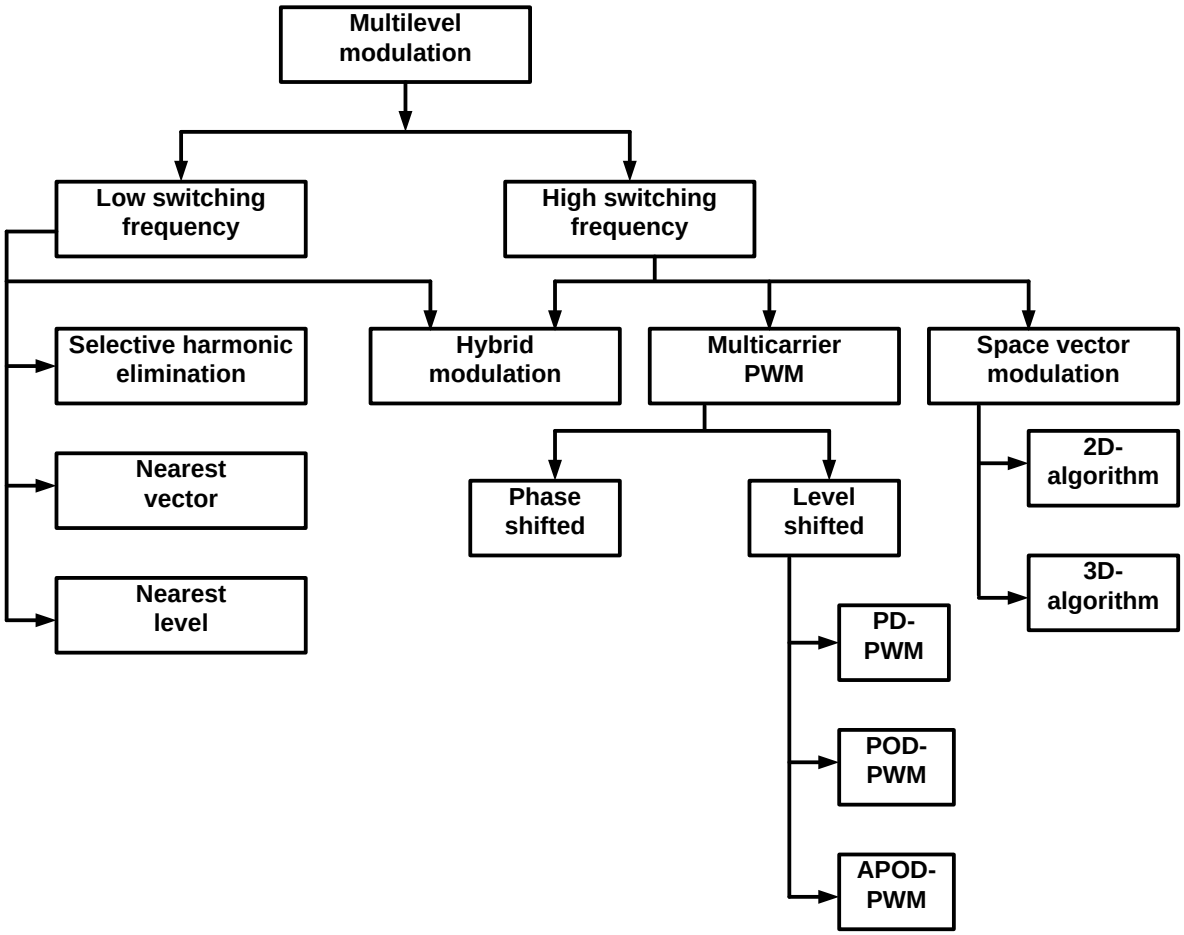

Fig.3.1 Classification of modulation techniques for converter

Multicarrier PWM strategy is mainly used in multilevel converter. In this strategy, $n-1$ carrier signals are required for n-level of converter. For 3-level NPC converter, two triangular waves (as carriers) of same frequency are compared with a sinusoidal reference signal. Phase Disposition (PD-PWM) modulation technique, where two carrier waves are in phase, has been used in our Matlab/Simulink model for generating the gate pulses of NPC as shown in Fig.3.2.

For a NPC-leg, as shown in Fig.3.3, $S1$ *and* $S3$ are the complimentary switches, i.e., when $S1$ is ON $S3$ will be OFF and vice-versa. Similarly $S2$ *and* $S4$ are also complimentary switches. The first carrier wave(v_{triU}), varied within 0 to 1, is compared with the positive half cycle of the modulating signal (v_{ref}) and switch S1 and its complementary switch S3 of NPC are operated. The second carrier wave, varied between -1 to 0, is compared with the negative half cycle of v_{ref} and Switch S2 and its complementary switch S4 are operated [73].

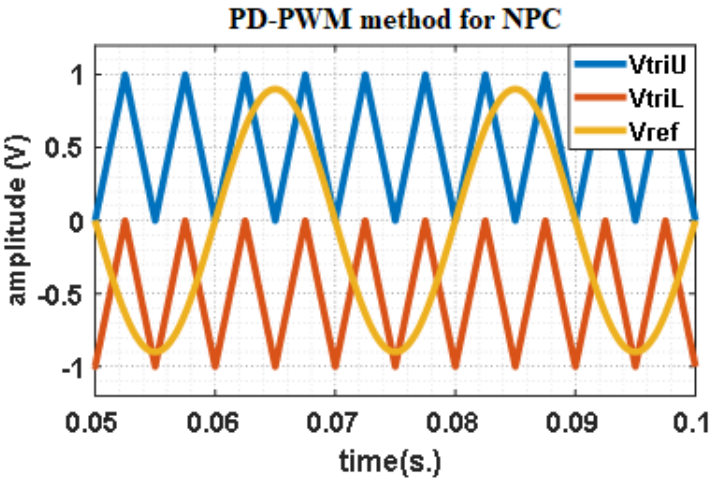

Fig.3.2 PD-PWM scheme for NPC converter

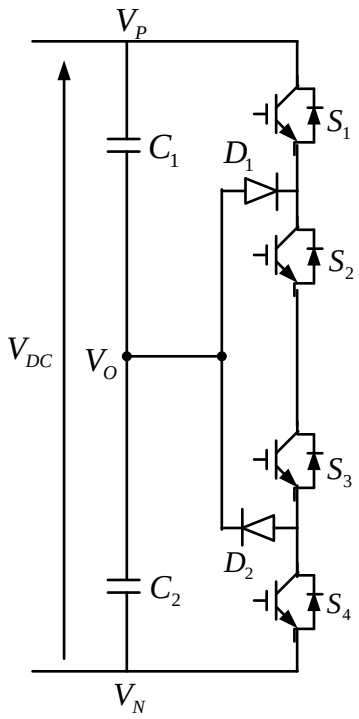

Fig.3.3 Single leg of NPC with DC-bus

In Fig.3.2, 200Hz carrier signals are used for better clarity of the picture and the understanding of the method. However, 20 kHz carrier signals are used in Matlab/Simulink model of closed loop control of NPC converter.

3.1.1 Output voltages of 3-level NPC converter

The NPC inverter can produce the three voltage levels at the output, based on the switching patterns of the leg as shown in Fig.3.3.

1. DC-bus positive voltage: When the upper half switches ($S1$ *and* $S2$) of the leg are turned on and remaining switches are turned off, the output pole voltage of the corresponding phase will be $V_{po} = \frac{V_{DC}}{2}$ (Considering$C_1 = C_2 = C$).

2. Zero voltage: When $S2$ *and* $S3$ are on and $S1$ *and* $S4$ are turned off, the output pole voltage of the corresponding phase will be zero.

3. DC bus negative voltage: When the lower half switches ($S3$ *and* $S4$) of the leg are turned on and the remaining switches are turned off, the output pole voltage of the corresponding phase will be $V_{no} = -\frac{V_{DC}}{2}$ (Considering $C_1 = C_2 = C$) [74].

Switching states (ON=1 and OFF=0) and the corresponding output voltages of NPC converter have been summarized with the help of *Table 2.*

S_1	S_2	S_3	S_4	Output voltage
1	1	0	0	$\frac{V_{DC}}{2}$
0	1	1	0	0
0	0	1	1	$-\frac{V_{DC}}{2}$

Table 2: Switching states and corresponding output voltages of NPC

In order to verify the theory of the NPC converter output voltages, simulation and experiment have been performed with V_{DC} =800V, m=0.93 and$f_{SW} = 20kHz$. NPC converter phase (a-phase) and phase to phase (a-phase to b-phase) voltages are represented by Fig.3.4 and Fig.3.5 respectively. With the test parameters, it is observed that phase voltage has steps of ±400V while phase-to-phase voltage has steps of 0, ±400V and ±800V, which are on accordance with the theory of NPC converter output voltages.

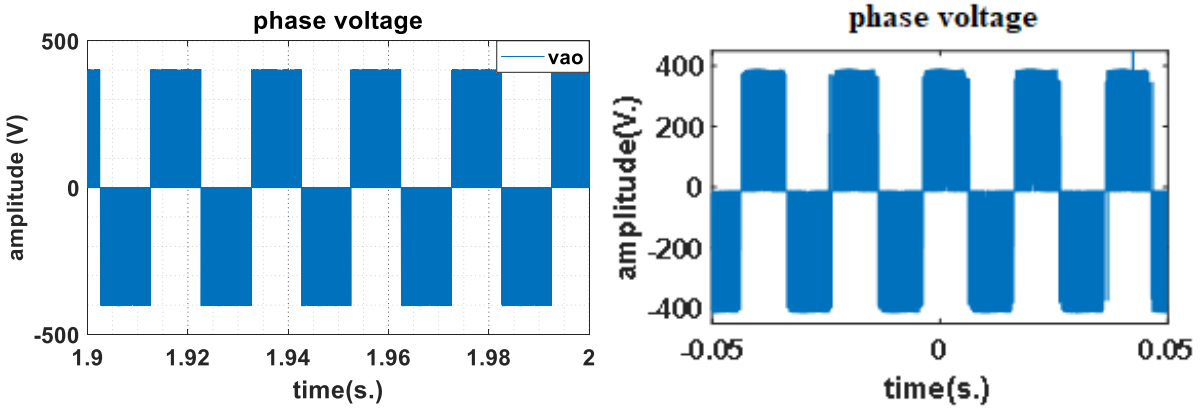

(a) *(b)*

Fig.3.4 Phase voltage of NPC converter (a) simulation (b) experimental

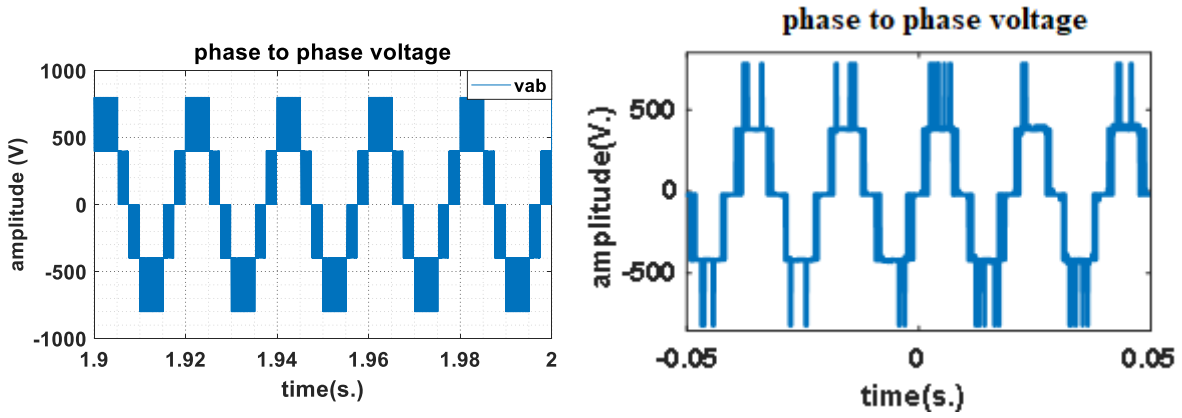

(a) *(b)*

Fig.3.5 Phase to phase voltage of NPC converter (a) simulation (b) experimental

3.1.2 Harmonic analysis of line to line voltage and line current of NPC converter

For any grid connected converter system, current distortion level is one of the most important parameters for power quality index [75][76]. According to the IEC standard 61727 and IEEE standard 1547-2003, THD of the grid current should be less than 5% in order to limit the adverse effects of the equipments connected to the grid [77][78][79][80]. Also there are limitations on individual harmonics, which are 4% for the odd harmonics from 3^{rd} to 9^{th} order while even harmonics are limited to 25% of the odd harmonic limits [73][81].

In order to respect the grid codes, the lower order harmonics should be attenuated and it can be done by using large filter. But at the same time it will increase the loss, cost, volume and weight of the converter. Thus, controlling of converter with proper PWM switching scheme is better option for limiting the harmonic distortion. The harmonic components, present in the phase-to-phase voltage and the phase currents of the NPC converter with PD-PWM modulation strategy, are :

1. $kf_{sw} \pm 2nf_1$, where k is odd integer and n can be any integer except 0 and multiple of 3. For an example, $f_{sw} \pm 2f_1, f_{sw} \pm 4f_1, f_{sw} \pm 8f_1,\ f_{sw} \pm 10f_1, f_{sw} \pm 14f_1$ and so on.

2. $kf_{sw} \pm nf_1$, where k is even integer and n can be any odd integer except multiple of 3. For an example, $2f_{sw} \pm f_1, 2f_{sw} \pm 5f_1, 2f_{sw} \pm 7f_1,\ 2f_{sw} \pm 11f_1, 2f_{sw} \pm 13f_1$ and so on.

Thus, harmonic of lower orders have almost been nullified with PD-PWM technique. THD will be better with increase in switching frequency. This has been validated with Matlab/Simulink model and results have been shown in Fig.3.6. It is observed that the NPC phase to phase voltage consists of major part of fundamental frequency (50Hz) and harmonic components of $nf_c \pm 1$ (n : integer and $f_c = \frac{f_{sw}}{f_1}$). In addition, THD of the grid current

(considering over first 40 harmonics) is approximatey equal to zero. Test parameters used for this validation are : $f_{sw} = 20kHz$, $V_{DC} = 800V$, $L_{ac} = 6.5mH$, $v_{grid}(r.m.s) = 230V$.

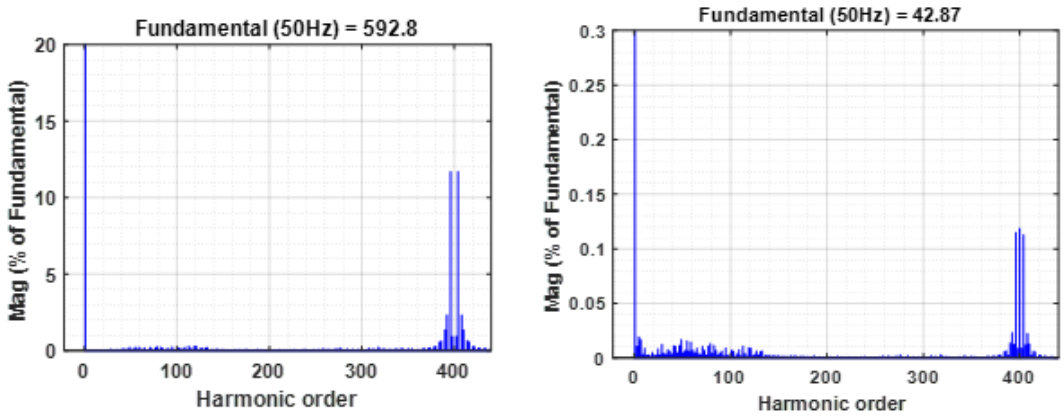

(a) *(b)*

Fig.3.6 FFT analysis of NPC converter with PD-PWM modulation strategy (a) phase to phase voltage (b) phase current

3.2 Phase locked loop

In simulation, grid voltage has fixed amplitude and frequency. But in reality, both of these amplitude and frequency of the grid voltage can vary independently within a range. Different control loops of a grid connected converter requires unit vectors ($sin\omega t$ and $cos\omega t$) (will be described in detail in Sec. 3.5 and Sec. 3.6) for proper operation [82]. These unit vectors depend on the real time frequency (as $\omega = 2\pi f$) of the grid voltage. Phase Locked loop (PLL) is an important unit for an efficient control of a grid connected converter [83] [84]. It detects the frequency deviation of the grid voltage and track that accurately and quickly. So that all the control loops of the grid connected converter can be properly synchronized with the grid system.

PLL circuit has been developed and verified experimentally thanks to grid emulator and FPGA programmed with LabVIEW. During test, both the amplitude and the frequency of the grid voltages were varied within 10% range of 230V (r.m.s) and 5% range of 50Hz respectively.

3.3 Overall control strategy of the 4-leg NPC converter

The global control strategy of the 4-leg NPC converter, that supports both balance and unbalance current injection operation, has been shown in Fig.3.7. For controlling the 4-leg NPC converter, four modulating signals need to be generated. Thanks to PD-PWM modulation strategy, these modulating signals will generate the gate pulses which are required for switching the IGBTs in the four legs. For this purpose, three current controllers are used for

generating the modulation signals and that will control the a,b and c-phase. Whereas one voltage controller is used for generating the modulting signal and that will control the neutral phase.

The control strategy has been realized in the Park domain (rotating dq0-reference frame) as shown in the following figure [85].

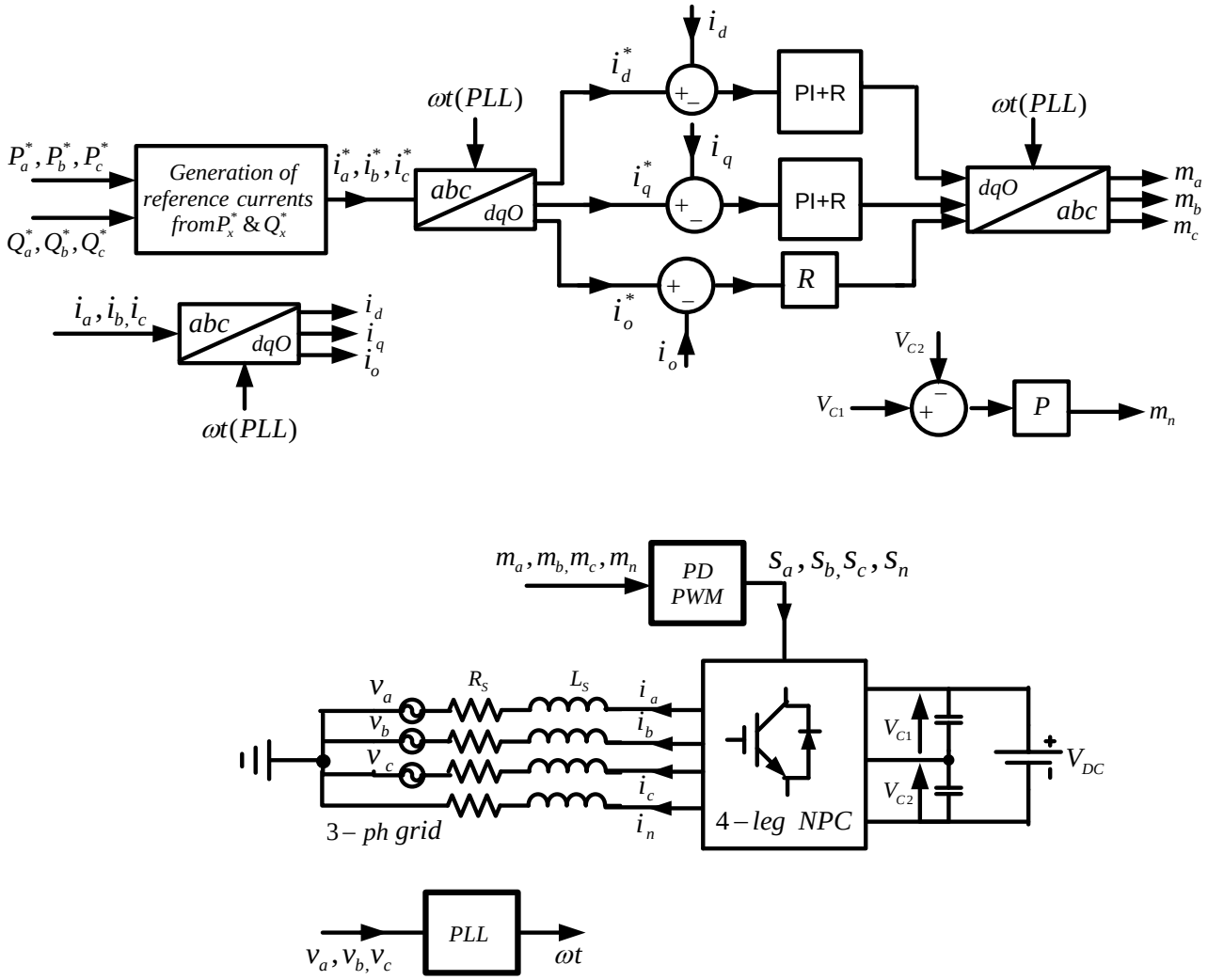

Fig.3.7 Overall control strategy of the 4-leg NPC

One of the main purposes of the converter is to inject active (P) and reactive (Q) power to the grid, if required. Thus, three phase active and reactive powers (P_x^* *and* Q_x^*) are the reference quantities that need to be controlled by the NPC converter. Current references (i_x^*) are generated from these power references, thanks to the mathematical expression written in Equ. 53. These reference currents are transformed into Park domain. Similarly, three phase grid currents (i_x) are sensed and transformed into Park domain which is expressed as:

$$\begin{bmatrix} u_d \\ u_q \\ u_0 \end{bmatrix} = \frac{2}{3} \begin{bmatrix} sin\omega t & sin(\omega t - \frac{2\pi}{3}) & sin(\omega t + \frac{2\pi}{3}) \\ cos\omega t & cos(\omega t - \frac{2\pi}{3}) & cos(\omega t + \frac{2\pi}{3}) \\ \frac{1}{2} & \frac{1}{2} & \frac{1}{2} \end{bmatrix} * \begin{bmatrix} u_a \\ u_b \\ u_c \end{bmatrix} \quad \textbf{(53)}$$

Where, u_x is a vector quantity.

The main characteristics of this conversion are [76]:

- Any rotating space vector generated by any number of phases (balanced/unbalanced, symmetrical/unsymmetrical) can be decomposed into two orthogonal axis variables. Thus, these variables will not have any mutual components that will affect each other.

- This transformation is good in terms of control point of the converter. Because synchronously rotating reference frame, dq0, makes all the balanced AC quantities into DC. These DC quantities can easily be controlled by PI controller. Because PI controller has advantages of: a. Zero steady state error b. Reduced effect of disturbance input or noise signals [86].

However, as we are in unbalanced conditions, this Park transformation behaves differently.

In case of unbalanced 3-phase system, for an e.g.

$$\boldsymbol{u_a = U_{m1} sin\omega t,\ \ u_b = U_{m2} sin(\omega t - \frac{2\pi}{3} + \varphi_1)\ \text{and}\ u_c = U_{m3} sin(\omega t + \frac{2\pi}{3} + \varphi_2)}$$

$$\boldsymbol{u_d = \frac{2}{3}(U_{m1} sin^2 \omega t + U_{m2} sin(\omega t - \frac{2\pi}{3}) sin(\omega t - \frac{2\pi}{3} + \varphi_1) + U_{m3} sin(\omega t + \frac{2\pi}{3}) sin(\omega t + \frac{2\pi}{3} + \varphi_2)}$$

$$\boldsymbol{Or, u_d = \frac{1}{3}(U_{m1} + U_{m2} cos\varphi_1 + U_{m3} cos\varphi_2) - \frac{1}{3}\Big[U_{m1} cos2\omega t + U_{m2} cos(2\omega t - \frac{4\pi}{3} + \varphi_1) + U_{m3} cos(2\omega t + \frac{4\pi}{3} + \varphi_2)\Big]} \quad \textbf{(54)}$$

$$\boldsymbol{u_q = \frac{2}{3}(U_{m1} sin\omega t cos\omega t + U_{m2} cos(\omega t - \frac{2\pi}{3}) sin(\omega t - \frac{2\pi}{3} + \varphi_1) + U_{m3} cos(\omega t + \frac{2\pi}{3}) sin(\omega t + \frac{2\pi}{3} + \varphi_2)}$$

$$\boldsymbol{Or, u_q = \frac{1}{3}(U_{m2} sin\varphi_1 + U_{m3} sin\varphi_2) + \frac{1}{3}\Big[U_{m1} sin2\omega t + U_{m2} sin(2\omega t - \frac{4\pi}{3} + \varphi_1) + U_{m3} sin(2\omega t + \frac{4\pi}{3} + \varphi_2)\Big]} \quad \textbf{(55)}$$

$$\boldsymbol{u_0 = \frac{1}{3}\Big[U_{m1} sin\omega t + U_{m2} sin\Big(\omega t - \frac{2\pi}{3} + \varphi_1\Big) + U_{m3} sin(\omega t + \frac{2\pi}{3} + \varphi_2)\Big]} \quad \textbf{(56)}$$

From the above calculations of 3-phase unbalance system, it is observed that:

- Both d-axis and q-axis components consist of a DC component and an AC-component of 100Hz (2f) frequency.
- 0-axis component consists of an AC-component of 50Hz (f) frequency.

Mathematical analysis of both 3-phase balanced and unbalanced systems have been verified by the simulation results which are shown in Fig.3.8 and Fig.3.9 respectively.

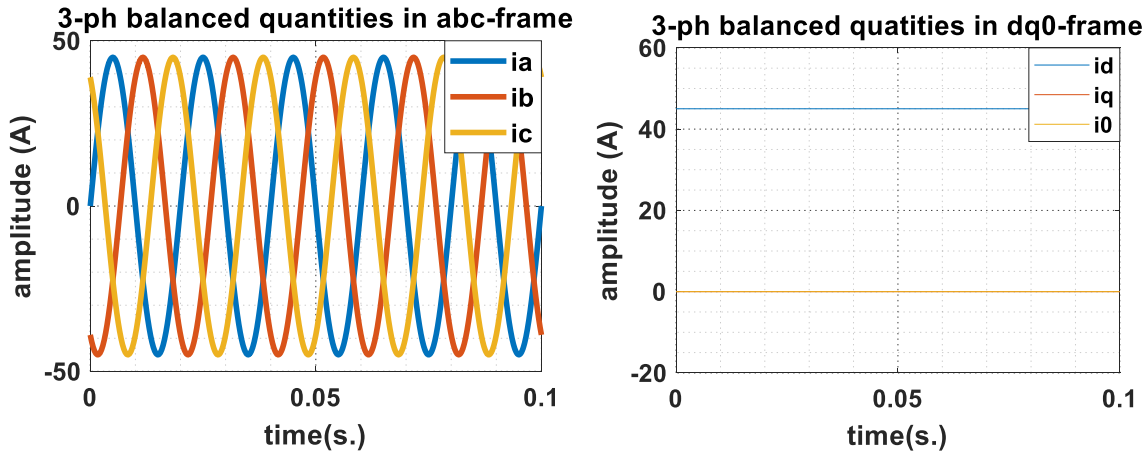

(a) *(b)*

Fig.3.8 abc to dq0 transformation of 3-ph balance system a. abc-reference frame b. dq0-reference frame

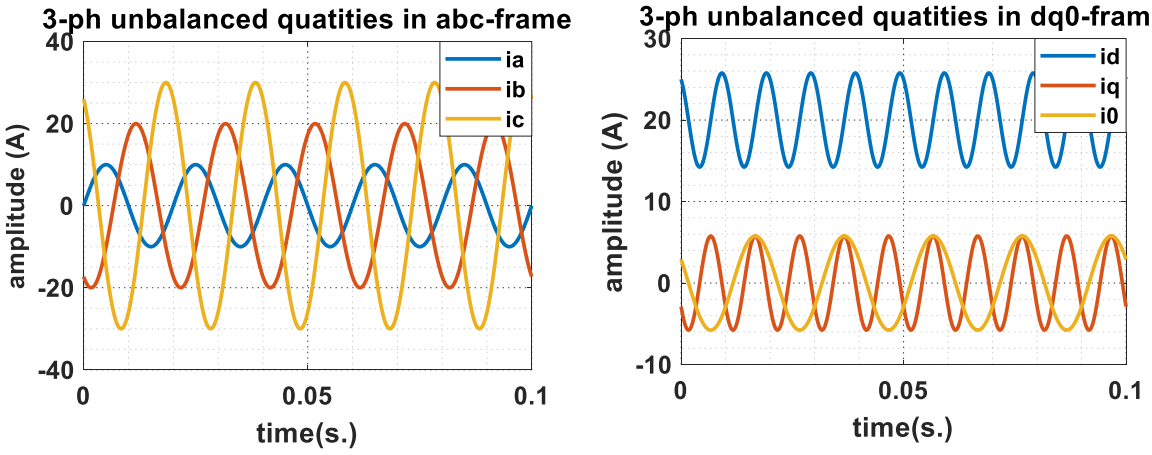

(a) *(b)*

Fig.3.9 abc to dq0 transformation of 3-ph unbalance system a. abc-reference frame b. dq0-reference frame

Both these Park domain reference and measured currents are compared and the errors have been passed through d-axis, q-axis and 0-axis current controllers. In case of 3-phase balanced system, PI-current controllers can be used for controlling the currents as all components are DC. However, for 3-phase unbalanced systems, PI and Resonant (R) controllers with resonance at 100Hz can be used for controlling d and q-axis currents whereas R controller, with resonance at 50Hz, can be used for controlling 0-axis current [87][88]. Modulating signals for 3-legs, connecting to a,b and c-phase, are generated by transfroming the output of the current controllers to abc-reference frame by using inverse Park transformation. The inverse Park transformation matrix is expressed as:

$$\begin{bmatrix} u_a \\ u_c \\ u_c \end{bmatrix} = \begin{bmatrix} sin\omega t & cos\omega t & 1 \\ sin(\omega t - \frac{2\pi}{3}) & cos(\omega t - \frac{2\pi}{3}) & 1 \\ sin(\omega t + \frac{2\pi}{3}) & cos(\omega t + \frac{2\pi}{3}) & 1 \end{bmatrix} * \begin{bmatrix} u_d \\ u_q \\ u_0 \end{bmatrix} \quad (57)$$

For both these Park and inverse Park transformation, unit vectors ($sin\omega t\ and\ cos\omega t$) are required and they can be generated by PLL strategy described in Sec. 3.2.

Voltages, across the DC-bus capacitors of the NPC, are also need to be controlled. For that purpose, DC-bus capacitor voltages are sensed, compared and passed through the proportional voltage controller. Output of this voltage controller will generate the modulating signal required for the leg connecting to the neutral terminal of the AC-grid. Switching signals for 4-leg NPC will be generated by PD-PWM modulation strategy (as explained in Fig.3.2), thanks to these four modulating signals (m_x).

3.3.1 Generation of reference currents from reference powers

In order to validate the equations of reference currents generation, simulation has been done with the parameters of $P_a = P_b = P_c = 7kW$ and $Q_a = Q_b = Q_c = 0kVAr$ for $0 \leq t \leq 1s$. Parameters are changed to $P_a = 2.3\ kW, P_b = -1.16kW, P_c = -1.16kW$ and $Q_a = 0kVAr, Q_b = -2.01kVAr, Q_c = 2.01kVAr$ at $t > 1s$.

With 230V grid phase voltage (r.m.s),
$I_{am} = I_{bm} = I_{cm} = \frac{\sqrt{2}*7000}{230} = 43A$ for $0 \leq t \leq 1s$.
In addition, these currents are 120° phase apart, thus $i_n^* = 0$ for $0 \leq t \leq 1s$.

At $t > 1s$., reference powers are considered in such a way, that we can test our control strategy for one of the worst unbalance conditions. The sizing of the converter is done for a current of 32A (r.m.s) in each leg. The characteristic of this test point of unbalance condition is that all three phases One test point to achieve this unbalance condition is that all three phase currents of a, b and c will have the same magnitude [$i_a^* = i_b^* = i_c^* = 10.6A(rms)$] and be in phase. Neutral current will not only be the summation of a, b and c-phase currents but also 180° out of phase to them.

With this criteria, reference active and reactive powers are calculated as:

$$\text{So, } \boldsymbol{P_a = v_a i_a \cos 0^\circ = 2.3kW\ and\ Q_a = v_a i_a \sin 0° = 0kVAr} \quad \textbf{(58)}$$

$$\boldsymbol{P_b = v_b i_b \cos 120^\circ = -1.16kW\ \ and\ \ Q_b = -v_b i_b \sin 120° = -2.01kVAr} \quad \textbf{(59)}$$

$$\boldsymbol{P_c = v_c i_c \cos 240^\circ = -1.16kW\ \ and\ \ Q_c = -v_c i_c \sin 240° = -2.01kVAr} \quad \textbf{(60)}$$

These analytical calculations have been validated with the simulation results shown in Fig.3.10.

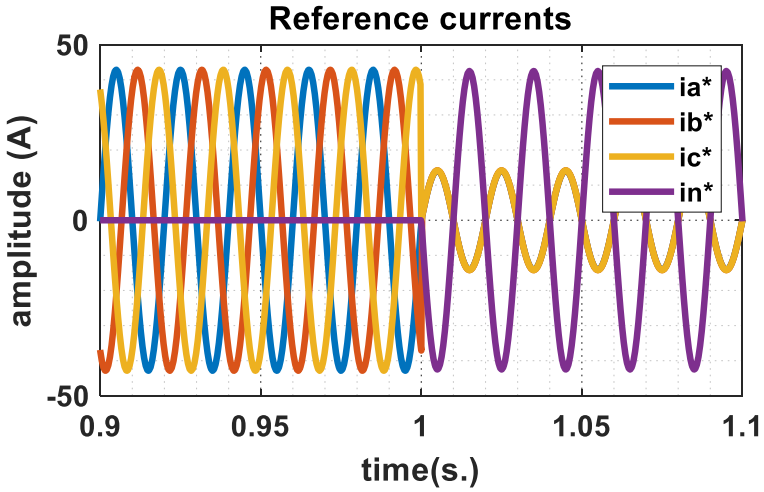

Fig.3.10 Generation of reference currents from active and reactive power references

3.4 Design of controllers for NPC converter

NPC topology, as shown in Fig.2.3, has four control loops: three current control loops and one voltage control loop. Three current control loops includes dq0-axis current controllers and the main purpose of the current control loop is to generate the appropriate current that will follow the reference current generated by reference active (P_x^*) and reactive power(Q_x^*). Whereas, voltage control loop is required to keep the voltage difference, at the middle point of the DC-bus of NPC, within a limit (ideally as small as possible).

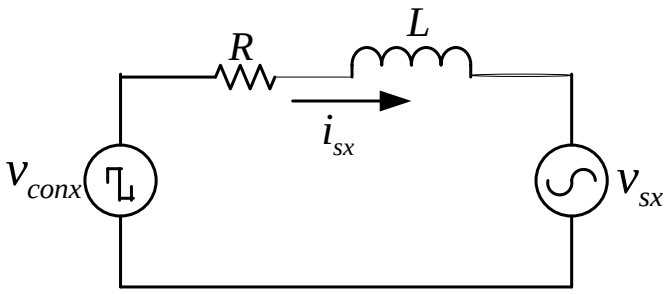

Fig.3.11 Equivalent circuit of the grid connected converter per phase ($x \in a, b \text{ and } c$)

From Fig.3.11, the equations related to grid voltages, converter output voltages and currents could be written as [89]:

$$\boldsymbol{v_{cona} = Ri_{sa} + L\frac{di_{sa}}{dt} + V_{sa}} \quad \textbf{(61)}$$

$$\boldsymbol{v_{conb} = Ri_{sb} + L\frac{di_{sb}}{dt} + V_{sb}} \quad \textbf{(62)}$$

$$\boldsymbol{v_{conc} = Ri_{sc} + L\frac{di_{sc}}{dt} + V_{sc}} \quad \textbf{(63)}$$

Where $L = AC - side\ inductance$ $\qquad$ $R = resistance\ associated\ to\ L$

These voltage equations in synchronously rotating reference frame (dq0) can be written as:

$$\boldsymbol{Ri_d + L\frac{di_d}{dt} = V_{cond} - V_{sd} - \omega L i_q} \quad \textbf{(64)}$$

$$\boldsymbol{Ri_q + L\frac{di_q}{dt} = V_{conq} - V_{sq} + \omega L i_d} \quad \textbf{(65)}$$

$Or, \boldsymbol{Ri_q + L\frac{di_q}{dt} = V_{conq} + \omega L i_d}$ [$V_{sq} = 0$ as for balanced 3-phase system, v_s does not have any quadrature component]

$$\boldsymbol{Ri_0 + L\frac{di_0}{dt} = V_{con0} - V_{s0}} \quad \textbf{(66)}$$

$Or, \boldsymbol{Ri_0 + L\frac{di_0}{dt} = V_{con0}}$ [$V_{s0} = 0$ as for balanced 3-phase system, v_s does not have any zero component]

The transformation in Park-domain produces two cross-coupling terms $\omega L i_d \; and \; \omega L i_q$ for q-axis and d-axis respectively. In order to have independent control of d-and q-axis current controllers, compensating terms are used for decoupling and it is defined as followed:

$$\boldsymbol{V'_{cond} = -V_{cond} + V_{sd} + \omega L i_q} \quad \textbf{(67)}$$

$$\boldsymbol{V'_{conq} = -V_{conq} - \omega L i_d} \quad \textbf{(68)}$$

Putting theses compensating term in Equ. 64 and 65,

$$\boldsymbol{Ri_d + L\frac{di_d}{dt} = V'_{cond}} \quad \textbf{(69)}$$

$$\boldsymbol{Ri_q + L\frac{di_q}{dt} = V'_{conq}} \quad \textbf{(70)}$$

Transforming Equ. 69 and 70 into s-domain:

$$\frac{\boldsymbol{i_d(s)}}{\boldsymbol{V'_{cond}(s)}} = \frac{\boldsymbol{1}}{\boldsymbol{R+sL}} \quad \textbf{(71)}$$

$$\frac{\boldsymbol{i_q(s)}}{\boldsymbol{V'_{conq}(s)}} = \frac{\boldsymbol{1}}{\boldsymbol{R+sL}} \quad \textbf{(72)}$$

Equ. 71 and 72 are required to design the current controllers, which is discussed in the next section.

3.4.1 Design of current controllers

As both d and q-axis equations have a similar form, only d-axis equation is used for further analysis of controller design. The current controller loops will generate the reference signals for SPWM strategy.

As explained earlier, both PI and R controllers need to be designed. Designing of these PI and R-current controllers will be demonstrated in following Sec. 3.4.1.1 and 3.4.1.2 respectively.

3.4.1.1 Design of Proportional-Integral (PI) controller

Transfer function of PI-controller in s-domain can be represented as [90]:

$$C(s) = \left(K_p + \frac{K_i}{s}\right) \quad (73)$$

Where $K_p = proportional\ gain$ $K_i = integral\ gain$

Using Equ. 73, block diagram of closed loop control of d-axis current is shown in Fig.3.12.

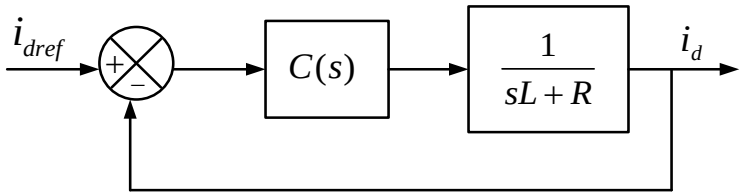

Fig.3.12 Closed loop control of d-axis current

Open loop transfer function of the system is given by,

$$G_O(s) = C(s) * \frac{1}{sL+R} = \frac{K_p+\frac{K_i}{s}}{sL+R} \quad (74)$$

Closed loop transfer function of the system will be:

$$G_c(s) = \frac{(sK_p+K_i)/L}{s^2+\left(\frac{R+K_p}{L}\right)s+\frac{K_i}{L}} \quad (75)$$

Comparing the denominator of Equ. 75 with the 2nd order transfer function: $s^2 + 2s\xi\omega_i + \omega_i^2$ [91]

$$K_p = 2\xi\omega_i L - R \quad (76)$$

Where ξ=damping factor and considered as 0.707

$$K_i = L\omega_i^2 \quad (77)$$

$$\omega_i = \frac{1}{t_i} = \frac{R}{L} \quad (78)$$

Considering $R = 0.1\Omega$ and$L = 6.5\ mH$, $\omega_i = 15.38\ rad.$, $K_i = 1.54$ $K_p = 0.04$

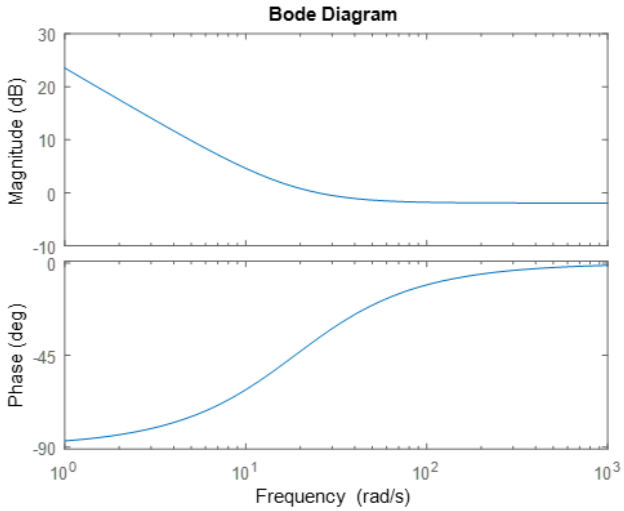

Fig.3.13 Bode diagram of d-axis PI current controller

Same calculations have been done for PI controller used for q-axis current.

3.4.1.2 Design of Resonant (R) controller

Two types of resonant controllers need to be designed for controlling the phase currents. First type of resonant current controller should work on 100Hz current components in d and q-axis currents whereas second type of R controller will control the 50Hz neutral current component. Bode plots of these two R-controller should be like Fig.3.14.

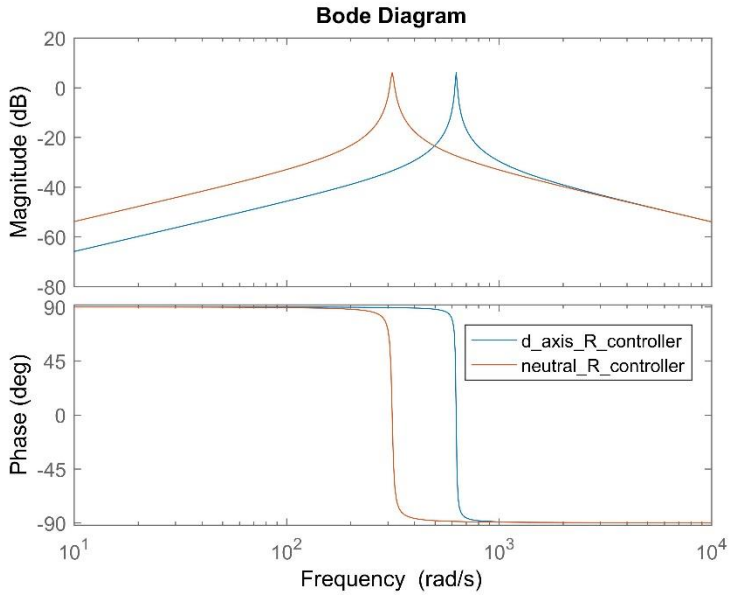

Fig.3.14 Bode diagrams of d-axis and neutral phase resonant current controllers

Constraint regarding designing of R-controller, required for controlling the 100Hz d and q-axis current components, is that it should not overlap with the operating zone of PI controller of the corresponding axis. Similarly, constraint regarding designing of R-controller, required to control the 50Hz 0-axis component, is both DC-bus middle point voltage controller (Proportional) and neutral current controller (Resonant) linked together. Therefore, they should also be decoupled.

For decoupling the effect of each other

- The gain margin of the PI-current controller and P-voltage controller should be much less than 100Hz and 50Hz respectively. As observed in Fig.3.13, gain crossover frequency of the PI current controller, used for both d and q-axis, is around 5Hz.
- Ideally except at 100Hz (for d and q-axis) and 50Hz (neutral current), there should not be positive magnitude gain of the resonant controller as observed in Fig.3.14.

This decoupling strategy of the neural current R-controller has been explained pictorially in Fig.3.15. This is exactly similar decoupling strategy between d and q-axis R current controllers with their corresponding PI current controllers.

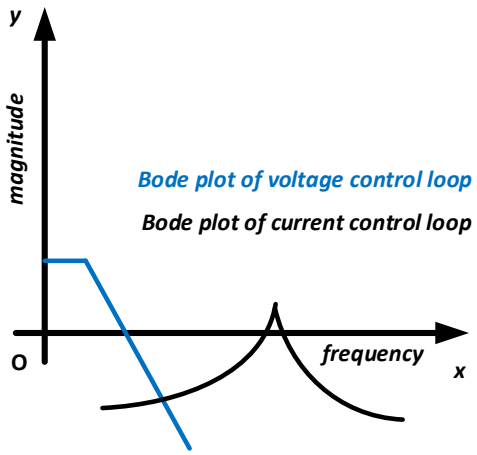

Fig.3.15 Strategy to decouple the effect of 0-axis current controller and capacitive middle point voltage controller

Transfer function of the resonant controller system can be written as [92] [93]:

$$\boldsymbol{G(s)} = \frac{\boldsymbol{K*2\omega_C s}}{\boldsymbol{s^2+2\omega_C s+\omega_0^2}} \quad \textbf{(79)}$$

Where K=gain factor

$\omega_0 = resonant\ frequency = 2\pi * 50$rad/s or $2\pi * 100$rad/s (As resonant controller will work only on either neutral current of 50Hz or 100Hz AC component of d and q-axis current during 3-phase unbalance energy exchange condition)

$\omega_C = bandwidth\ around\ \omega_0$. Ideally, preferred bandwidth should be zero. However, in reality maximum frequency deviation of the grid is 5Hz. In order to be consistent with this standard, $\omega_C = 2\pi * 5$rad/s has been considered.

After checking the Bode plots of the d axis PI current controllers and resonant controller separately, as shown in Fig.3.16, $K = 0.2$ has been considered. So that resonant current controllers will have small gain only at 50Hz and 100Hz for neutral current and d, q-axis currents respectively as explained before.

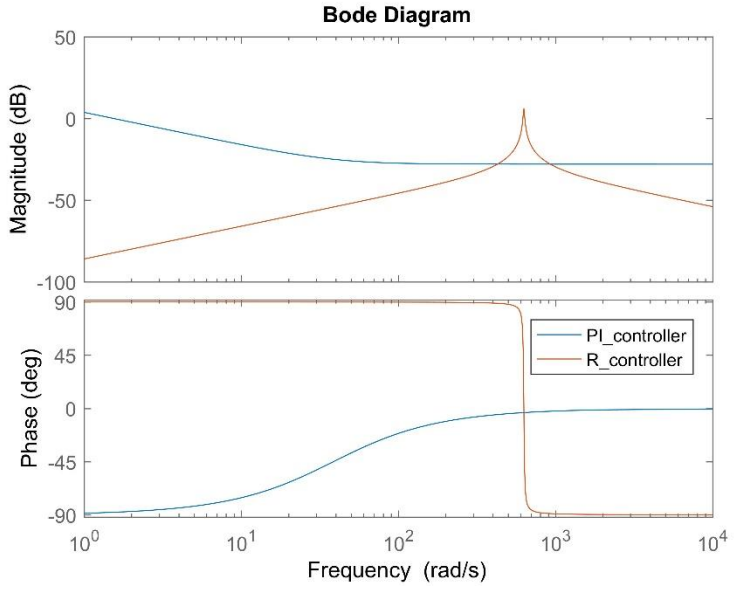

Fig.3.16 Bode diagram of the d-axis PI and R current controllers

Thus, the transfer function of resonant controller for controlling neutral current is expressed as $\frac{2s}{s^2+10s+(2\pi*50)^2}$ whereas it will be $\frac{2s}{s^2+10s+(2\pi*100)^2}$ for d and q-axis resonant current controllers.

Considering all these three modulating signals, coming out of current controllers, are generated in dq0 reference frame. They are transformed to abc- reference frame with inverse Park transform, thanks to Equ. 57.

3.4.2 Design of neutral point voltage controller

As discussed in Chapter 2, 150Hz current component is flowing at the middle point of the DC-bus of NPC due to its configuration. This creates voltage difference between two DC-bus capacitors of NPC. This fluctuation of neutral point voltage should be mitigated as it can create problems such as over-voltage across the switching devices, output voltage distortions or Common Mode Voltage (CMV) issues etc. [94].

In order to control that difference, voltage controller is essential for the converter. In order to minimize the voltage oscillations at the middle point of the DC-bus, zero potential difference (ΔV) between DC-bus upper and lower capacitor voltages($v_{c1} and\ v_{c2}$), should pass through a proportional controller. The gain of the proportional controller has been set to a small value, 0.001, so that the frequency response of the voltage controller loop will not overlap with the frequency response of the 50Hz resonant controller, used for neutral current control.

Homopolar current component has also an effect on this DC-bus voltage oscillation. For this reason, homopolar current controller and the DC-bus voltage controller outputs are added together in case of 3-leg NPC to generate the SPWM signal for the third leg as shown in Fig.3.17. But in case of 4-leg NPC, they are decoupled and the homopolar current controller output is used to control the third leg whereas the voltage controller output is responsible to control the fourth leg of the 4-leg NPC as shown in Fig.3.7.

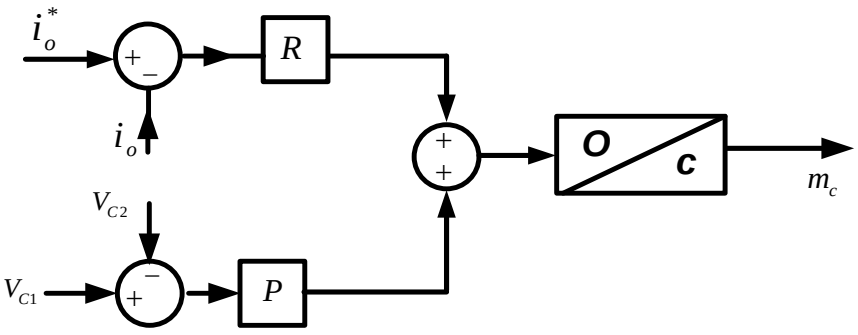

Fig.3.17 Coupling of homopolar current controller and the DC-bus voltage controller in 3-leg NPC

As observed in this section that there is a difference in controlling the DC-bus middle point voltage oscillation. In the following section, we will compare between 3-leg and 4-leg NPC converter in terms of size of the passive elements so that we can justify the necessity of 4-leg NPC converter as a bidirectional AC/DC converter in the onboard EV battery charger that can support unbalance network conditions.

3.5 Comparison between 3-phase 3-legs 4-wires and 3-phase 4-legs converters in different network conditions

In chapter 2, comparison between 3ph 4-wire 2-level and 3-level VSC has been done in terms of volume and weight. It was observed that,

- The value of AC-side inductor is half in 3-level VSC compared to that of 2-level VSC.
- In different unbalance network conditions, higher values of DC-bus capacitors are required in 2-level VSC compared to NPC, in order to limit Δv_C within a range.

Thus, it was concluded that 3-level VSC could reduce the overall volume and weight of the onboard EV bidirectional charger in unbalance network conditions. In this section we will compare between 3-level 3-leg and 4-leg VSC that can be more suitable for embedded battery charger.

There will be no change in the ratings of AC-side inductors. However, it is observed that the higher ratings of DC-bus capacitors are required in 3-leg NPC compared to that of 4-leg NPC. Mathcad model has been developed considering the equations in Sec. 2.2.3 and Sec. 2.4.3.2. Based on the Mathcad model, *Table 3* has been prepared to compare between Δv_{C3leg} andΔv_{C4leg}in different power exchange condition between three phases with same capacitor, whereas, *Table 4* has been prepared to compare between Δv_{C3leg} andΔv_{C4leg}in diffrent power exchange condition between three phases with different capacitors that can assure$\Delta v_{C4leg} = 5\%\ of\ V_{DC}$.

$C\ (\mu F)$	$P_1(kW)$	$P_2(kW)$	$P_3(kW)$	$Q_1(kVar)$	$Q_2(kVar)$	$Q_3(kVar)$	$\Delta v_{C3leg}(V)$	$\Delta v_{C4leg}(V)$
245	**7.36**	**0**	**0**	**0**	**0**	**0**	**177.4**	**119.8**
245	**7.36**	**3.68**	**3.68**	**0**	**0**	**0**	**94.62**	**59.9**
245	**7.36**	**0**	**0**	**0**	**-3.68**	**-3.68**	**212.5**	**133.7**
245	**2.3**	**-1.16**	**-1.16**	**0**	**-2.01**	**2.01**	**62**	**39.16**

Table 3: Comparison of DC-bus voltage oscillations between 3-leg and 4-leg NPC in different power exchange conditions with same capacitor

$C\ (\mu F)$	$P_1(kW)$	$P_2(kW)$	$P_3(kW)$	$Q_1(kVar)$	$Q_2(kVar)$	$Q_3(kVar)$	$\Delta v_{C3leg}(V)$	$\Delta v_{C4leg}(V)$
733	**7.36**	**0**	**0**	**0**	**0**	**0**	**44.9**	**40**
365	**7.36**	**3.68**	**3.68**	**0**	**0**	**0**	**87.48**	**40**
820	**7.36**	**0**	**0**	**0**	**-3.68**	**-3.68**	**44.8**	**40**
238	**2.3**	**-1.16**	**-1.16**	**0**	**-2.01**	**2.01**	**63.35**	**40**

Table 4: Comparison of DC-bus voltage oscillations between 3-leg and 4-leg NPC in different power exchange conditions with different capacitors

From both *Table 3* and *Table 4*, it is observed that always$\Delta v_{C3leg} \geq \Delta v_{C4leg}$, for same capacitor rating and network conditions. In these different network conditions, $P_1 = 2.3kW, P_2 = P_3 = -1.16kW, Q_1 = 0kvar, Q_2 = -2.01kvar\ and\ Q_2 = 2.01kvar$ is a constraining operating points as in this operating point, the r.m.s current flowing through the neutral wire will be 32A. This is our maximum allowed r.m.s current which can flow in one phase. Thus, we can conclude that the DC-bus capacitors of higher ratings are required in 3-leg NPC compared to 4-leg NPC in similar network conditions for getting$\Delta \boldsymbol{v_C}$ within our allowed limit. Thanks to all of these tests and observations, we can conclude that the 4-leg NPC is the best AC/DC bidirectional structure in terms of volume that can be integrated to the onboard bidirectional EV battery charger which can inject required active and reactive powers to the grid.

In order to validate this overall control strategy, closed loop control of 4-leg NPC converter has been performed in Matlab/Simulink. After that, Hardware-in-the-Loop (HIL) simulation has been performed with the same control strategy. Overview and requirement of HIL simulation has been described in Sec. 3.6. Expected results have been obtained for both in Matlab and HIL simulation and these results are shown in Sec. 3.7.

3.6 Hardware-in-the-Loop simulation

Thorough multiple tests are required to verify and validate the design and control strategy of a power electronic converter. Matlab simulation is a concept where both the control and power circuits of the converter have been designed in computer for initial testing. HIL simulation is a technique that is used for testing the control strategy of the converter in real time, thanks to FPGA/DSP processor [95][96][97]. In this strategy, the power circuit of the converter is still virtual but the real gate pulses are coming out of a digital controller in order to operate a power electronic converter as shown in Fig.3.18. Through various digital and analog I/O terminals, the controller interacts between real control and virtual power circuits of the converter [98].

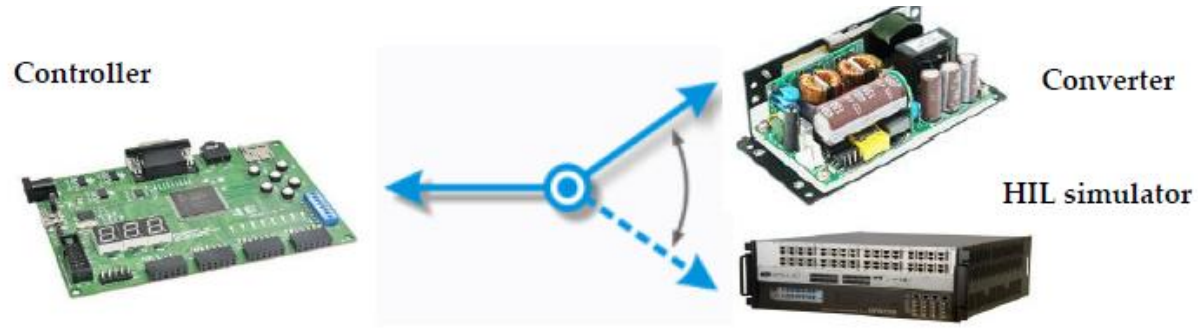

Fig.3.18 HIL strategy

HIL testing has following advantages [99]:

1. Save time: A lot of time is required in order to develop real prototype of a converter. Thanks to HIL simulator, developed control strategy of the converter can be checked rapidly and efficiently.

2. Save money: In case there is some unwanted issues in the developed control strategy of the converter then real converter prototypes can easily be destroyed. Thus, components of the prototypes need to be changed several times and that in turn will increase the cost of experimental validation. Thanks to HIL simulator, developed control strategy of the converter can be validated effectively.

3. Reduce risk and increase safety: With the help of HIL simulator, control algorithm of a complex system can be tested without any risk. Thus, engineers can perform various experiments without any worries.

In G2ELab, Opal-RT 5700 real time simulator has been used for emulating the power converter, which is controlled by LabVIEW driven Zynq processor (CPU+FPGA). The whole setup has been shown in Fig.3.19.

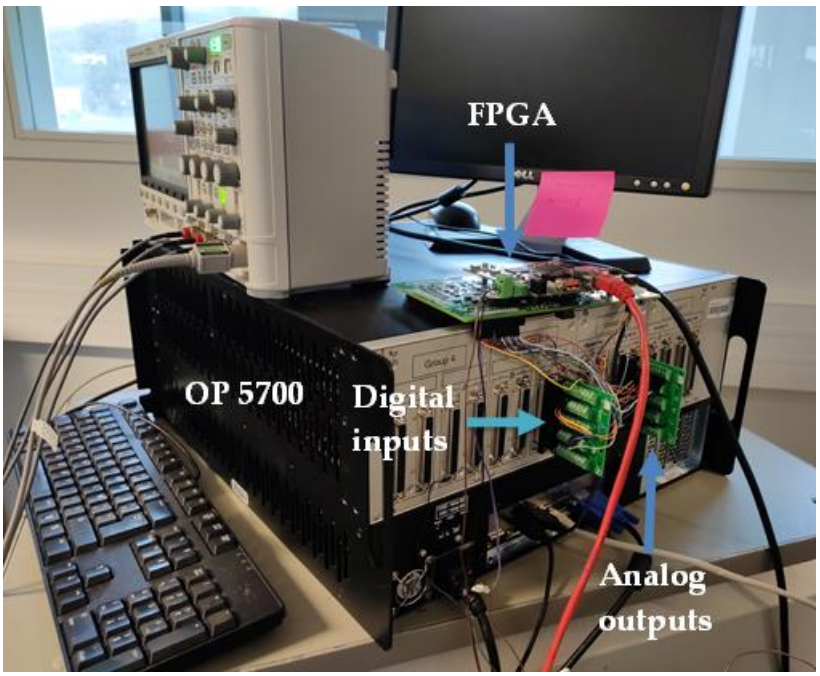

Fig.3.19 Opal-RT real time simulator for HIL simulation of power electronic converter

Code, required for developing the control strategy of the converter, has been splitted separately between CPU and FPGA due to less space in FPGA. I/O terminals, Park and inverse Park transformation, SPWM strategy, reference currents generation from active and reactive power references have been coded in FPGA whereas controllers have been designed in CPU.

3.7 Results for validating the closed loop model of NPC converter in different operating conditions

In this section, 4-leg NPC converter has been tested both in Matlab/Simulink and HIL in different test conditions and relevant results have been shown. The goal of these tests is to validate the developed control strategy of the 4-leg NPC converter in following operating conditions.

Condition a: Single phase operation between a-phase and neutral.
Active and reactive power for a-phase is considered as $P_a = 7kW$ and $Q_a = 0kVAr$ respectively whereas all other active and reactive powers in the remaining phases are set at zero.

Condition b: Three phase operation

- For, $0 \leq t \leq 1s.$, NPC converter is operated in 3-ph balance energy exchange condition has been considered with:

Reference active powers: $P_a = P_b = P_c = 7kW$
Reference reactive powers: $Q_a = Q_b = Q_c = 0kVAr$

- For, $t > 1s.$, unbalance energy exchange condition (one of the worse situations as discussed in Sec.3.3) has been considered with:

Reference active powers: $P_a = 2.3kW \;\; P_b = -1.16kW \;\; P_c = -1.16kW$
Reference reactive powers: $Q_a = 0kVAr \;\; Q_b = -2.01kVAr \;\; Q_c = 2.01kVAr$

- Another three phase unbalance power exchange condition, which is in between 3-phase balance condition and the condition with 32A (r.m.s) neutral current.

Reference active powers: $P_a = 3kW \quad P_b = 4kW \quad P_c = 2kW$
Reference reactive powers: $Q_a = Q_b = Q_c = 0kVAr$

In all these test conditions, other common parameters are considered as:
DC-bus voltage (V_{DC}) $= 800V$ (assuming DC-bus is perfectly controlled by the source)
DC-bus capacitors (C_1 & C_2) $= 5mF$ and line inductance $L = 5mH$
Phase voltage of the AC-grid (v_{ac}) $= 230V(rms)$

For all these test conditions,

- Reference and measured phase currents have been shown for validating the current control loops.

- DC-bus upper and lower capacitor voltages and their difference have been shown for validating the capacitive middle point voltage control loop.

Thanks to all of these results, we can understand the operational behavior of the AC/DC converter and justify its effectiveness both in single phase and 3-phase balance/unbalance operation.

a. Results in Matlab/Simulink for single-phase operation (between a-phase and neutral) of the converter:

Fig.3.21 and Fig.3.21 represent the a-phase reference and measured currents and DC-bus capacitor voltages and their difference in Matlab platform respectively for single phase operation of the NPC converter.

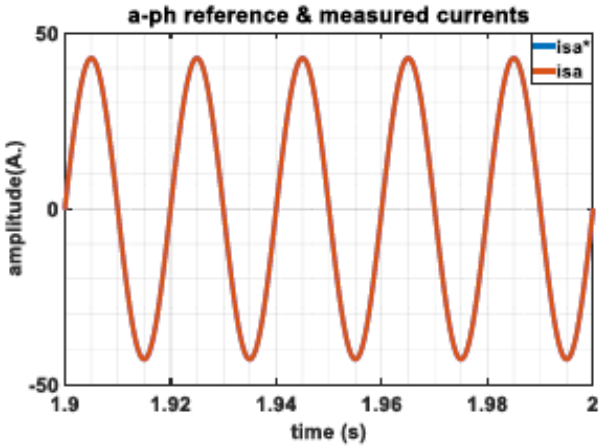

Fig.3.20 a-phase reference and measured currents during single phase operation in Matlab/Simulink platform

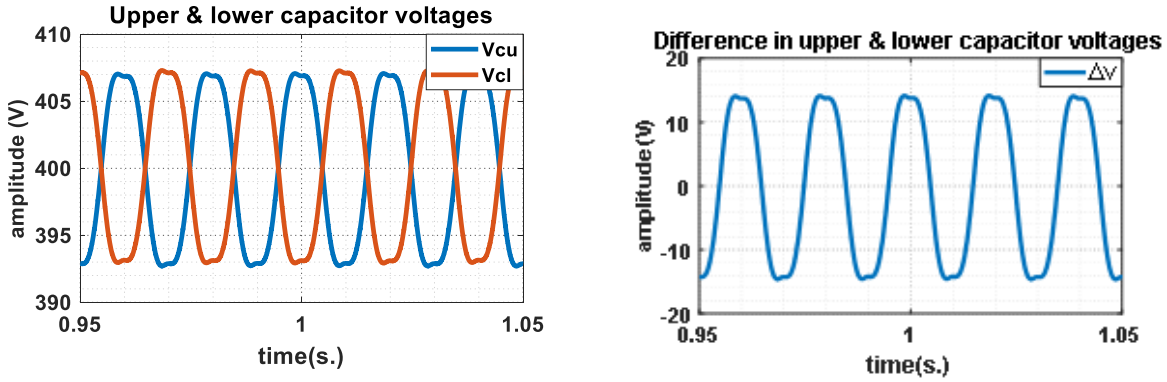

(a) *(b)*

Fig.3.21 (a) Upper and lower capacitor voltages of NPC DC-bus (b) Difference between upper and lower capacitor voltages of NPC DC-bus during single phase operation in Matlab/Simulink platform

From Fig.3.20, it is observed that a-phase reference and measured currents overlap with each other with expectedI_{am} = 43A. From Fig.3.21, it is observed that both the upper and lower capacitor voltages of DC-bus are varying within the limit keeping mean value of 400V. The

voltage difference between these two DC-bus capacitor voltages is around 29V($< 5\%$ of V_{DC}). Thus, it can be concluded that both the current control loops and voltage control loop of the NPC converter are working fine during single phase operation.

In order to show the effectiveness of the voltage loop controller, simulation has been done for single phase test condition without the voltage loop controller and result has been shown in Fig.3.22. It is observed that capacitor voltages are oscillating between 372-428V which is beyond threshold limit of ΔV.

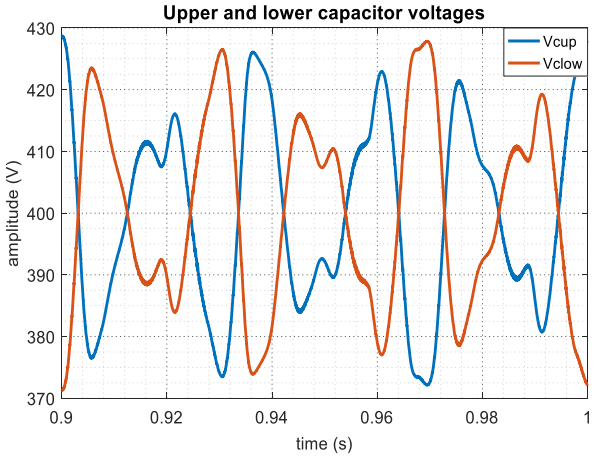

Fig.3.22 Upper and lower capacitor voltages of NPC DC-bus during single phase operation without voltage controller in Matlab/Simulink platform

b. Results in both Matlab/Simulink and HIL platform for 3-phase operation of the converter:

<u>Condition 1:</u>

As stated earlier, Matlab simulation of the 4-leg NPC converter has been done for 3-phase balance energy exchange condition during $0 \leq t \leq 1s$ whereas it was simulated for unbalance energy exchange condition (one of the worst situations as discussed in Sec.3.3) during $t > 1s$.

For ensuring the under modulation operation of the NPC converter, Matlab simulation result of modulating signals of 4-leg NPC converter in closed loop control strategy, is shown in Fig.3.23. During$0 \leq t \leq 1s$., modulating signals of a, b and c phase legs of NPC converter are within ±0.8. Modulating signal for neutral phase of the NPC converter is zero, due to zero neutral current as the converter is operating in balanced condition. At $t > 1s$.,unbalance energy exchange condition between phases has been introduced and because of that $m_n$starts varying sinusoidally. It shows the operation of the 4^{th}leg of 4-leg NPC converter to control the neutral current, depending on unbalance energy exchange condition between 3-phases.

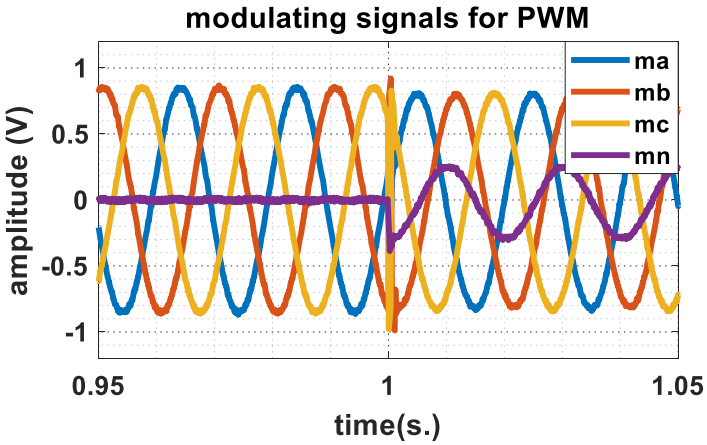

Fig.3.23 Modulating signals used for generation of switching pulses of four legs of NPC converter in Matlab/Simulink platform [Test condition: $P_a = P_b = P_c = 7kW$ and $Q_a = Q_b = Q_c = 0kVAr$ for $0 \leq t \leq 1s$ and $P_a = 2.3\ kW, P_b = -1.16kW, P_c = -1.16kW$ and $Q_a = 0kVAr, Q_b = -2.01kVAr, Q_c = 2.01kVAr$ at $t \geq 1s$.*]*

Fig.3.26, Fig.3.25 and Fig.3.26 represent the a-phase and neutral phase reference and measured currents, DC-bus capacitor voltages and their difference respectively in Matlab platform, both for 3-phase balanced and unbalanced energy exchange conditions.

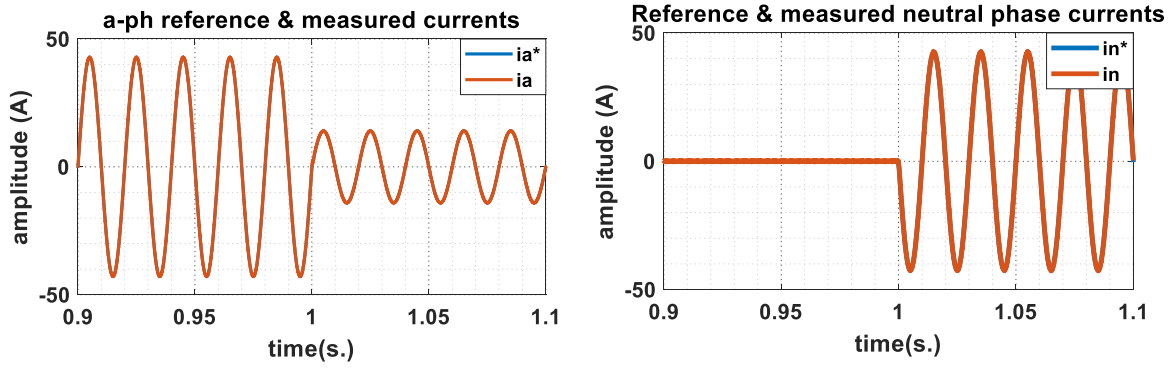

(a) *(b)*

Fig.3.24 (a) a-phase reference and measured currents (b) neutral-phase reference and measured currents in Matlab/Simulink platform [Test condition: $P_a = P_b = P_c = 7kW$ and $Q_a = Q_b = Q_c = 0kVAr$ for $0 \leq t \leq 1s$ and $P_a = 2.3\ kW, P_b = -1.16kW, P_c = -1.16kW$ and $Q_a = 0kVAr, Q_b = -2.01kVAr, Q_c = 2.01kVAr$ at $t > 1s$.*]*

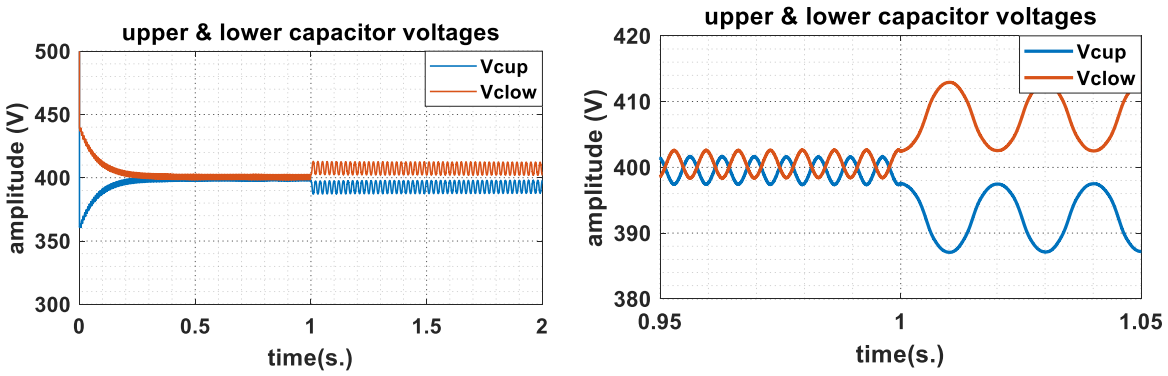

(a) *(b)*

Fig.3.25 DC-bus upper and lower capacitor voltages (a)normal scale (b)zoomed version in Matlab/Simulink platform [Test condition: $P_a = P_b = P_c = 7kW$ and $Q_a = Q_b = Q_c = 0kVAr$ for $0 \leq t \leq 1s$ and $P_a = 2.3\ kW, P_b = -1.16kW, P_c = -1.16kW$ and $Q_a = 0kVAr, Q_b = -2.01kVAr, Q_c = 2.01kVAr$ at $t > 1s$.*]*

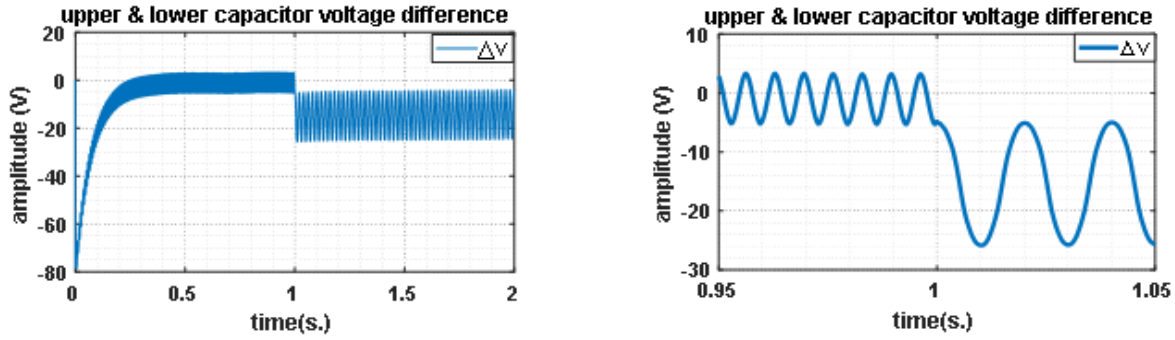

(a) *(b)*

Fig.3.26 Voltage difference of DC-bus upper and lower capacitor voltages (a)normal scale (b)zoomed version in Matlab/Simulink platform [Test condition: $P_a = P_b = P_c = 7kW$ and $Q_a = Q_b = Q_c = 0kVAr$ for $0 \leq t \leq 1s$ and $P_a = 2.3\ kW, P_b = -1.16kW, P_c = -1.16kW$ and $Q_a = 0kVAr, Q_b = -2.01kVAr, Q_c = 2.01kVAr$ at $t \geq 1s$.*]*

From Fig.3.24, it is observed that a-phase and neutral phase reference and measured currents overlap with each other respectively for both 3-phase balance and unbalance situations. Similar waveforms have been observed for both b and c phase. During$0 \leq t \leq 1s$., both i_n^* and i_n are of zero magnitude while at $t > 1s$., both magnitudes are changed to 3-times of other phase current magnitudes.

Fig.3.25 and Fig.3.26 represent the DC-bus capacitor voltages and their difference respectively. During$0 \leq t \leq 1s$., both the upper and lower capacitor voltages of NPC DC-bus are varying within the limit, keeping mean value of 400V. However, the voltage oscillation is increased at $t = 1s$., but their difference is still around 22V, which is less than the our threshold limit (5% of V_{DC}). These results validate the goal of our tests which is to check the global control strategy of 4-leg NPC converter during 3-phase operation for both balanced and unbalance energy transfer conditions in Matlab/Simulink platform.

Same tests have been performed in Matlab/Simulink platform without the voltage controller and the results have been shown in Fig.3.27. It is observed that for 3-phase balance operating condition, DC- bus capacitor voltages are similar to the result with voltage controller. However, in case of unbalance condition, DC-bus voltage oscillations are very large. In fact, modulation signals exceed the under modulation limit of ± 1. It happened because when the capacitor voltages are at minimum values, V_{DC} is not sufficient for under modulation operation zone due to their relation mentioned in Equ. 29. Only solution to overcome this situation is either to increase the DC-bus capacitor ratings or to increase V_{DC}.

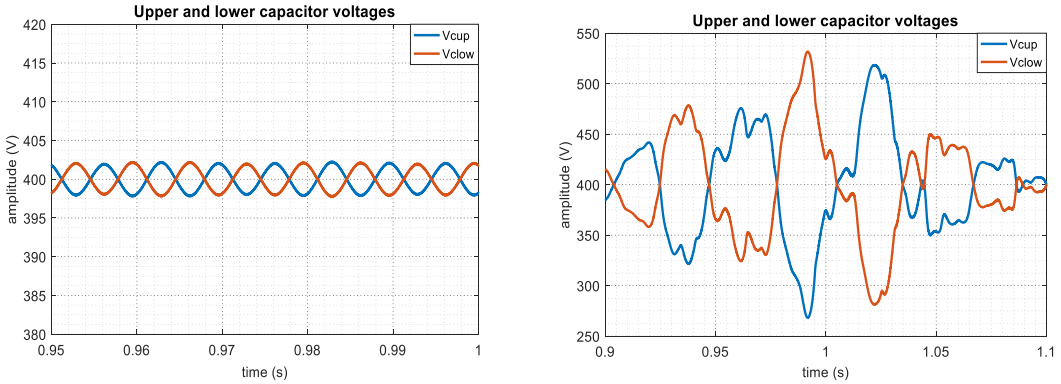

(a) *(b)*

Fig.3.27 Voltage difference of DC-bus upper and lower capacitor voltages in Matlab/Simulink platform without voltage controller (a) $P_a = P_b = P_c = 7kW$ and $Q_a = Q_b = Q_c = 0kVAr$ *(b)* $P_a = 2.3\ kW, P_b = -1.16kW, P_c = -1.16kW$ and $Q_a = 0kVAr, Q_b = -2.01kVAr, Q_c = 2.01kVAr$

As stated earlier, HIL simulation have also been performed and results have been shown to validate the global control strategy of 4-leg NPC converter during 3-phase operation for both balanced and unbalance power transfer condition in three phases in real-time platform. However, the magnitude of all parameters are scaled down in order to represent them by I/O terminals of FPGA.

Supply phase voltages and supply phase currents, obtained from the HIL simulation platform, have been shown in Fig.3.28 while 4-leg NPC converter is working under balanced operating condition of 7kW active power and zero reactive power in each phase. Thanks to our developed closed loop control strategy, it is observed that

- The phase voltages and the corresponding phase currents are in phase which ensures the near unity power factor operation of the NPC converter. This is one of the fundamental grid codes to check for any grid connected converter.
- Scaled down values of the three phase currents are in accordance with the calculated values of $I_{xm} = 43A\ (x \in a, b\ and\ c)$.

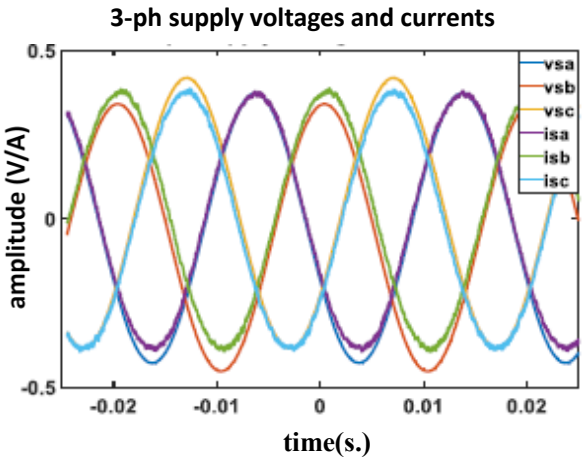

Fig.3.28 3-ph supply voltages and currents in HIL simulation [Test condition: $P_a = P_b = P_c = 7kW$ and $Q_a = Q_b = Q_c = 0kVAr$*]*

Fig.3.29 represents the voltage difference of the DC-bus upper and lower capacitors of the NPC converter in HIL platform during 3-phase balance and one of the worse unbalance energy exchange conditions respectively. Differences in DC-bus capacitor voltages are observed around 8V and 22V which are as equal as Matlab/Simulink simulation results, shown in Fig.3.26. Comparisons of these results with Matlab/Simulink platform ensure the correct implementation of closed loop model of 4-leg NPC in HIL platform.

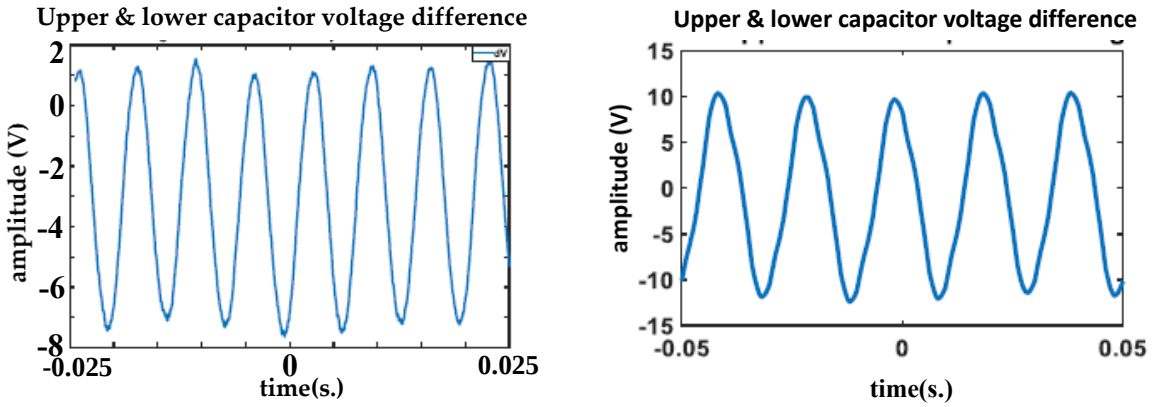

(a) *(b)*

Fig.3.29 Voltage difference of DC-bus upper and lower capacitor voltages in HIL simulation [Test condition: (a) $P_a = P_b = P_c = 7kW$ and $Q_a = Q_b = Q_c = 0kVAr$ *(b)* $P_a = 2.3\ kW, P_b = -1.16kW, P_c = -1.16kW$ and $Q_a = 0kVAr, Q_b = -2.01kVAr, Q_c = 2.01kVAr$*]*

<u>Condition 2:</u>

As stated earlier, another transition between balanced 3-phase operation and condition with 32A (r.m.s) neutral current, has been simulated in Matlab/Simulink for double checking of the proposed control strategy of NPC converter during three-phase operation. In this case, HIL simulation results have not been shown, just to avoid repetition.

Similar to previous unbalance energy exchange condition between three phases, four results has been checked for verifying the proposed control strategy of the 4-leg NPC converter and they are:

- Modulating signals of all four phases ($m_a, m_b, m_c \; and \; m_n$) for checking the under modulation operating zone of the converter.
- Reference and measured currents of one phase and neutral for verifying the designed current controllers.
- DC-bus capacitor voltages and their difference in order to verify that the capacitive middle point voltage oscillation is within the limit, thanks to voltage control loop.

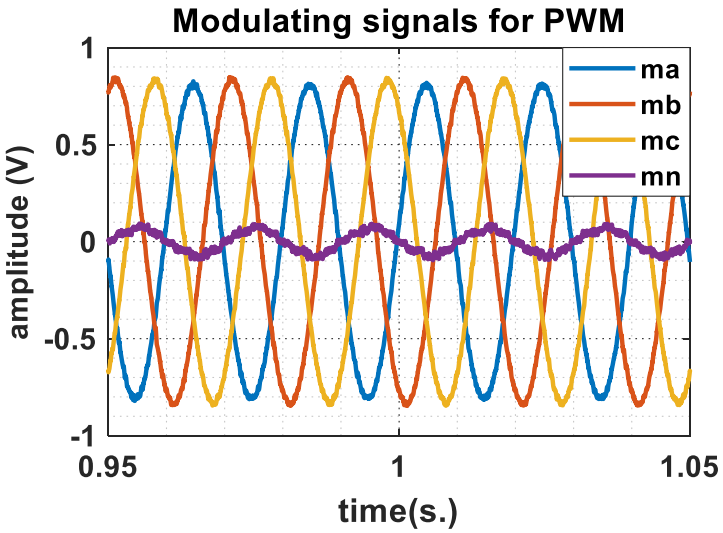

Fig.3.30 Modulating signals used for generation of switching pulses of four legs of NPC converter in Matlab/Simulink platform [Test condition: $P_a = 3kW \; P_b = 4kW \;\; P_c = 2kW$ and $Q_a = Q_b = Q_c = 0kVAr$*]*

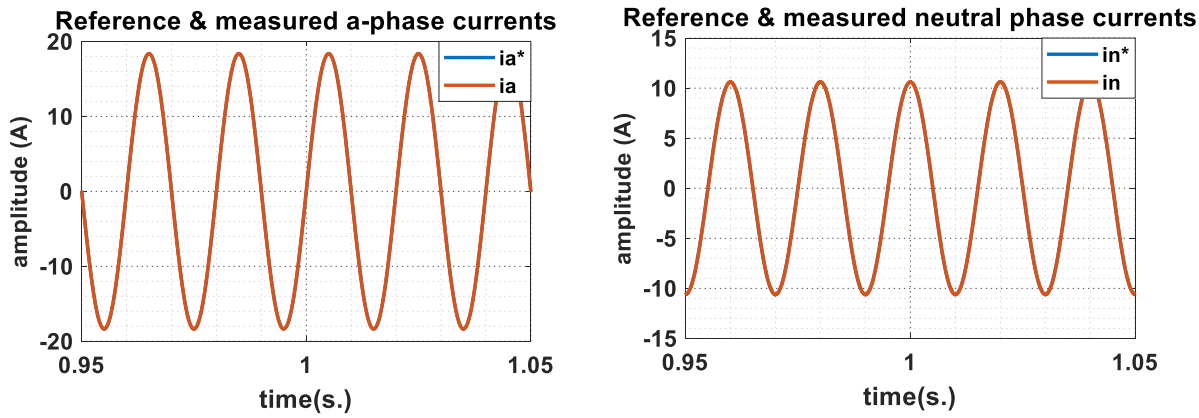

(a) *(b)*

Fig.3.31 (a) a-phase reference and measured currents (b) neutral-phase reference and measured currents in Matlab/Simulink platform [Test condition: $P_a = 3kW \; P_b = 4kW \;\; P_c = 2kW$ and $Q_a = Q_b = Q_c = 0kVAr$*]*

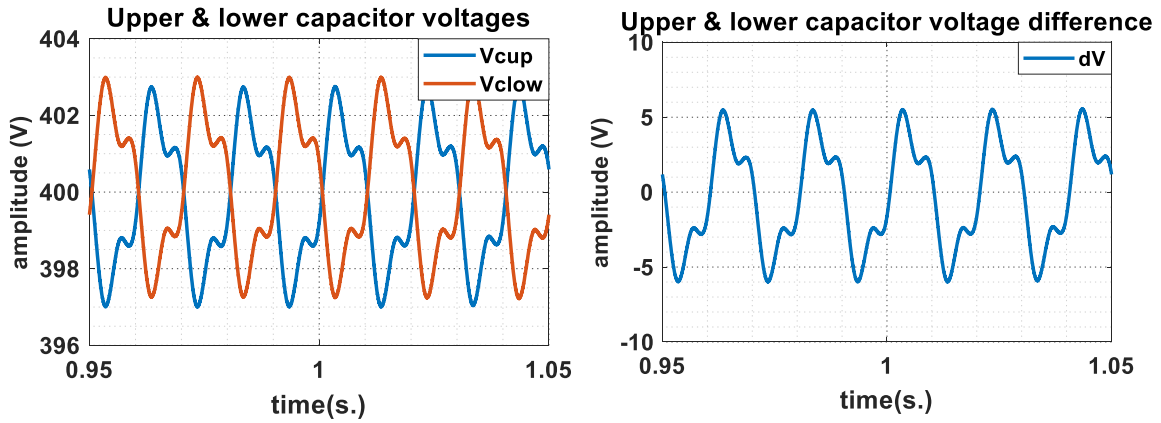

(a) *(b)*

Fig.3.32 (a) DC-bus upper and lower capacitor voltages (b) Voltage difference between two capacitors in Matlab/Simulink platform [Test condition: $P_a = 3kW\ P_b = 4kW\ \ P_c = 2kW$ and $Q_a = Q_b = Q_c = 0kVAr]$

From Fig.3.30, it is observed that all four modulating signals, required for PD-PWM strategy of 4-leg NPC, are varying sinusoidally with amplitudes lying between ±1. It ensures that the converter is working in normal modulation zone. Fig.3.31 and Fig.3.32 represent the a-phase and neutral reference and measured currents and DC-bus capacitor voltages and their difference respectively in Matlab/Simulink platform. According to numerical analysis, amplitude of $i_a^* = \frac{\sqrt{2}*S_a}{v_{sa}} = \frac{\sqrt{2}*3000}{230} = 18.45A$. From Fig.3.31, it is observed that both 'a' and neutral phase reference and measured currents overlap with each other during this condition. Similar results have been observed for both 'b' and 'c' phase due to proper function of current controllers. Fig.3.32 represents the voltage profiles of DC-bus upper and lower capacitor voltages and their difference. It is observed that the difference is ±5V, which is within the limit of 5% of V_{DC}. Thus, it can be concluded that the voltage controller of the of the 4-leg NPC is also working properly during this condition of unbalance energy exchange between three phases.

Same test has been performed in Matlab/Simulink platform without the voltage controller and the results have been shown in Fig.3.33. It is observed that the DC-bus capacitor voltage oscillations are increased significantly compared to result with voltage controller as shown in Fig.3.22.

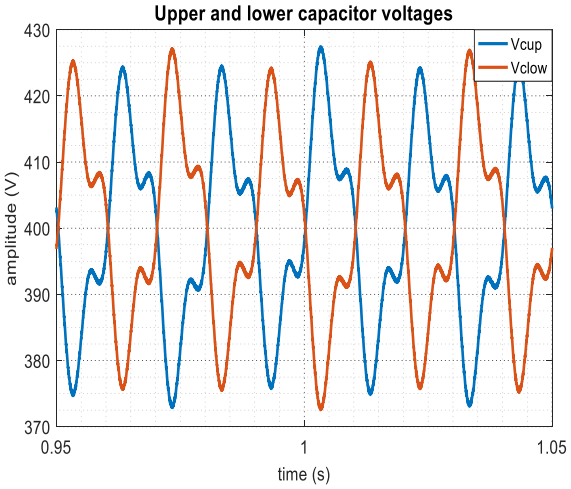

Fig.3.33 DC-bus upper and lower capacitor voltages in Matlab/Simulink platform at test condition: $P_a = 3kW\ P_b = 4kW\ \ P_c = 2kW$ *and* $Q_a = Q_b = Q_c = 0kVA$ *without voltage controller*

With all these results, obtained from Matlab/Simulink and real time HIL simulation, it can be concluded that the developed closed loop control strategy of the 4-leg NPC converter is working fine both for single phase and different conditions of three phase charging. However, DC voltage was supplied by battery of constant value of 800V during all these tests as AC/DC converter was tested individually. In the overall bidirectional EV battery charger, this battery will be removed and DC bus will be supplied by the output of the DC/DC converter.

3.8 Method to reduce the DC-bus voltage oscillation further

4-leg NPC converter can keep the DC-bus voltage oscillation within the limit for different operating conditions. Configuration, as shown in Fig.3.34, has been considered for reducing the DC-bus voltage oscillation further.

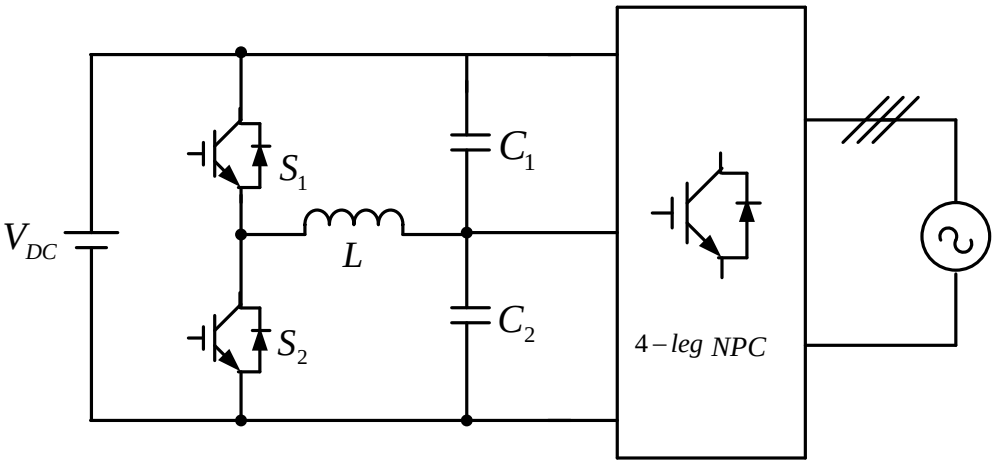

Fig.3.34 Configuration to compensate the DC-bus voltage oscillation further

With this configuration one additional leg, consisting of two IGBTs, has been added to the middle point of the DC-bus of 4-leg NPC converter through an inductor. This additional leg will act as an active filter and inject the opposite current to the middle point of the DC-bus, depending on the voltage difference between two DC-bus capacitors and this in turn will reduce the voltage oscillation further by current compensation.

3.8.1 Comparison of DC-bus middle point voltage oscillation between 4-leg NPC with an additional leg and 4-leg NPC

Matlab simulations have been done with the configuration of 4-leg NPC with an additional leg for comparing the results with 4-leg NPC. For the sake of comparison, parameters for simulation have been chosen same as that of 4-leg NPC, operating under 3-phase unbalance condition, mentioned in Sec. 3.7.

Voltages across DC-bus capacitors and their difference for both the above-mentioned conditions have been shown in Fig.3.35 and Fig.3.36.

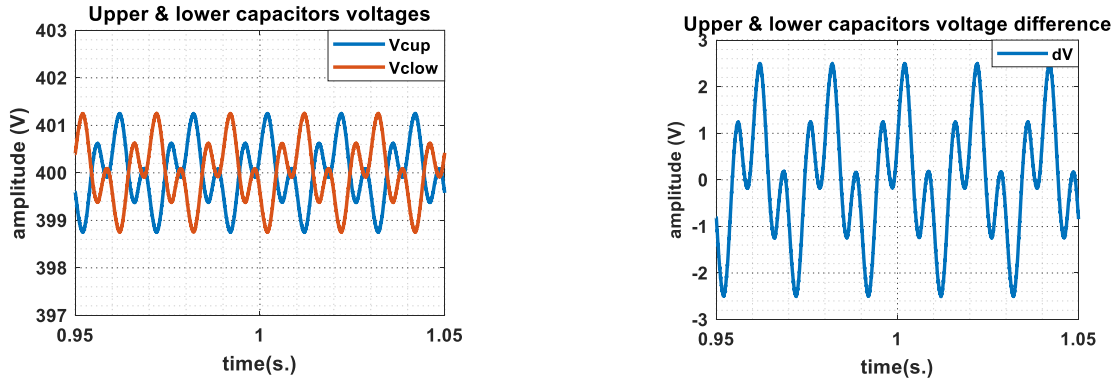

Fig.3.35 (a) DC-bus upper and lower capacitor voltages (b) Voltage difference between two capacitors in Matlab/Simulink platform [Test condition: $P_a = 3kW\ P_b = 4kW\ P_c = 2kW$ and $Q_a = Q_b = Q_c = 0kVAr$*]*

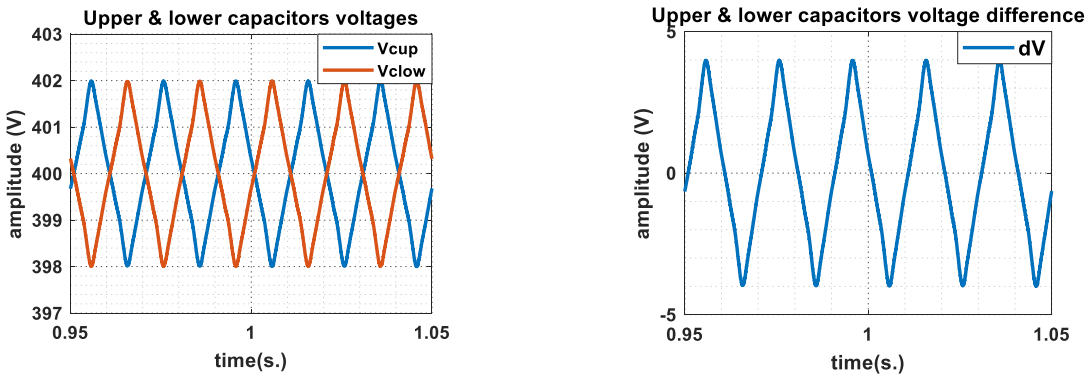

(a) *(b)*

Fig.3.36 (a) DC-bus upper and lower capacitor voltages (b) Voltage difference between two capacitors in Matlab/Simulink platform [Test condition: $P_a = 2.3kW\ P_b = -1.16kW\ P_c = -1.16kW$ *and* $Q_a = 0kVAr\quad Q_b = -2.01kVAr\quad Q_c = 2.01kVAr$*]*

It is observed that voltage variation, at the middle point of the DC-bus capacitors, has almost been nullified with the new configuration. Whereas, these oscillations were more for 4-leg NPC, operated under same conditions, as observed in Fig.3.25, Fig.3.26, and Fig.3.32.

Below *Table 5* compares the voltage variation with two configurations.

Active and reactive powers	ΔV with 4-leg NPC	ΔV with 4-leg NPC+5th leg
$P_a = 3kW\ P_b = 4kW\ P_c = 2kW \quad Q_a = Q_b = Q_c = 0\ kVAr$	±5V	±2.5V
$P_a = 2.3kW\ P_b = -1.16kW\ P_c = -1.16kW\ Q_a = 0kVAr\quad Q_b = -2.01kVAr\quad Q_c = 2.01kVAr$	±11V	±4V

Table 5: Comparison of voltage oscillation between 4-leg NPC and 4-leg NPC+5th leg

This new configuration is better in terms of reducing capacitive middle point voltage oscillation which in turn can help to reduce the size of the DC-bus capacitors further. However, additional inductor, additional leg with two IGBTs and their auxiliary circuits may increase the overall volume, weight and losses of the charger.

3.9 Conclusion

In this chapter, closed loop control strategy has been developed for 4-leg NPC converter, which will be used as bidirectional AC/DC part of EV battery charger. In addition, tuning of

both line current and capacitive middle point voltage controllers of the converter have also been done.

Thanks to offline Matlab/Simulink, developed closed loop control strategy of the 4-leg NPC converter has been validated in different operating conditions:

1. Single phase operation.
2. 3-phase operation during balanced energy exchange between three phases.
3. 3-phase operation during unbalanced energy exchange between three phases with two different situations.

   a. $P_a = 2.3\ kW, P_b = -1.16kW, P_c = -1.16kW$ and $Q_a = 0kVAr, Q_b = -2.01kVAr, Q_c = 2.01kVAr$ (one of the worst unbalance condition with 32A r.m.s neutral current)

   b. $P_a = 3kW\ P_b = 4kW\ \ P_c = 2kW$ and $Q_a = Q_b = Q_c = 0kVAr$

Real-time simulations have also be performed for above mentioned conditions of 2 and 3a in order to validate the developed control strategy of the 4-leg NPC converter which will be used as AC/DC conversion part of the bidirectional EV battery charger.

With the developed controlled strategy, the NPC converter can operate in four-quadrant mode as shown in Fig.3.37.

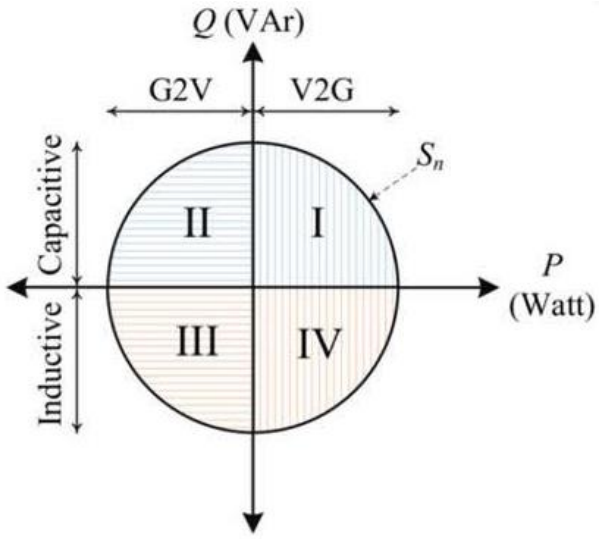

Fig.3.37 G2V and V2G operating point of EV bidirectional battery charger based on reference active and reactive power

Voltage oscillations (ΔV) of the DC-bus capacitors are 29V and 22V during single phase and one of the worst situations (32A r.m.s current in neutral phase) of three-phase operation respectively. Also, we have used an additional controller for the DC-bus middle point which does not remove the issue fully and can interact with the global control if the design is not done adequately. Though ΔV is within the limit but still we want to check the possibility of minimizing it more with the help of DC/DC converter.

As we want an insulated solution, DAB topology has been considered primarily as bidirectional DC/DC converter as shown in Fig.3.38.

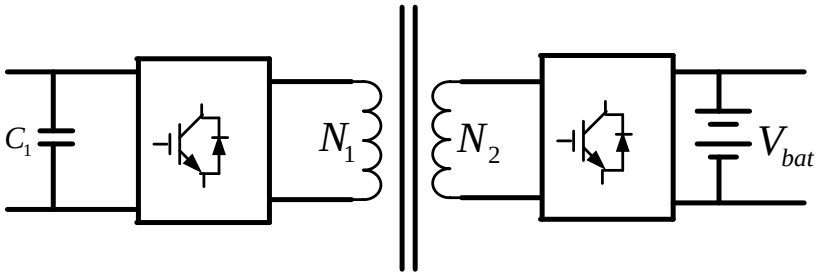

Fig.3.38 Configuration of DAB

However, in order to redistribute the same volume and weight of windings of the HF transformer, Triple Active Bridge (TAB) topology (shown in Fig.3.39), has been considered for bidirectional insulated DC/DC converter. The motivation behind the using of TAB is to feed the upper and lower capacitors of the DC-bus separately in order to limit the voltage fluctuations. Indeed, the active filter has proven some effectiveness, however if it is a corrective action in order to eliminate the issue. What we want to do is to control precisely the amount of power delivered on each half of The DC-bus, in order to cancel the voltage discrepancies and control the global DC-bus. Although, four extra semiconductor switches are required in the secondary side of TAB compared to DAB, but they will be half of the voltage rating compared to a single DAB.

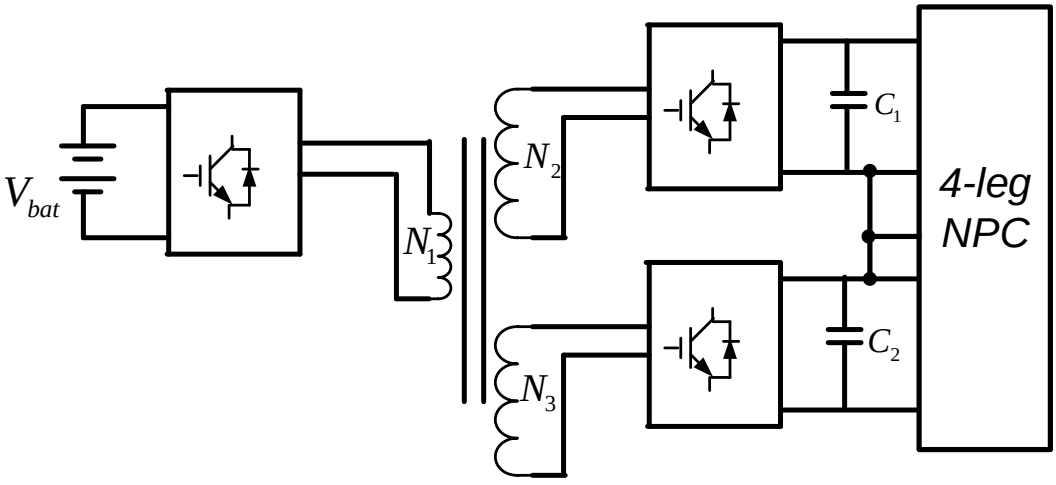

Fig.3.39 Configuration of TAB and its integration with 4-leg NPC

Closed loop control strategy of the TAB will be introduced in the next chapter. In order to validate the control strategy, Matlab/Simulation and HIL simulation results of the TAB will also be shown.

Chapter 4

INSULATED DC/DC CONVERTER

This chapter introduces both the configuration and the control strategy of insulated DC/DC converter that is required for regulating the battery current of the bidirectional EV battery charger with V2G application.

4. Introduction

As discussed in Chapter 1, for a grid connected EV, the power electronics part of the battery charger can include an isolated bidirectional DC/DC converter, which is essential for V2G application [100] [101]. However, non-isolated DC/DC converter is less heavy and simpler in structure than isolated one and can achieve better efficiency [102], but galvanic isolation in the converter structure can help in solving safety issues [103].

4.1 Configurations of the selected bidirectional DC/DC converter configuration and its power exchange

In the beginning, DAB configuration, as presented in Chapter 1, has been thought for bidirectional isolated DC/DC converter because of following advantages:
1. Lower transformer size due to HF commutation
2. Insulation in order to solve safety issues.

However, TAB configuration, which was first proposed in [104], has been chosen as bidirectional isolated DC/DC converter for further experiments. The interest to use a three-port transformer magnetically couples TAB [105] are followings:
1. Both half of the DC-bus voltages can be controlled individually.
2. This will not increase the overall size or losses of the charger significantly as the voltage stress across the semiconductor switches will be half compared to DAB and the secondary side of the transformer winding will just be splitted into two.

Fig.4.1 represents the configuration of TAB and its' connection with 4-leg NPC (only one leg is represented).

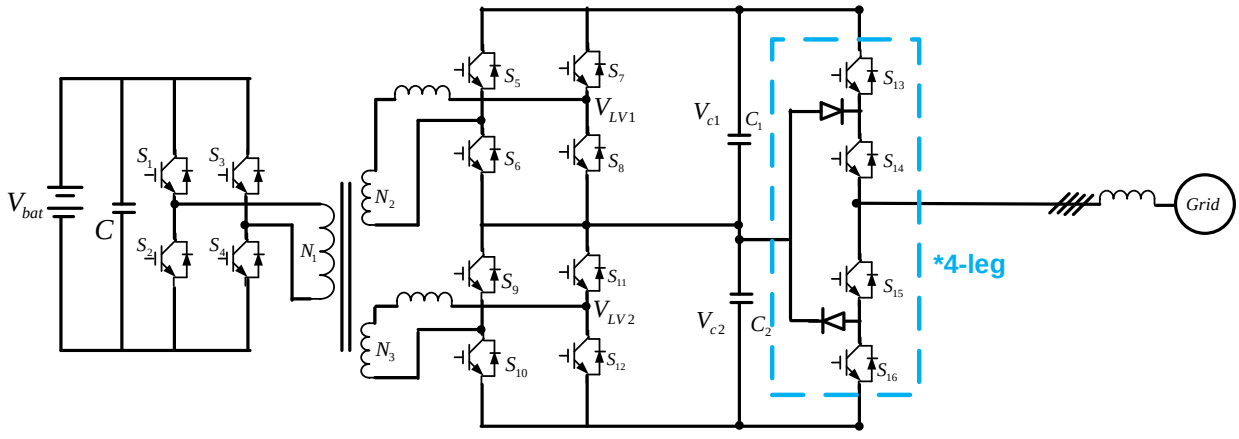

Fig.4.1 Configuration of TAB and its' connection with 4-leg NPC

For understanding the idea of the control strategy of the TAB, below Fig.4.2 represents the different power exchanges between the grid and the charger and also within the charge. Due to the unbalanced powers, a 100Hz harmonic component will be added on the DC-bus voltage. Due to the capacitive middle point connection, an additional fluctuation will appear and that will lead to a discrepancy between the upper and lower capacitor voltages. The frequency will be the classical 150Hz component due to the NPC operation along with a 50Hz component, appears due to the unbalance power exchange conditions, as discussed in Chapter 3. The goal of the TAB is to mitigate this two unbalances. Because of the TAB, the DC-bus voltage will be controlled, thanks to the battery power exchange (Yellow arrow) and the unbalances between the capacitor voltages will be controlled, thanks to the two output stages (Red dotted arrow).

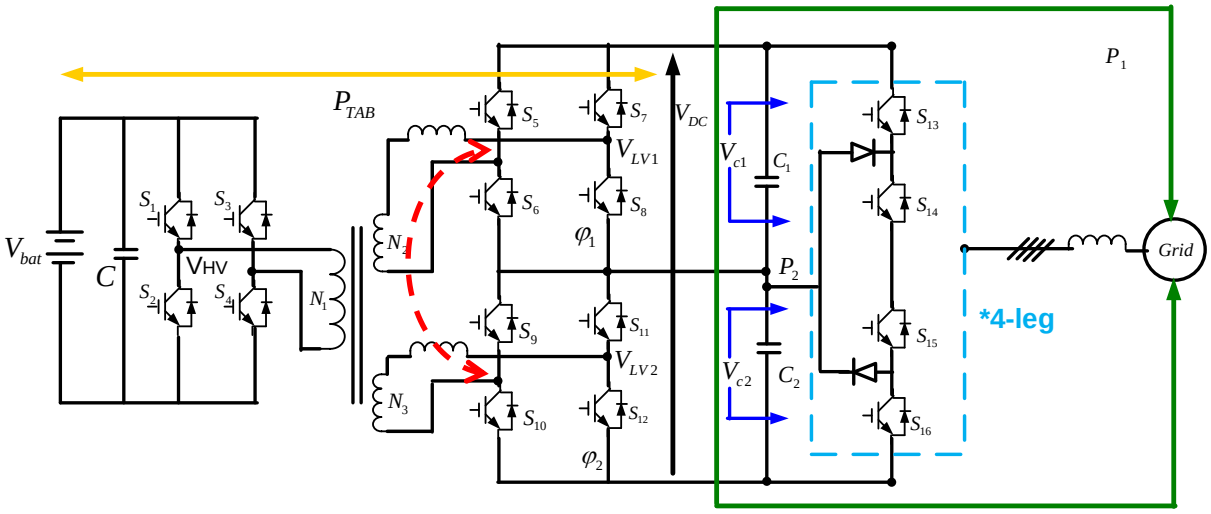

Fig.4.2 Integrated bidirectional EV battery charger and flow of powers within it

In case of TAB, the easy solution for transferring power between H-bridges is to generate the phase difference between them. Thus, we need to develop the control strategy in such a way that can generate phase shifts between three H-bridges and based on these phase shift angles bidirectional power transfer will be managed.

4.2 Control strategy for TAB

Control strategy of the TAB should ensure the control of two major parameters. They are:

- Constant DC voltage must be ensured to allow the inverter for operating the in a proper way, i.e., without overmodulation and associated current distortions.
- Voltage balancing between two DC-bus capacitors must also be ensured for limiting the value of ΔV within a limit and avoid the output current distortion also.

In order to control DC-bus voltage, two solutions are possible. First one is to control V_{C1} *and* V_{C2} individually and the second one (which has been chosen) is to control the DC-bus voltage and voltage unbalance separately. For controlling the DC-bus voltage, sum of the DC-bus capacitor voltages must be maintained at a constant value of 800V (V_{DC}^{*}) and on the other hand, their difference must be maintained at 0 for controlling the voltages across DC-bus capacitors.

As mentioned before, the power transfer in a DAB/TAB structure is linked to the phase shifts between inputs and outputs. V_{HV}, V_{LV1} *and* V_{LV2} represent the voltages across the H-bridge of the battery side, voltages across the upper and lower H-bridges of the DC-bus side of the TAB respectively. With our control strategy, the sum of V_{LV1} *and* V_{LV2}will generate phase shift angle φ^{*}that will responsible to maintain the DC-bus voltage at V_{DC}^{*} and whereas their difference will generate $d\varphi$ (phase shift of switching pulses between DC-bus side active bridges) for reducing ΔV further.

Considering V_{HV}as a reference, the vector diagram of the TAB is represented by Fig.4.3.

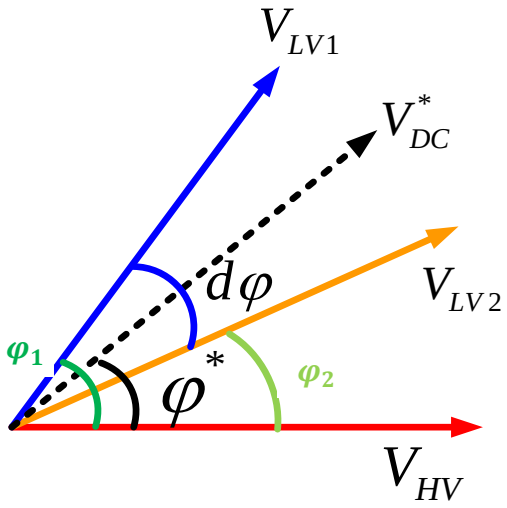

Fig.4.3 Vector diagram of the voltages in TAB

We are going to control the main power flow which is linked with φ^{*} and power unbalance between secondary sides of the TAB which is associated to $d\varphi$ thanks to the two phase shifts φ_1 and φ_2, representing the phase shifts between V_{HV} with V_{LV1} and V_{LV2} respectively.

From Fig.4.3, φ_1 and φ_2 can be written as:

$$\boldsymbol{\varphi_1 = \varphi^{*} + \frac{d\varphi}{2}} \quad \textbf{(80)}$$

$$\boldsymbol{\varphi_2 = \varphi^{*} - \frac{d\varphi}{2}} \quad \textbf{(81)}$$

With these generated two phase shift angles φ_1 and φ_2, we can control the bidirectional energy transfer of the TAB. Overall control strategy of TAB has been shown in Fig.4.4. Two control loops of energy sum and energy difference use PI controller for error correction and the

outputs of the PI controllers are used to generate the phase shifts between the gate pulses of the three H-bridges in the TAB.

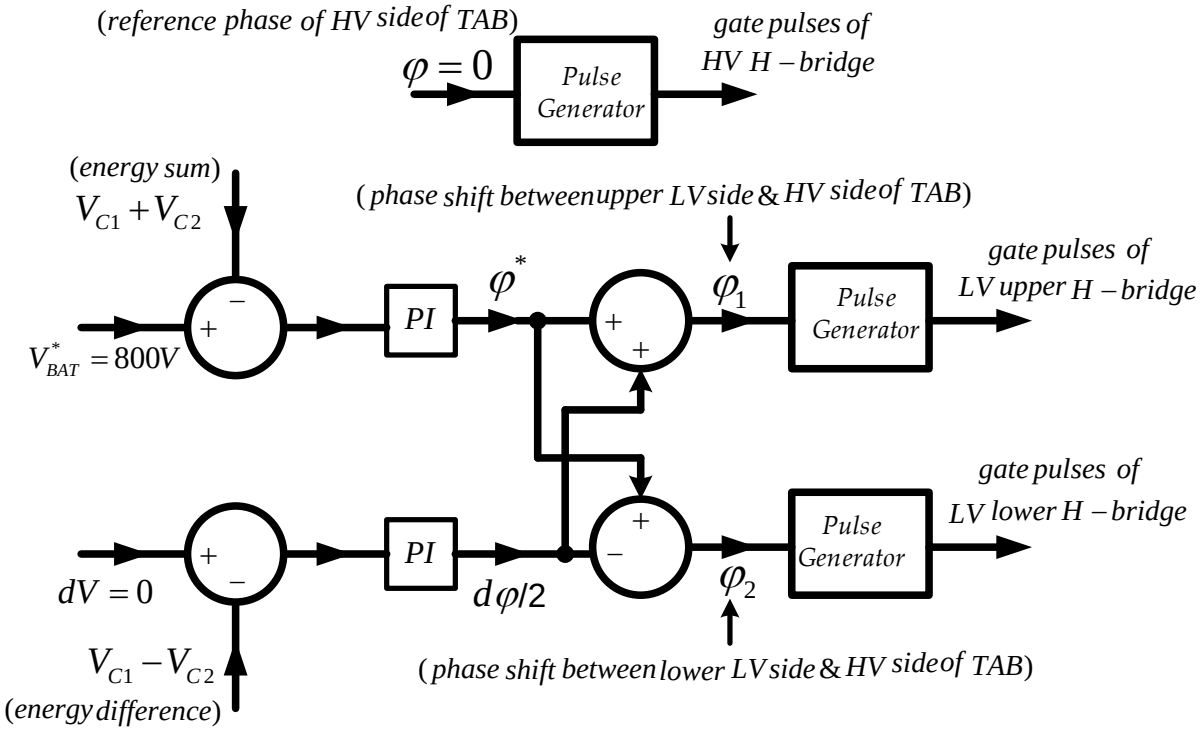

Fig.4.4 Control strategy for TAB

Fig.4.5 represents the pulse generator logic circuit. In our strategy, the duty cycle remains constant at 50%. It is a sawtooth signal used to compare with 0, φ_1 and φ_2. The output signals of the comparators are toggled at each falling edge by using monostable multivibrator. As a result, the frequency of the sawtooth signals is considered at 40 kHz (twice of the converter operating frequency).

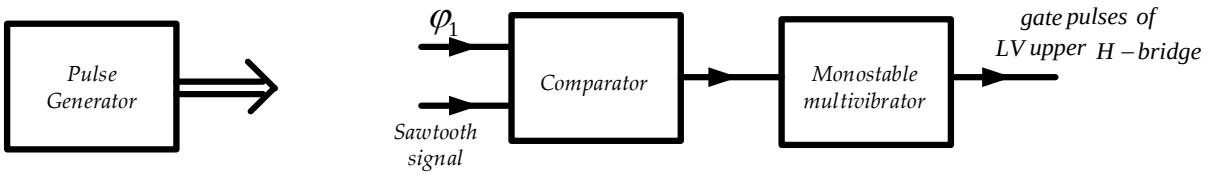

Fig.4.5 Logic circuit of the pulse generator used in the control strategy of the TAB

4.3 Implementation of the closed loop control strategy of the integrated charger by using Matlab/Simulink and its results

4.3.1 Design of PI controller

Two PI controllers, one associated to the energy sum and other associated to the energy difference, are used in the control strategy that includes DC-bus capacitors and equivalent resistance parallel to it. This section describes the tuning procedure of the parameters of the PI controllers.

Equivalent resistance, for one half of the DC-bus in 22kW battery charger, can be calculated as:

$$\boldsymbol{R_{eq} = \frac{(V_{DC}/2)^2}{P/2} = \frac{400^2}{11000} = 14.5\Omega} \quad \textbf{(82)}$$

Transfer function of the RC parallel circuit is $\frac{\boldsymbol{R}}{\boldsymbol{1+sRC}}$ **(83)**

Open loop transfer function of the system that includes PI controller with RC-circuit is:

$$\boldsymbol{G(s) = \frac{K_p(s+\frac{K_I}{K_p})}{s} * \frac{1}{C(s+\frac{1}{RC})}} \quad \textbf{(84)}$$

According to the Pole-Zero cancellation method, $G(s) = \frac{K_p}{sC}$

Closed loop transfer function of our system after Pole-Zero cancellation and with unity feedback gain will be $\boldsymbol{C(s) = \frac{1}{1+s\frac{C}{K_p}}}$ **(85)**

Closed loop transfer function of a system with unity feedback gain can be represented as: $\frac{\boldsymbol{1}}{\boldsymbol{1+s\tau}}$ **(86)**

Comparing Equ. 85 and 86,

$$\boldsymbol{\tau = \frac{C}{K_p}} \quad \textbf{(87)}$$

The cutoff frequencies of both the PI controllers are considered separately. 20Hz cutoff frequency is considered for the PI controller associated to energy sum as it is designed to control only the DC-component of V_{DC}. 1 kHz cutoff frequency is considered for the PI controller associated to the energy difference as we want to cancel the effect of both 50Hz and 150Hz components which induce voltage discrepancies between the upper and lower DC-bus capacitors.

Considering DC-bus capacitor is of 5mF, parameters of the PI-controller associated with energy sum

$K_p = 0.005 * 2 * \pi * 20 = 0.63$

From Pole-Zero cancellation method, $\frac{K_i}{K_p} = \frac{1}{RC}$ **(88)**

$Or, K_i = 8.69$

As mentioned earlier, that proper designing of the PI controller was not done due to our hypothesis to use 20Hz cut-off frequencies for both the PI controllers that are used in TAB. Considering the same calculations made in Equ. 87 and 88, parameters of the PI-controller associated with energy difference are $K_p = 31.4$ and $K_i = 433.1$.

After calculating the parameters of the PI controllers, Matlab simulations of the integrated charger have been done for different conditions and discussed in the following section. However, with this hypothesis, power transfer to the battery will be limited.

4.3.2 Associated results in Matlab/Simulink platform:

After understanding the theory and design of the closed loop control strategy of the TAB, Matlab/Simulink model has been developed for the integrated bidirectional EV battery charger which includes both grid-connected 4-leg NPC (for bidirectional AC/DC power transfer) and TAB (for bidirectional DC/DC power transfer).

Integrated charger has been simulated in closed loop for 3-phase balanced power transfer operating conditions ($P_a = P_b = P_c = 7kW \quad Q_a = Q_b = Q_c = 0kVAr$) for checking the phase shifts between the modulating signals. From Fig.4.6, it is observed that there are phase differences between these generated modulating signals and this in turn will create the phase differences between the gate pulses of three H-bridges.

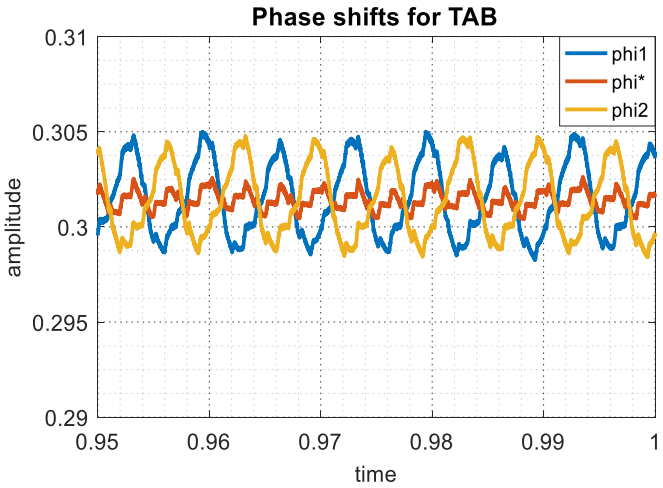

Fig.4.6 Modulating signals of the TAB

In order to justify the effectiveness of the proposed bidirectional EV battery charger, it has been tested for all single-phase, 3-phase balance and unbalance power exchange conditions. However, results have been shown only for single phase and 3-phase unbalance power exchange condition which are the main objectives of this thesis. The active and reactive powers for both these conditions are:

$\boldsymbol{A.P_a = 7kW\ \ P_b = P_c = 0kW \qquad Q_a = Q_b = Q_c = 0kVAr}$

$\boldsymbol{B.P_a = 2.3kW\ \ P_b = -1.16kW\ \ P_c = -1.16kW \qquad Q_a = 0kVAr\ \ Q_b = -2.01kVAr\ \ Q_c = 2.01kVAr}$

All other parameters are kept same for both the cases, which are:

Battery voltage (V_{bat}) = $800V$

DC-bus capacitors (C_1 & C_2) = $5mF$

Per phase voltage of the AC-grid= $230V(rms)$

Below mentioned relevant results have been shown:

1. DC-bus upper and lower capacitor voltages, their sum and their difference for verifying$\Delta V \leq 5\%\ of\ V_{bat}$.
2. Battery current and power in order to verify the control loop of the TAB.
3. Also, DC-bus voltage variations have been shown in 5mF capacitors without TAB control, for justifying the developed control strategy.

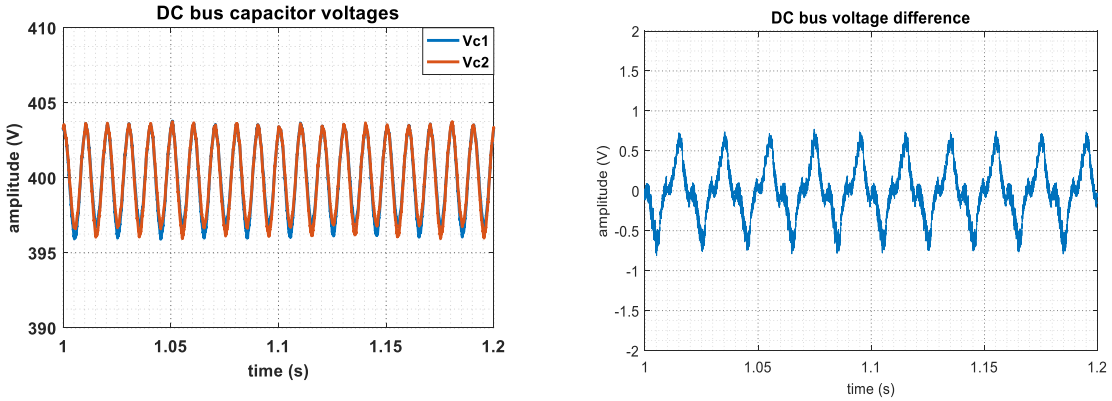

(a) *(b)*

Fig.4.7 a. Upper and lower capacitor voltages of the DC-bus b. Voltage difference between upper and lower capacitors of the DC-bus [Test condition: $P_a = 7kW\ \ P_b = P_c = 0\ kW$ and $Q_a = Q_b = Q_c = 0kVAr]$

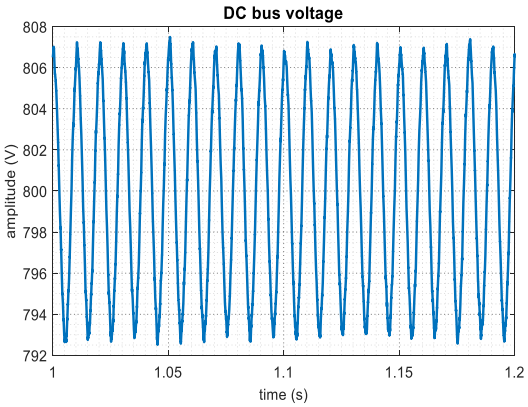

Fig.4.8 DC-bus voltage at test condition: $P_a = 7kW\ \ P_b = P_c = 0\ kW$ and $Q_a = Q_b = Q_c = 0kVAr$

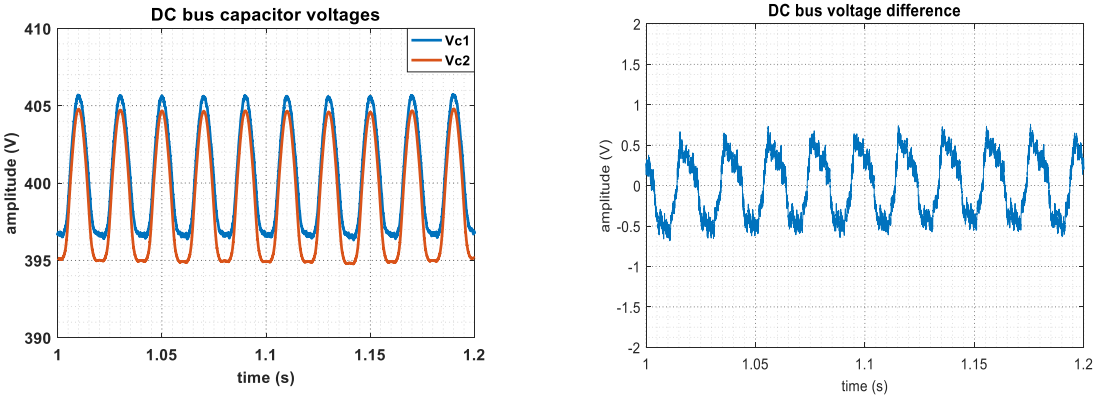

(a) (b)

Fig.4.9 a. Upper and lower capacitor voltages of the DC-bus b. Voltage difference between upper and lower capacitors of the DC-bus [Test condition: $P_a = 2.3\ kW, P_b = -1.16kW, P_c = -1.16kW$ and $Q_a = 0kVAr, Q_b = -2.01kVAr, Q_c = 2.01kVAr]$

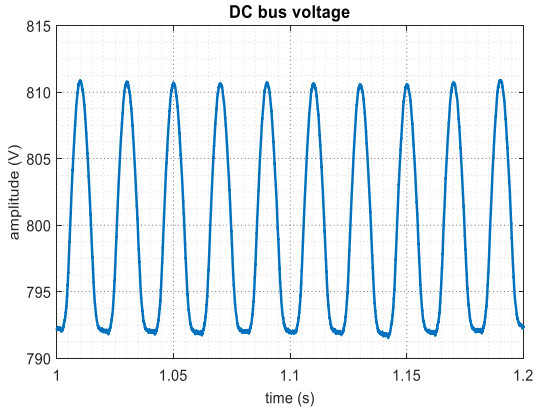

Fig.4.10 DC-bus voltage at test condition: $P_a = 2.3\ kW, P_b = -1.16kW, P_c = -1.16kW$ and $Q_a = 0kVAr, Q_b = -2.01kVAr, Q_c = 2.01kVAr]$

Fig.4.7 and Fig.4.9 represent the DC-bus capacitor voltages and their difference with closed loop control of the integrated bidirectional EV battery charger for both single phase and 3-phase unbalance power exchange conditions respectively. In both of the cases, variations of ΔV are almost nullified whereas they were 29V and 22V for single phase and 3-phase respectively as shown in Fig.3.21 and Fig.3.26. The global DC-bus voltages in two conditions have been shown in Fig.4.8 and Fig.4.10 where V_{DC}deviates slightly from$V_{DC}^{*} = 800V$. It appears mainly due to presence of 100Hz component arises due to unbalance power transfer.

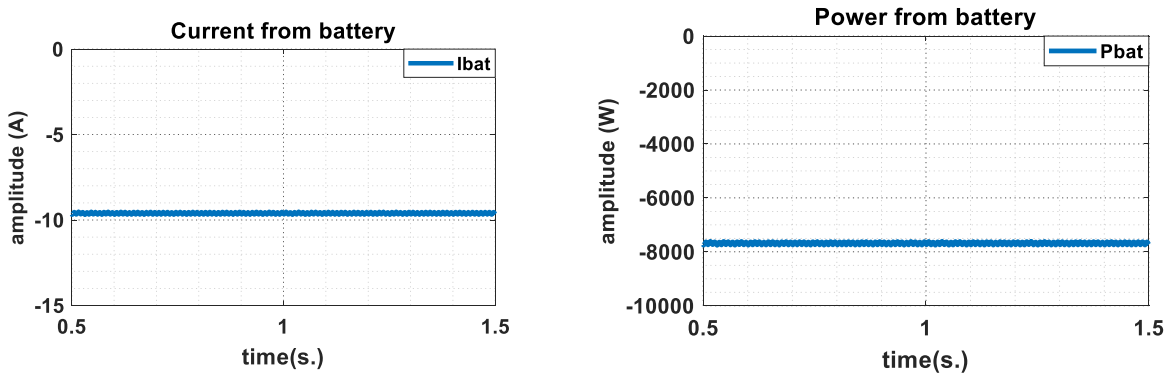

(a) *(b)*

Fig.4.11 a. Current from battery b. Power from battery [Test condition: $P_a = P_b = P_c = 7kW$ and $Q_a = Q_b = Q_c = 0kVAr]$

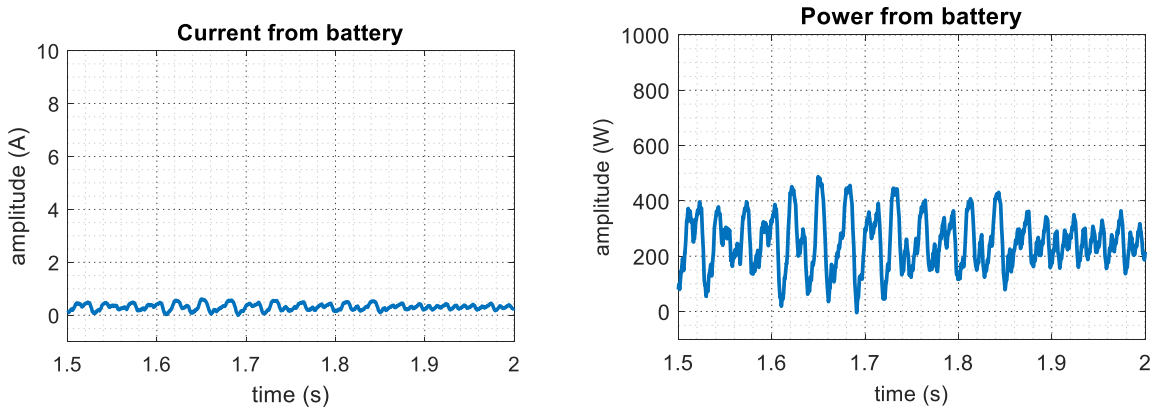

(a) *(b)*

Fig.4.12 a. Current from battery b. Power from battery [Test condition: $P_a = 2.3\ kW, P_b = -1.16kW, P_c = -1.16kW$ and $Q_a = 0kVAr, Q_b = -2.01kVAr, Q_c = 2.01kVAr]$

Fig.4.11 and Fig.4.12 represent the battery current and battery power in the closed loop control strategy of the integrated bidirectional EV battery charger for both single phase and 3-phase unbalance power exchange conditions respectively. Analytically, $I_{bat} = \frac{7000}{800} = 8.75A$ and $I_{bat} = \frac{20}{800} = 0.025A$ for both the mentioned conditions respectively. However, they are observed as 9.4A and 0.25A respectively from Matlab/Simulink result. In addition, P_{bat} values are settled at 7.52kW and 200W instead of 7kW and 20W respectively. Thus, 520W and 180W system losses are observed in the integrated EV battery charger during 3-phase balance and unbalance power conditions respectively. As ideal switches are used in the system, these losses are coming from the resistive part of the transformer used in TAB and the resistances associated to the DC-bus capacitors and the grid-connected AC-filter.

From Fig.4.12.b, it is also observed that the battery power has been oscillated during 3-phase unbalance power exchange condition. This is due to the 100Hz component present in the DC-bus at this operating point. Though we have selected 20Hz as the cutoff frequency of the TAB PI controller for the energy sum for avoiding the control of compensating the 100Hz

component, the issue comes mainly from the characteristics of the power transfer at the TAB level. Indeed the power, transferred from the battery to the DC-bus, depends on the controlled phase shift, but also on the amplitude of the DC-bus. If oscillations are presented in one DC-bus capacitor voltage, these oscillations will affect the power transfer due to following relation.

$$\boldsymbol{P = \frac{V_a V_b sin\varphi}{\omega L}} \quad \textbf{(89)}$$

Where V_a =Battery side H-bridge voltage of the TAB
V_b =NPC side H-bridge voltage of the TAB
φ =Phase shift between V_a and V_b
L = Energy transfer inductor

So from all the presented results in Matlab/Simulink platform, it is observed that ΔV are almost nullified in both the unbalance conditions with the whole integrated charger. So the control strategy of the converter has been validated and it justifies our configuration of the charger that can support the unbalance power exchange between the grid and the car battery. However, small ΔV oscillation still persists. It seems that this small limit is coming from the linearization of the control strategy. As from Equ. 89, it is observed that the power transfer is based on $sin\varphi$ but in our control strategy, we consider it only as φ. With the small values of φ, $sin\varphi \rightarrow \varphi$.

4.4 Conclusion

Thanks to all the results obtained from Matlab/Simulink, it can be concluded that the bidirectional onboard EV battery charger can support the objectives of the thesis, which are:

a. Single-phase power transfer.
b. Bidirectional power transfer in 3-phase balanced network condition.
c. Bidirectional power transfer while compensating and mitigating unbalance active and reactive power exchange between supplies of three phases.

Thus, the developed bidirectional EV battery charger can inject the current to the grid, when required.

Control strategy of the bidirectional DC/DC converter (TAB) along with the control strategy of the bidirectional AC/DC converter (4-leg NPC) further reduces the voltage difference of the DC-bus capacitors to almost zero, in all operating conditions. This, in turn, is helpful in integrating the onboard EV battery charger due to lesser volume and weight.

Chapter 5

GENERAL CONCLUSIONS AND FUTURE WORKS

This section of the thesis presents the general conclusions of the thesis and the future works, which can be done based on it, regarding bidirectional EV battery charger with V2G application.

5. Conclusion

The work, presented in this thesis, concerns the requirements of V2G application and the development of the onboard bidirectional charger for EVs. This thesis has been done with the collaboration between Institut VEDECOM and G2ELab, Université Grenoble Alpes. Institut VEDECOM is an Institute for Energy Transition (ITE) that works in the field of low-carbon energy sources. Founded in 2014, it brings together both the academic research (for e.g., UGA, Cetim, ESIGELEC, ESTACA etc.) and industrial skills (for e.g., PSA, Groupe Renault, Safran, Valeo etc.). Under the domain of vehicle electrification and sub domain of innovative charging systems, this research studies have been done.

5.1 General conclusions

Because of concernment and awareness of the environment, most of the countries are relying on EVs as future transportation rather than ICE based vehicles. In order to betterment of nature, battery of these EVs can be considered as energy producers during their idle time. These G2V and V2G applications require bidirectional power transfer capability of EV's battery charger. The power electronics part of EV battery charger can provide this bidirectional power transfer operation, considering all the constraints of grid codes and safety towards car owner. **In Chapter 1,** different topologies of the Power Electronics parts of the bidirectional EV battery chargers and all the benefits and the ancillary services, provided by V2G application, have been discussed in detail. After investigating the literature reviews, it was understood that a lot of works had already been done on V2G applications and the charger configurations. But all these works were based mostly on the balanced power network. This motivates me to work on the power electronic configurations of the bidirectional EV battery charger that can support network with unbalance power supply.

One of the main constraints of the bidirectional EV battery charger was that it should be onboard in nature. Keeping that in mind, aim was to develop an optimal EV battery charger in terms of weight and volume. With this objective, calculations of passive elements of the selected charger have been done. One of the goals of this thesis is to develop the bidirectional EV battery charger that will support unbalance current injection condition of the grid. For this purpose, different configurations of bidirectional AC/DC converters, which can provide the neutral connection, have been studied and compared starting from 2-level VSC to multilevel VSC. After studying different pros and cons of different converters both in balanced and unbalanced network power, NPC configuration has been selected as an AC/DC bidirectional converter in **Chapter 2.** Though we have selected NPC topology in comparison with 2-level VSC but it will be interesting to compare this NPC structure with other multilevel VSC structure namely flying capacitor. The main reason to select NPC over 2-level VSC was the weight and volume. From the tests, it was proved that voltage oscillation at the middle point

of the DC-bus will be more in 2-level VSC compared to that of NPC with increase in power unbalance. This happens because of some compensation current due to structure of the NPC. As a result, we need smaller size of the DC-bus capacitors in NPC compared to 2-level VSC, considering$\Delta V \leq 5\%\ of\ V_{DC}$.

In **Chapter 3,** closed loop control strategy of the selected configuration of bidirectional AC/DC converter, which is 4-leg NPC, has been developed. With the developed control strategy, homopolar current controller and the DC-bus voltage controller are decoupled. For particular parameters, tests have been done with and without voltage control loop in order to justify its necessity. Since, we are working on unbalance power in three phases, generated reference currents contain both the DC and AC component in the Park domain. This leads to necessity to use R-controller and develop its design. However, another control strategy can be thought. In which, regardless of transforming the reference quantities in Park domain, they can directly be controlled by the R-controller. But in that case, space in the Zynq processor (required to implement the control logic) can be a problematic. As resonant controller is a second order controller, it requires more space in the processor compared to PI controller. However, we gain some space in the Zynq processor as we do not need to implement Park and inverse Park transformation, if we implement our controllers in AC-domain. So there is a trade-off and this can be investigated. Also PI current controller had been designed by comparing the transfer function of the system and the controller. It can be done with Pole-Zero compensation method by defining the particular bandwidth. After implementing this control strategy, comparison has been done between 3-leg NPC and 4-leg NPC in terms of weight and volume of the converter to show the effectiveness of the 4-leg NPC. According to the developed closed loop control strategy of 4-leg NPC converter and its design, tests have been performed at different operating points with the help of Matlab/Simulink and HIL results. According to the obtained results, it was observed that reference and measured phase currents were overlapped. Also Δv was within the threshold limit of 5% of V_{DC}. These results validate the design of the controllers and the developed control strategy. Though the threshold limit of Δv had been respected, but still another configuration of the AC/DC converter was thought where one extra leg had been added to the 4-leg NPC through an inductor. With this configuration Δv had almost been nullified however this configuration had not been studied further due to the presence of an extra inductor. It can be an interesting study to compare between these two structures. As though an extra leg with two IGBTs and an inductor were added but we can almost nullify Δv that leads to a lower sized DC-bus capacitor. Thus, there is a trade-off between these two passive elements.

In **Chapter 4,** closed loop control strategy of the selected configuration of bidirectional DC/DC converter, which is TAB, has been developed. The purposes of utilizing TAB as a bidirectional DC/DC converter are that it is insulated in structure and feed the upper and lower capacitors of the DC-bus separately in order to limit the voltage fluctuations. So that the amount of power delivered on each half of The DC-bus will be controlled precisely. The developed control

strategy of the integrated charger has been implemented both in Matlab/Simulink platform. Our aim was to nullify ΔV completely with the help of TAB and with our proposed control strategy that is achieved and shown in Matlab/Simulink results.

5.2 Future works

In this thesis, configuration of the bidirectional onboard EV battery charger has been proposed that can compensate and mitigate unbalance active and reactive powers exchange between 3-phase supply. Also control strategies are developed for both AC/DC and DC/DC converters. Apart from the propositions, mentioned in the conclusion part to understand the topic further, below works can be done in future for improving this thesis objectives:

1. Test point with the worst unbalance condition

In this thesis, tests had been done on the single phase power transfer condition and a test point where neutral current is equal to 32A (r.m.s). But apart from that test point, there are other unbalance three phase active and reactive powers that can lead to worse situation. It should be necessary to study the whole range of operating points and their impacts on the converter sizing. We can try to find that worse test point and compare with single phase power transfer condition.

2. Optimization of passive elements of the converter

In this thesis, comparisons between the converters had been made on the size of passive elements, namely AC-inductor and the DC-bus capacitors. However, adding an extra leg with the 3-leg NPC will increase the complexity of the control strategy and also the weight and volume of the charger due to extra semiconductor switches and the associated driver circuits. So proper optimization of the passive elements can help to find the best suitable structure of the embedded charger in terms of power density.

3. Experimental test of the developed control strategies

The control strategy of the AC/DC converter had been validated both in offline Matlab/Simulink platform and real-time HIL platform while the whole charger that includes both AC/DC and DC/DC converters, had been validated in offline Matlab/Simulink platform in this thesis. Thus, the control strategy of the whole integrated charger can be validated in real time HIL platform and then experimental tests have been required to validate the developed control strategies fully. With the help of experimental tests, the efficiency of the charger can also be measured.

4. Study of other types of AC/DC bidirectional converter structures

It can be useful to study other AC/DC bidirectional converter topologies that can allow the advantages of the multilevel configuration as well as without having capacitive middle point problem, such as, Flying Capacitor structure.

5. In order to avoid the perturbations passing through the transformer in the TAB, it could be imaginable to adapt the control laws that can reject the perturbations by adding a Phi variation in compensating the voltage variation at the DC-bus side.

Résumé de la thèse

En raison de l'industrialisation et de l'augmentation exponentielle de la population mondiale, la consommation de combustibles fossiles augmente également. Les risques environnementaux, tels que les émissions de gaz à effet de serre et l'augmentation de la température mondiale sont les effets d'une consommation accrue de combustibles fossiles. Il attire l'attention de la communauté de la recherche et du développement (R&D) et amène les gouvernements du monde entier à élaborer des politiques pour résoudre ce problème.

Différentes mesures préventives ont été prises afin de réduire les émissions de gaz à effet de serre. Telles que la production d'énergie verte à partir de sources d'énergie renouvelables (éolienne, hydraulique, solaire, géothermique et marémotrice, etc.) sont favorisées, ainsi que des méthodes de consommation et de stockage plus efficaces de l'énergie produite sont adoptées. Les véhicules électriques (VE), aident également la nature, car ils n'ont pas d'émissions d'échappement. En fait, ils n'ont même pas d'échappement. Compte tenu de l'impact de la production d'électricité utilisée, les véhicules électriques purs peuvent toujours produire des gaz à effet de serre nettement inférieurs à ceux des voitures à essence ou diesel. Ces émissions seront encore réduites à mesure que le monde passera à une production d'électricité plus renouvelable et nucléaire.

À l'aide d'un chargeur de batterie bidirectionnel, les véhicules électriques peuvent non seulement être considérés comme un consommateur d'énergie, mais aussi comme un producteur d'énergie. Vehicle-to-Grid (V2G) est une technologie dans laquelle les VE déchargent leur énergie stockée et l'injectent sur le réseau pendant la période de charge de pointe. Ainsi, il ne doit pas seulement être considéré comme des charges passives mais aussi comme des sources d'énergie tout en étant au repos. La technologie V2G offre également un potentiel pour fournir des services auxiliaires dans les secteurs de l'énergie, tels que la régulation de tension, le rasage de tension, la compensation de puissance réactive et la production distribuée. S'il est bien géré, EV devient un atout attractif pour DSO. Ainsi, le chargeur de batterie des VE devrait fournir les fonctionnalités ci-dessous:

1. Chargement de la batterie (fonction principale): Dans ce cas, la puissance est transférée du réseau au véhicule, appelée opération G2V.
2. Décharge de la batterie (fonction secondaire): Dans ce cas, l'unité de stockage d'EV, c'est-à-dire la batterie, est considérée comme une source d'énergie et la puissance est transférée du véhicule au réseau.
3. Capacité d'équilibrage du réseau (fonction tertiaire): les véhicules électriques peuvent fournir des services auxiliaires au réseau, tels que la puissance réactive ou le déséquilibre de la consommation / injection de courant pour aider à équilibrer et maintenir le réseau sans cyclage de batterie supplémentaire.

Les deux premières fonctionnalités avaient déjà été abordées par des chercheurs précédents (également dans G2ELab par le Dr Mounir Marzouk). Cette thèse se concentre sur la troisième fonctionnalité mentionnée qui peut être fournie par les véhicules électriques.

Chapitre 1

1.1 L'Introduction

Le secteur des transports, dépendant des moteurs à combustion, contribue à une grande quantité de CO2 dans l'atmosphère. Récemment, l'électrification du secteur des transports a attiré l'attention du monde entier en tant que solution potentielle et prometteuse aux problèmes susmentionnés. En conséquence, l'intérêt pour les véhicules électriques a augmenté rapidement ces dernières années et cette tendance semble continuer de croître dans un proche avenir.

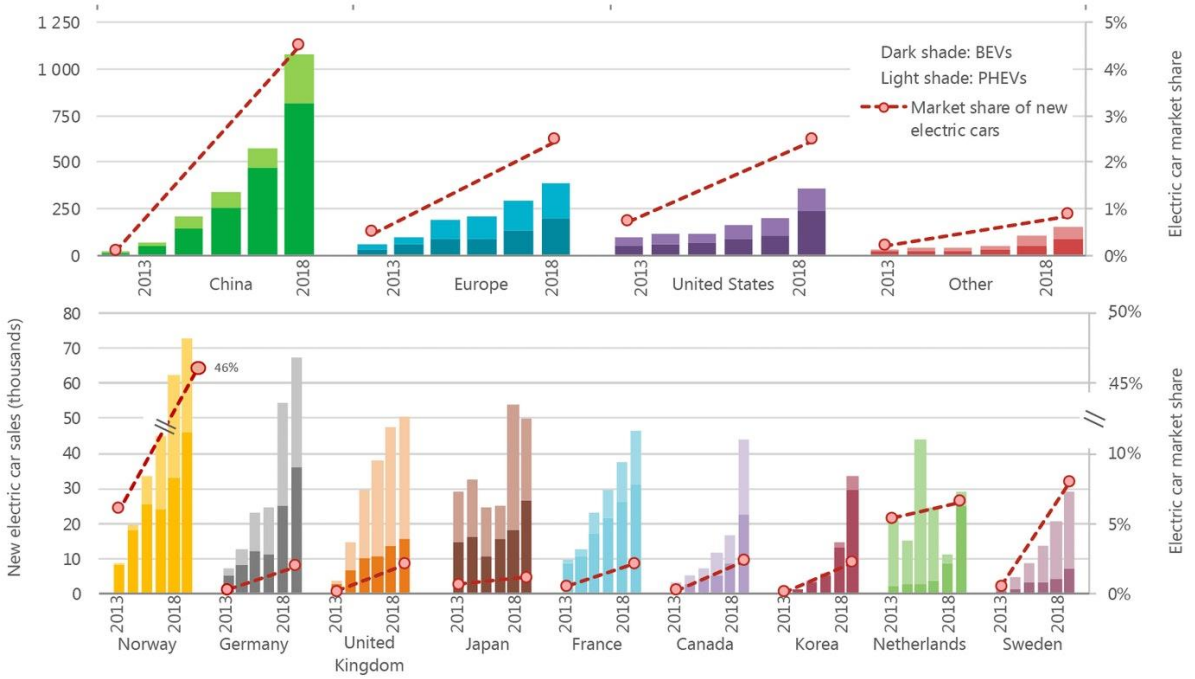

Fig.R.1 Ventes mondiales de véhicules électriques et part de marché, 2013-2018

1.2 Concept et services annexes de la technologie V2G

Le but principal du chargeur de batterie EV est de transférer l'énergie à la batterie (G2V), mais il est possible d'utiliser le chargeur de batterie bidirectionnel et de fournir certains services auxiliaires du réseau : **le rasage de puissance de pointe, la réglementation, la prise en charge**

de l'intégration des énergies renouvelables et des revenus génération pour les utilisateurs de VE.

Ce concept est bien présenté sur la Fig. R.2.

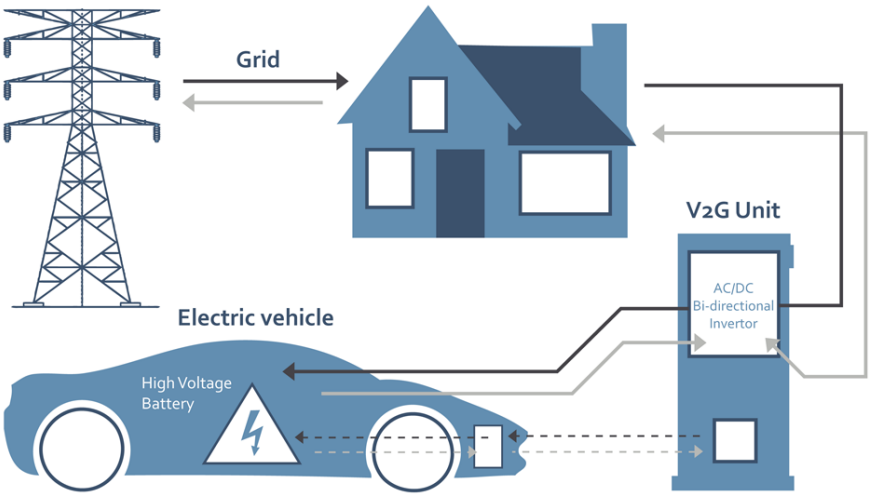

Fig.R.2 Concept de flux d'énergie bidirectionnel entre EV et réseau

1.3 Topologie du chargeur de batterie EV bidirectionnel

La topologie typique du chargeur de batterie EV bidirectionnel a été représentée sur la Fig. R.3. Le chargeur de batterie bidirectionnel EV se compose de deux étapes. Le premier étage se compose d'un convertisseur AC / DC, qui facilite le flux de puissance bidirectionnel du réseau vers la liaison DC du convertisseur DC / DC. De plus, il maintient le facteur de puissance unitaire. Le deuxième étage se compose d'un convertisseur DC / DC, qui régule le courant et la tension de la batterie.

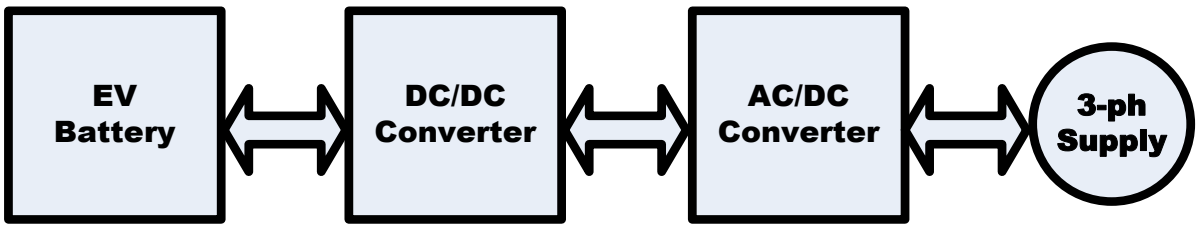

Fig.R.3 Topologie du chargeur de batterie EV bidirectionnel

1.4 Objectif de la thèse

En permettant un flux d'énergie bidirectionnel avec la technologie V2G, les VE ne sont pas seulement considérés comme une charge sur le réseau, mais agissent également comme des systèmes de stockage et de production distribués. Les VE pouvant être utilisés comme unité de production d'énergie active et réactive, nous souhaitons aller plus loin dans les capacités qu'ils permettent. En permettant l'échange de puissance active et réactive, la technologie V2G assure les services auxiliaires précédemment présentés et également présentés dans la thèse de doctorat de Mounir Marzouk sur le chargeur de batterie bidirectionnel triphasé 22kW pour camions hybrides en condition d'échange de puissance d'équilibre entre trois phases. Dans cette thèse, nous voulons étudier la possibilité d'efficacité du chargeur également dans des conditions d'échange de puissance de déséquilibre. Ainsi, la motivation principale de ce travail de recherche est de **compenser et d'atténuer le déséquilibre d'échange de puissance active (P) et réactive (Q) entre l'alimentation de trois phases.**

Dans les réseaux basse tension, de nombreuses charges sont monophasées, ce qui introduit des problèmes très courants dans ces réseaux. Cela crée un déséquilibre dans la consommation d'énergie ($P_1 \neq P_2 \neq P_3$), qui à son tour crée un déséquilibre du courant dans le réseau, comme illustré à la Fig. R.4.

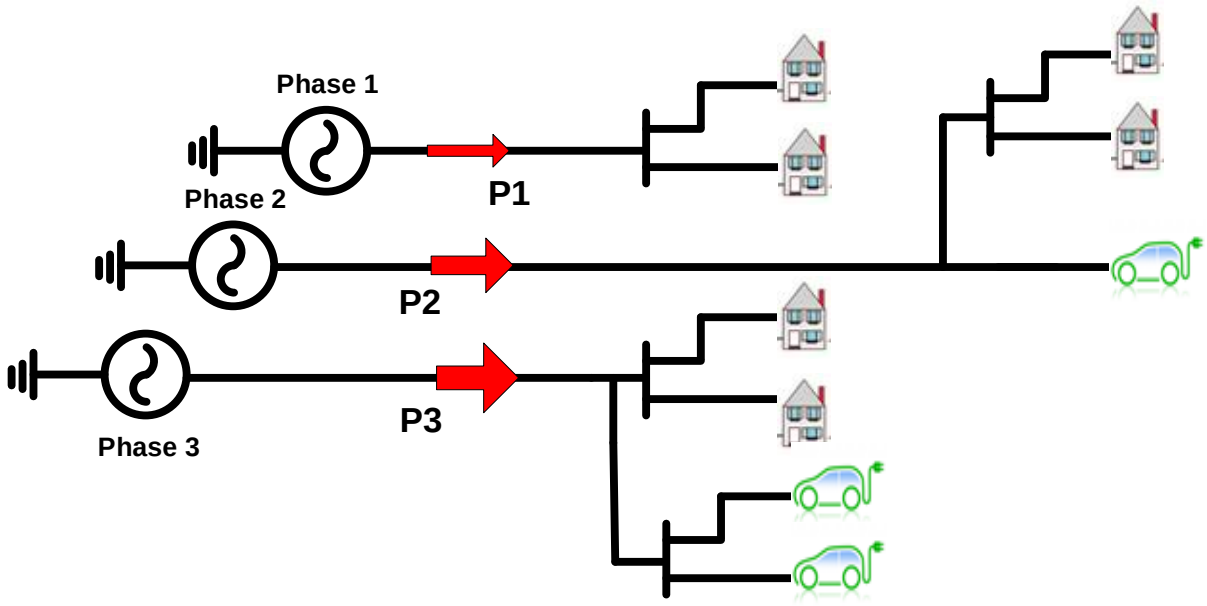

Fig.R.4 Déséquilibre dans le réseau dû à une consommation d'énergie inégale par charge monophasée

Ce déséquilibre de courant a des impacts négatifs sur le réseau, tels que,

- Augmentation du courant neutre qui peut créer une surchauffe et une défaillance d'isolation du conducteur de ligne.

- Les courants de séquence négative, générés en raison de l'affaissement de la tension de déséquilibre, ont des impacts négatifs sur l'ensemble du système de distribution d'énergie. Il réduit le rendement des transformateurs, des lignes de transmission et des machines côté charge.

Afin d'atténuer le déséquilibre de courant, la puissance active ou réactive requise doit être injectée au réseau à partir de l'unité de stockage extérieure, qui peut être une batterie EV avec un convertisseur bidirectionnel. Il peut redistribuer les courants en injectant ou en absorbant la bonne quantité de puissance active et réactive de chaque phase, comme le montre la Fig. R.5.

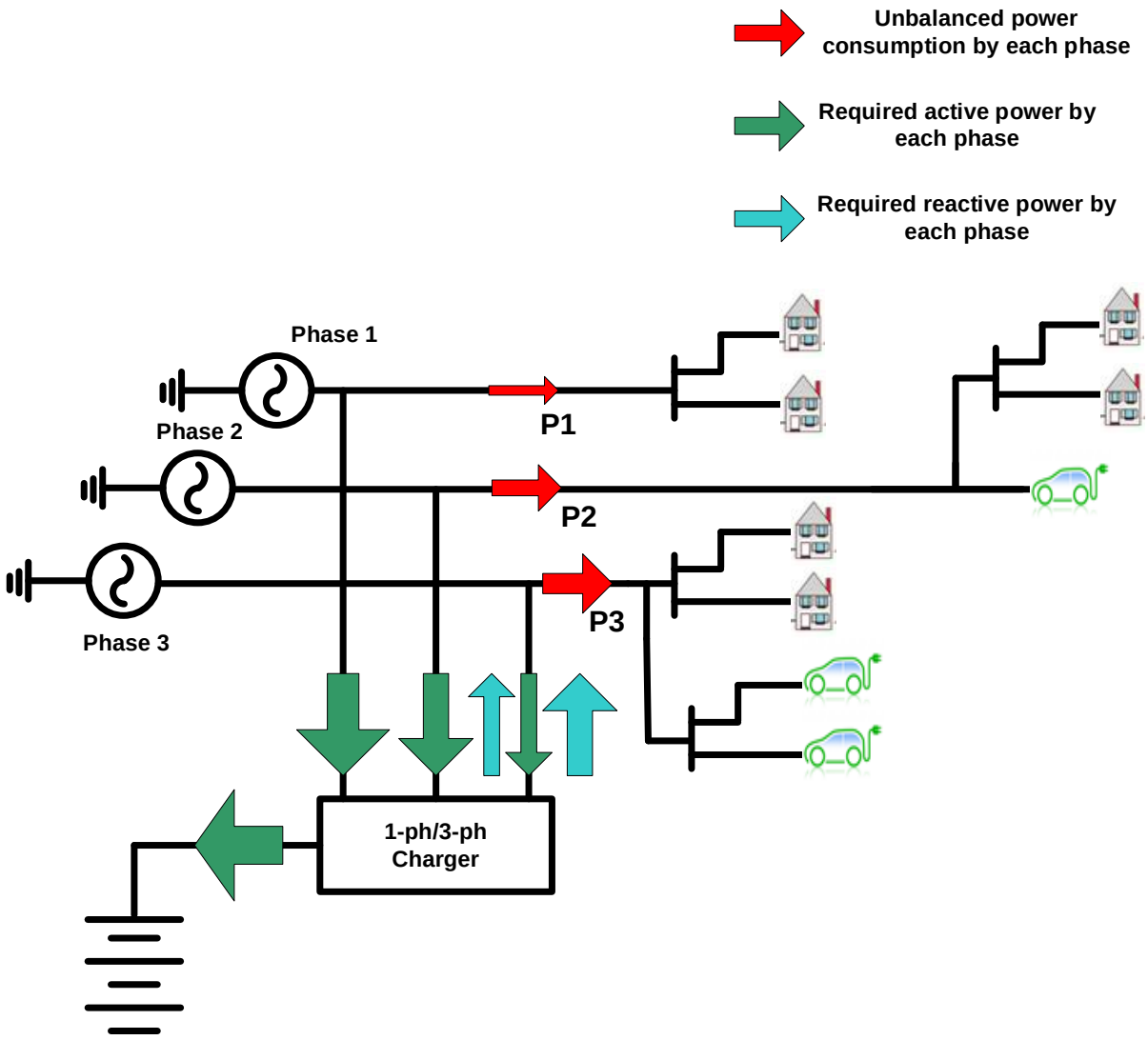

Fig.R.5 Atténuation du déséquilibre de courant en consommant et en injectant des puissances actives et réactives au réseau

Cette compensation et atténuation du déséquilibre des courants fournit les services de support de réseau suivants, qui est l'une des principales motivations des applications V2G:

- Le décalage du point neutre et ses problèmes associés peuvent être résolus.
- Étant donné que les courants sont équilibrés, la moyenne sera plus faible et cela réduira la perte de réseau, le problème de chauffage et les fluctuations de tension du réseau.

1.5 La conclusion

Sur la base des motivations des travaux de recherche, les contributions de cette thèse peuvent être résumées comme suit:

- Comparaison entre différentes configurations de convertisseurs bidirectionnels AC / DC en termes de taille des éléments passifs, de contenu harmonique et de THD.
- Sélection d'un convertisseur bidirectionnel AC / DC qui peut prendre en charge une situation d'injection de courant de déséquilibre.
- Sélection de la configuration du convertisseur DC / DC bidirectionnel isolé.
- Modélisation et contrôle du chargeur EV bidirectionnel à deux étages sélectionné.

Chapitre 2

2.1 L'Introduction

Comme observé sur la Fig. R.3, la topologie du chargeur de batterie EV bidirectionnel comprend un convertisseur AC/DC bidirectionnel. Dans les topologies triphasées classiques, seules trois phases sont connectées et le point neutre est mis à la terre. Néanmoins, l'un des principaux objectifs de cette activité de recherche est de compenser et d'atténuer le déséquilibre de l'échange de puissance active et réactive entre l'alimentation du réseau triphasé, c'est-à-dire de faire fonctionner le chargeur de batterie EV bidirectionnel en situation de déséquilibre de courant. Afin de pouvoir injecter des courants déséquilibrés dans le réseau, il est nécessaire d'avoir le point neutre connecté à la structure du convertisseur. Il existe des solutions pour connecter le neutre du réseau au convertisseur, telles que,

i) Utilisation de trois ponts en H

ii) Division du bus DC du convertisseur

iii) Convertisseur avec quatrième bras

Trois ponts en H peuvent être connectés au réseau triphasé à 4 fils à l'aide de trois transformateurs d'isolement comme indiqué sur la figure 2.1. Les inconvénients de la structure sont l'utilisation d'un grand nombre d'interrupteurs à semi-conducteurs et de plusieurs transformateurs basse fréquence, qui sont lourds, encombrants et difficiles à intégrer dans un véhicule.

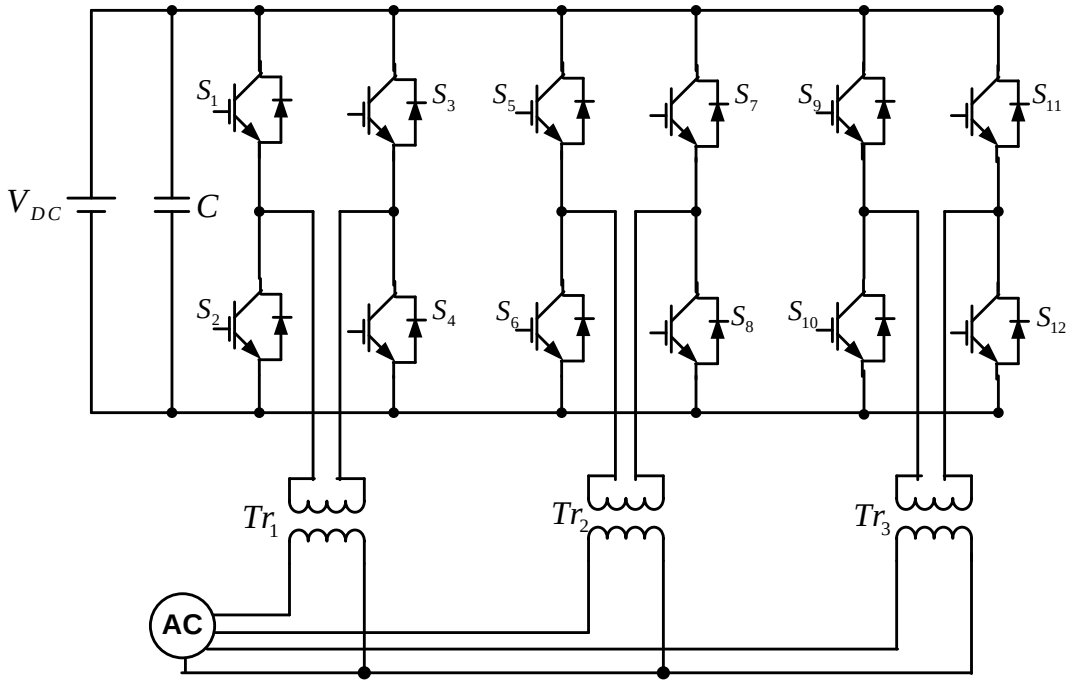

Fig.R.6 Configuration du convertisseur en pont en H avec une connexion neutre

La séparation des condensateurs du bus DC et la connexion du point neutre au point médian du bus DC est une solution simple et économique. Dans le cas du VSC à 2 niveaux, une configuration triphasée à 4 fils peut être possible en divisant le condensateur du bus DC en deux parties, comme indiqué sur la Fig. R.7.

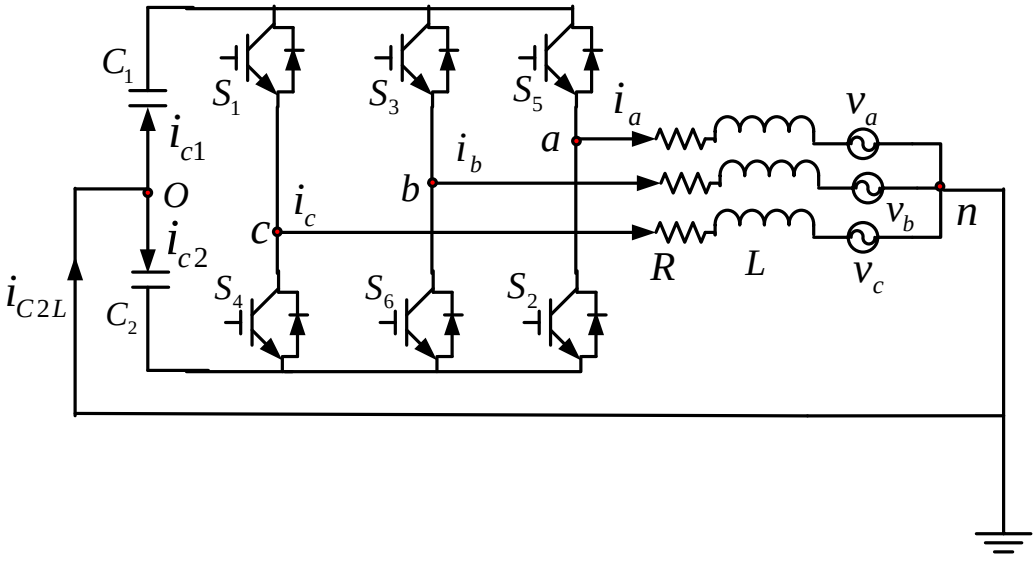

Fig.R.7 VSC bidirectionnel triphasé à 3 branches 4 fils à 2 niveaux

Dans le cas de NPC, ce point médian du bus DC existe déjà en raison de la structure du convertisseur et il est illustré sur la Fig. R.8. La topologie de convertisseur triphasé 4 fils offre également une sécurité sur la circulation du courant de fuite entre EVSE et la voiture.

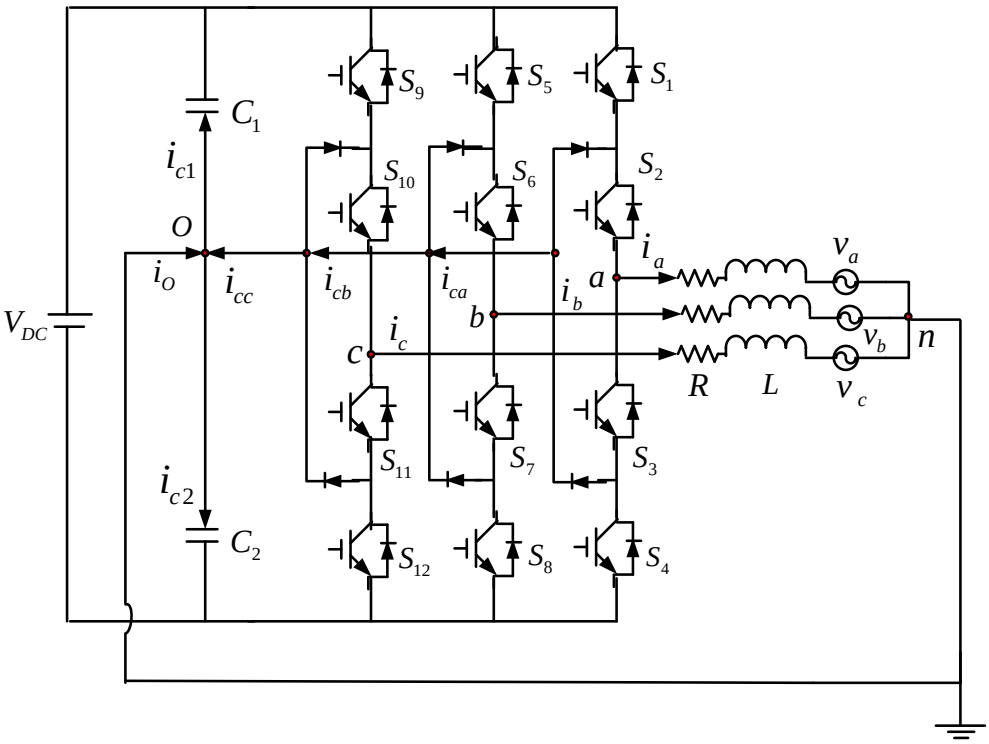

Fig.R.8 VSC bidirectionnel triphasé 3-bras 4 fils 3 niveaux

L'un des défis majeurs avec le convertisseur 3 bras 4 fils 2 niveaux ou 3 niveaux est d'équilibrer la tension du point médian des condensateurs de bus DC en configuration d'injection de courant déséquilibré. En raison des courants injectés, la différence entre les deux tensions de condensateur peut augmenter / diminuer (dépend de la direction du courant neutre) et cela créera une oscillation (due à un écart par rapport au point médian réel de la source DC) au point médian de le bus DC. Cette oscillation doit être limitée afin d'assurer des injections de courant correctes. Cette oscillation peut être limitée en augmentant la taille des condensateurs du bus DC, mais cela augmentera la taille et le poids globaux du chargeur embarqué.

Les inconvénients de ces deux configurations peuvent être partiellement résolus en ajoutant un quatrième bras entièrement contrôlable et en connectant le point neutre à ces bras comme indiqué sur la Fig. R.9. Les inconvénients de cette configuration sont:

- Diminution de la fiabilité en raison de la multiplication des commutateurs à semi-conducteurs et des pilotes de grille associés.
- Augmentez la complexité du circuit de commande du convertisseur.
- Inductance supplémentaire sur le neutre.

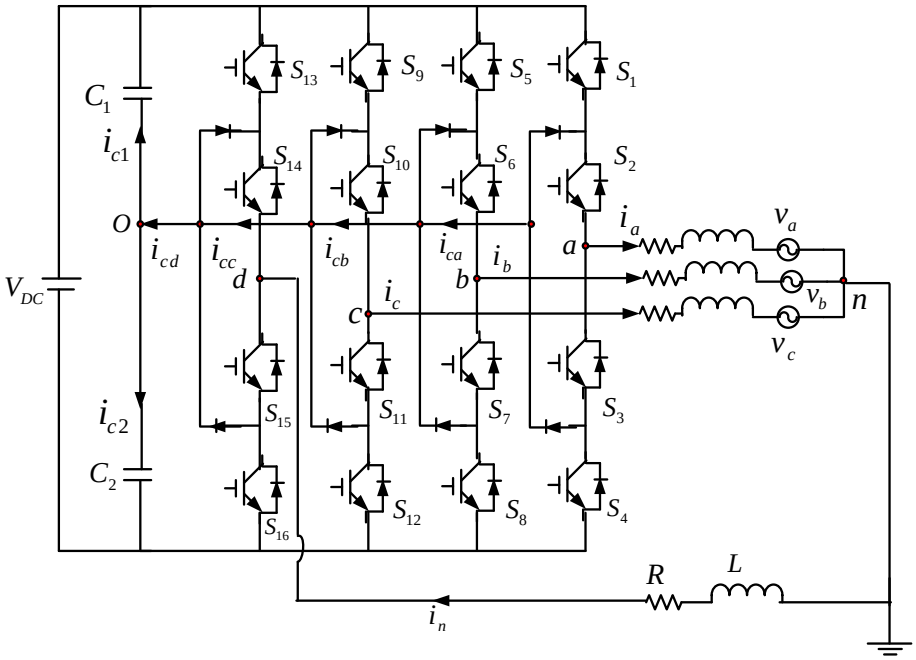

Fig.R.9 VSC bidirectionnel triphasé 4-bras 4 fils 3 niveaux

2.1.1 Comparaison entre les convertisseurs de source de tension à 2 niveaux et multi-niveaux

Dans la section, la comparaison et la sélection entre l'onduleur triphasé 3 bras 4 fils 2 niveaux et l'onduleur NPC ont été effectuées dans différentes conditions tous les deux dans Matlab/Simulink et banc d'essai expérimental :

- Réseau avec échange de puissance d'équilibrage entre phases
- Fonctionnement monophasé entre une phase et le point neutre
- Injection de puissance active et réactive de déséquilibre pour l'atténuation du courant dans le réseau

Dans la topologie de convertisseur à 3 bras, l'oscillation de tension au point médian des condensateurs du bus DC est importante et doit être vérifiée et limitée.

Dans ces tests expérimentaux, VSC et NPC à 2 niveaux sont utilisés comme VSI en fournissant une tension d'alimentation DC constante (V_{DC} = 200 V) et ils sont connectés à une charge RL en étoile triphasée où R passe de 100Ω à 40Ω avec 3 points de test intermédiaires tandis que L = 5mH (en raison de la disponibilité en laboratoire). Pendant le fonctionnement monophasé, la charge est connectée entre une phase (pour une phase a par exemple) et le point neutre pour un VSI à 2 et 3 niveaux. Pour créer une condition d'injection de puissance active et réactive de déséquilibre, les charges de phase 'a' et 'b' sont connectées tout en déconnectant la charge de phase c pour effectuer la configuration comme, $P_1 = P_2 = P\ W \neq P_3$ = 0W.

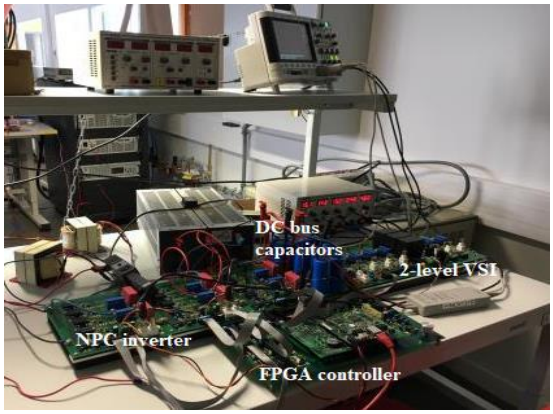

Fig.R.10 Configuration expérimentale d'un VSC triphasé 4 fils 2 niveaux et 3 niveaux

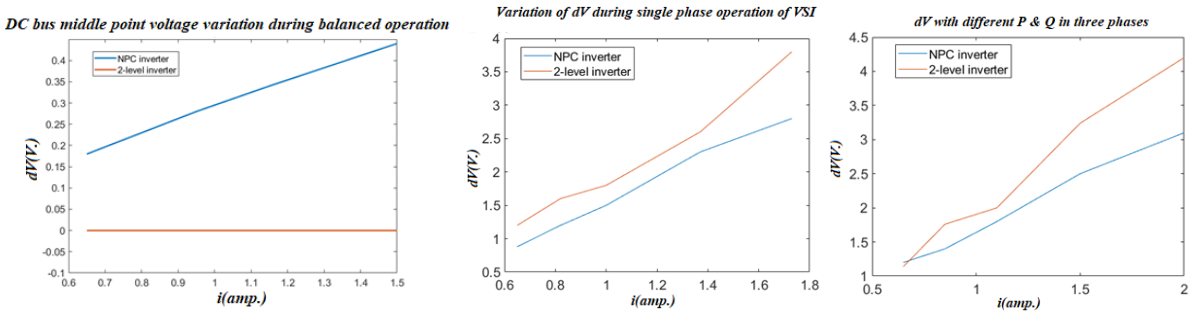

(a) *(b)* *(c)*

Fig.R.11 Comparaison des oscillations de tension au point médian du bus DC pour les VSI à 2 niveaux et 3 niveaux avec des données expérimentales a. en état de fonctionnement équilibré b. en fonctionnement monophasé c. pour différentes injections de puissance active et réactive

En cas de transfert de puissance d'équilibrage, un courant nul circule dans le fil neutre du VSI à 2 niveaux et, par conséquent, aucune oscillation de tension n'est observée dans le bus DC. En raison de la structure du NPC, une composante de courant de 150 Hz (3 fois la fréquence fondamentale) circule au point médian du bus DC et qui conduit l'oscillation de tension du bus DC. Cette oscillation augmente avec le courant neutre.

Pour les conditions d'échange de puissance monophasée et déséquilibrée, qui est l'objectif principal de cette thèse, les oscillations de tension au point médian du bus DC sont moindres dans le cas d'un VSI à 3 niveaux par rapport à un VSI à 2 niveaux. De plus, le taux d'incrémentation de dV est plus élevé dans les onduleurs à 2 niveaux, avec incrément de courant neutre. Ainsi, des condensateurs de valeurs nominales plus élevées doivent être utilisés dans un VSI à 2 niveaux que dans un VSI à 3 niveaux afin de limiter les dV dans une plage. Cela augmente à son tour le poids et le volume du VSI à 2 niveaux. Ainsi, on peut conclure que le VSC à 3 niveaux est meilleur que le VSC à 2 niveaux pendant une condition d'échange de puissance monophasée et déséquilibrée entre trois phases en termes de volume et de poids du convertisseur AC / DC.

2.2 Comparaison entre les convertisseurs triphasés à 3 bras 4 fils et triphasés à 4 bras dans différentes conditions de réseau

Sur la base du modèle Mathcad, le tableau 1 a été préparé pour comparer entre Δv_{C3leg} et Δv_{C4leg} dans différentes conditions d'échange de puissance entre trois phases avec le même condensateur, alors que le tableau 2 a été préparé pour comparer entre Δv_{C3leg} et Δv_{C4leg} dans différentes conditions d'échange de puissance entre trois phases avec des condensateurs différents qui peuvent assurer $\Delta v_{C4leg} = 5\%\ de\ V_{DC}$.

$C\ (\mu F)$	$P_1(kW)$	$P_2(kW)$	$P_3(kW)$	$Q_1(kVar)$	$Q_2(kVar)$	$Q_3(kVar)$	$\Delta v_{C3leg}(V)$	$\Delta v_{C4leg}(V)$
245	**7.36**	**0**	**0**	**0**	**0**	**0**	**177.4**	**119.8**
245	**7.36**	**3.68**	**3.68**	**0**	**0**	**0**	**94.62**	**59.9**
245	**7.36**	**0**	**0**	**0**	**-3.68**	**-3.68**	**212.5**	**133.7**
245	**2.3**	**-1.16**	**-1.16**	**0**	**-2.01**	**2.01**	**62**	**39.16**

Tableau 1: Comparaison des oscillations de tension du bus DC entre les NPC à 3 et 4 bras dans différentes conditions d'échange d'énergie avec le même condensateur

$C\ (\mu F)$	$P_1(kW)$	$P_2(kW)$	$P_3(kW)$	$Q_1(kVar)$	$Q_2(kVar)$	$Q_3(kVar)$	$\Delta v_{C3leg}(V)$	$\Delta v_{C4leg}(V)$
733	**7.36**	**0**	**0**	**0**	**0**	**0**	**44.9**	**40**
365	**7.36**	**3.68**	**3.68**	**0**	**0**	**0**	**87.48**	**40**
820	**7.36**	**0**	**0**	**0**	**-3.68**	**-3.68**	**44.8**	**40**
238	**2.3**	**-1.16**	**-1.16**	**0**	**-2.01**	**2.01**	**63.35**	**40**

Tableau 2: Comparaison des oscillations de tension du bus DC entre les NPC à 3 et 4 bras dans différentes conditions d'échange d'énergie avec différents condensateurs

D'après le Tableau 1 et le Tableau 2, il est observé que toujours $\Delta v_{C3leg} \geq \Delta v_{C4leg}$, pour les mêmes capacités de condensateur et les mêmes conditions de réseau. Ainsi, nous pouvons conclure que les condensateurs de bus DC de puissance nominale plus élevée sont nécessaires dans les NPC à 3 bras par rapport aux NPC à 4 bras dans des conditions de réseau similaires pour obtenir Δv_C dans notre limite autorisée. Grâce à tous ces tests et observations, nous pouvons conclure que le NPC à 4 bras est la meilleure structure bidirectionnelle AC / DC en termes de volume qui peut être intégrée au chargeur de batterie EV bidirectionnel embarqué qui peut injecter les puissances actives et réactives requises pour la grille.

Chapitre 3

3.1 L'Introduction

Dans ce chapitre, la stratégie de contrôle et la conception des contrôleurs pour le NPC à 4 bras, qui a été utilisé comme convertisseur AC / DC dans un chargeur de batterie EV bidirectionnel, ont été discutées.

3.2 Stratégie de contrôle globale du convertisseur NPC à 4 bras

La stratégie de contrôle globale du convertisseur NPC à 4 bras, qui prend en charge à la fois l'opération d'injection de courant d'équilibre et de déséquilibre, a été illustrée à la Fig. R.12. Pour contrôler le convertisseur NPC à 4 bras, quatre signaux de modulation doivent être générés. Grâce à la stratégie de modulation PD-PWM, ces signaux de modulation généreront les impulsions de grille nécessaires à la commutation des IGBT dans les quatre branches. A cet effet, trois contrôleurs de courant sont utilisés pour générer les signaux de modulation et qui contrôleront les phases a, b et c. Alors qu'un contrôleur de tension est utilisé pour générer le signal de modulation et qui contrôlera la phase neutre.

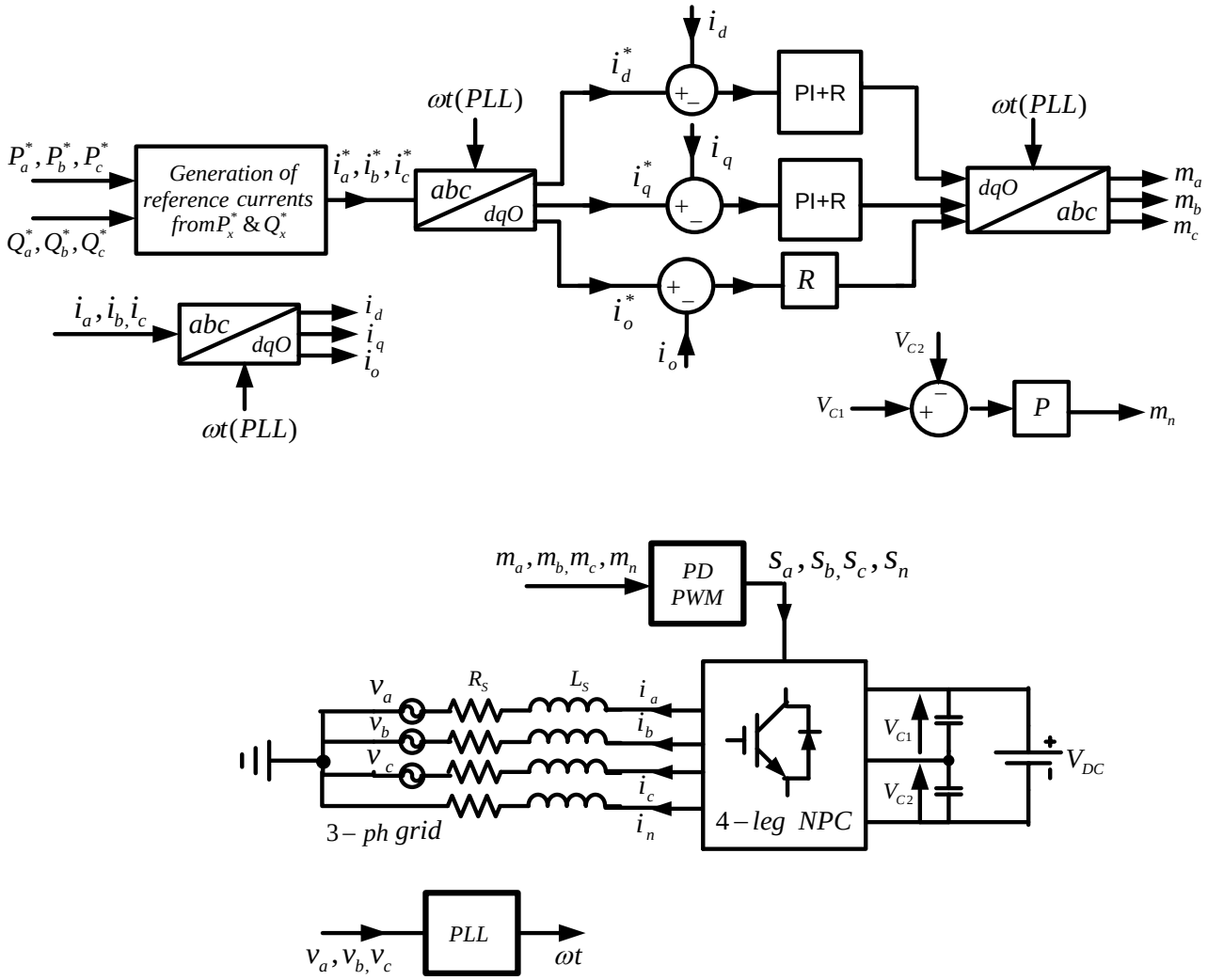

Fig.R.12 Stratégie de contrôle globale du NPC à 4 bras

Considérant un système d'équilibrage triphasé, pour un par ex.,

$$\boldsymbol{u_a = U_m sin\omega t,\ \ u_b = U_m sin(\omega t - \frac{2\pi}{3})\ \text{and}\ u_c = U_m sin(\omega t + \frac{2\pi}{3})}$$

$$\boldsymbol{u_d = U_m,\quad u_q = 0,\quad u_0 = 0}$$

D'après les calculs ci-dessus du système triphasé équilibré, on observe que:

- Le composant de l'axe-d est constitué du composant DC.
- Les composants de l'axe-q et de l'axe-0 ont une valeur nulle.

Mais en cas de système triphasé déséquilibré, par ex.,

$$\boldsymbol{u_a = U_{m1} sin\omega t,\ \ u_b = U_{m2} sin(\omega t - \frac{2\pi}{3} + \varphi_1)\ \text{and}\ u_c = U_{m3} sin(\omega t + \frac{2\pi}{3} + \varphi_2)}$$

$$\boldsymbol{u_d = \frac{1}{3}(U_{m1} + U_{m2} cos\varphi_1 + U_{m3} cos\varphi_2) - \frac{1}{3}\Big[U_{m1} cos2\omega t + U_{m2} cos(2\omega t - \frac{4\pi}{3} + \varphi_1) + U_{m3} cos(2\omega t + \frac{4\pi}{3} + \varphi_2)\Big]}$$

$$u_q = \frac{1}{3}(U_{m2}sin\varphi_1 + U_{m3}sin\varphi_2) + \frac{1}{3}\left[U_{m1}sin2\omega t + U_{m2}sin(2\omega t - \frac{4\pi}{3} + \varphi_1) + U_{m3}sin(2\omega t + \frac{4\pi}{3} + \varphi_2)\right]$$

$$u_0 = \frac{1}{3}\left[U_{m1}sin\omega t + U_{m2}sin\left(\omega t - \frac{2\pi}{3} + \varphi_1\right) + U_{m3}sin(\omega t + \frac{2\pi}{3} + \varphi_2)\right]$$

D'après les calculs ci-dessus du système de déséquilibre triphasé, on observe que:

- Le composant de l'axe-d et q se compose d'un composant DC et d'un composant AC d'une fréquence de 100 Hz (2f).
- Le composant de l'axe-0 se compose d'un composant AC de fréquence 50Hz (f).

Ces deux courants de référence de domaine Park et mesurés sont comparés et les erreurs ont été transmises à travers les contrôleurs de courant des axes d, q et 0. Dans le cas d'un système triphasé équilibré, des contrôleurs de courant PI peuvent être utilisés pour contrôler les courants car tous les composants sont DC. Cependant, pour un système à déséquilibre triphasé, les contrôleurs PI et R avec résonance à 100 Hz peut être utilisés pour contrôler les courants des axes d et q, tandis que le contrôleur R, avec résonance à 50 Hz, peut être utilisé pour contrôler le courant de l'axe 0.

3.3 Conception des contrôleurs

3.3.1 Conception des contrôleurs de courant

Le contrôleur de courant PI

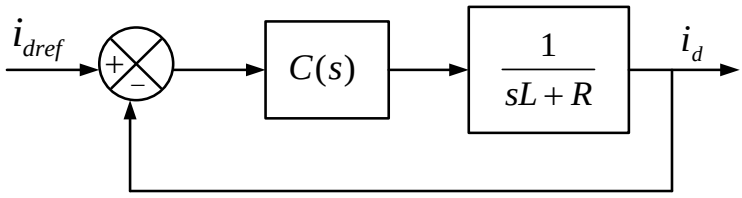

Fig.R.13 Contrôle en boucle fermée du courant de l'axe-d

La fonction de transfert en boucle fermée du système sera à la Fig. R.13:

$$G_c(s) = \frac{(sK_p + K_i)/L}{s^2 + \left(\frac{R+K_p}{L}\right)s + \frac{K_i}{L}}$$

En comparant le dénominateur avec la fonction de transfert de 2ème ordre:$s^2 + 2s\xi\omega_i + \omega_i^2$

$$K_p = 2\xi\omega_i L - R$$
$$K_i = L\omega_i^2 \qquad [\omega_i = \frac{1}{t_i} = \frac{R}{L}]$$

Même calcul pour le contrôleur de courant PI de l'axe-q.

Le contrôleur de courant R

Deux types de contrôleurs résonants doivent être conçus pour contrôler les courants de phase: le contrôleur 100Hz R pour les axes d et q et le contrôleur 50Hz R pour le composant de courant neutre.

En ce qui concerne la conception du contrôleur R de courant neutre, la contrainte est qu'il est lié au contrôleur de tension du point médian du bus DC (proportionnel). Ainsi, ils doivent être découplés de manière à ce que leurs parcelles de Bode soient comme à la Fig. R.14:

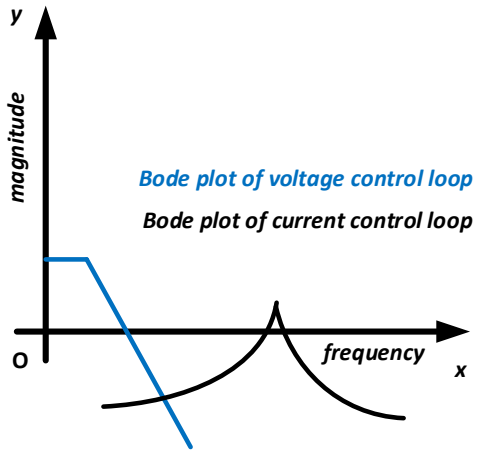

Fig.R.14 Stratégie pour découpler l'effet du contrôleur de courant de l'axe 0 et du contrôleur de tension capacitif du point central

3.3.2 Conception de contrôleur de tension

La différence de tension (dV) dans les condensateurs du bus DC a été comparée à zéro afin de la minimiser. L'erreur a été transmise par un contrôleur proportionnel. Le gain du contrôleur de tension est réglé sur une petite valeur, 0,001, de sorte que la réponse en fréquence de la boucle du contrôleur de tension ne chevauche pas la réponse en fréquence du contrôleur résonnant à 50 Hz, utilisé pour le contrôle du courant neutre.

3.4 Simulation Hardware-in-the-Loop

Dans cette stratégie, le circuit de puissance du convertisseur est toujours virtuel mais les impulsions de porte réelles sortent d'un contrôleur numérique afin de faire fonctionner un convertisseur électronique de puissance comme illustré sur la Fig. R.15.

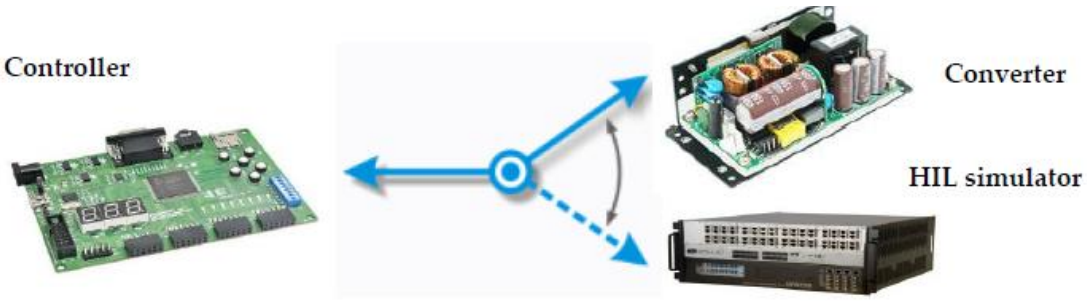

Fig.R.15 concept de simulation HIL

3.5 Résultats de la validation du modèle en boucle fermée du convertisseur NPC dans différentes conditions de fonctionnement

Les simulations Matlab / Simulink et HIL ont été réalisées pour valider la stratégie de contrôle globale du convertisseur NPC à 4 bras dans différentes conditions de fonctionnement. Mais ici, les résultats de condition d'équilibre triphasé et de transfert de puissance de déséquilibre maximal (courant neutre de 32 A r.m.s), obtenus à partir de la plate-forme Matlab/Simulink et HIL, ont été montrés. Cependant, la grandeur de tous les paramètres est réduite afin de les représenter par les bornes d'E / S du FPGA.

Dans toutes ces conditions de test, d'autres paramètres communs sont considérés comme:

Tension du bus DC = 800 V (en supposant que le bus DC est parfaitement contrôlé par la source)

Condensateurs de bus DC = 5 mF

Tension de phase du réseau AC = 230V (r.m.s)

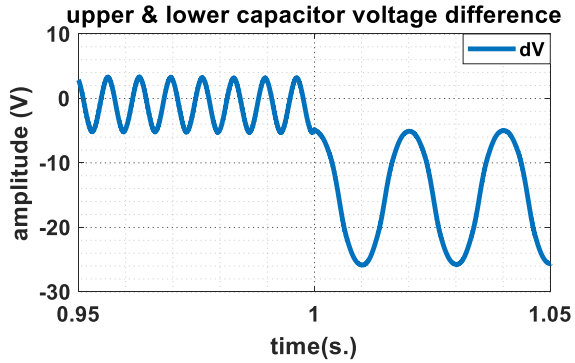

Fig. R.16 Différence de tension des tensions supérieures et inférieures des condensateurs du bus DC dans la simulation Matlab/Simulink [Condition de test: $P_a = P_b = P_c = 7kW$ and $Q_a = Q_b = Q_c = 0kVAr$ pour $tt < 1s$. $P_a = 2.3\ kW, P_b = -1.16kW, P_c = -1.16kW$ and $Q_a = 0kVAr, Q_b = -2.01kVAr, Q_c = 2.01kVAr$ pour $t \geq 1s$.*]*

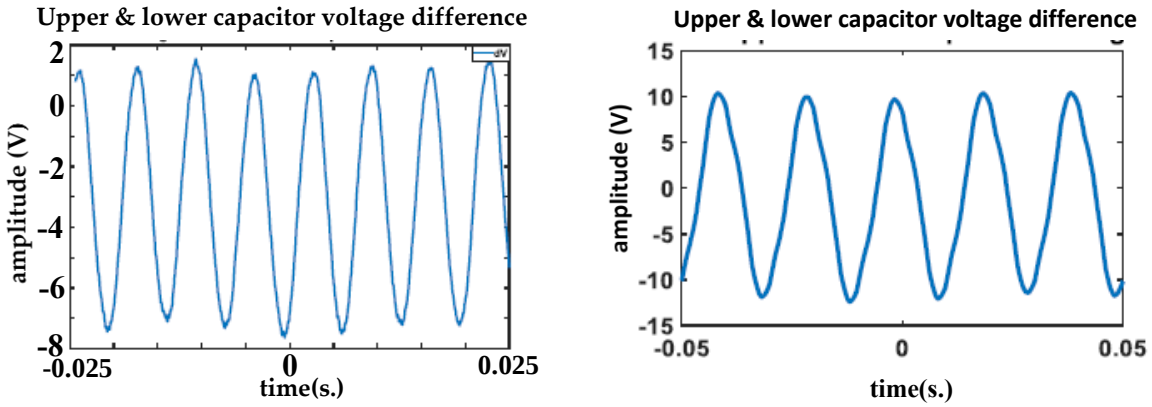

(a) *(b)*

Fig. R.17 Différence de tension des tensions supérieures et inférieures des condensateurs du bus DC dans la simulation HIL [Condition de test: (a) $P_a = P_b = P_c = 7kW$ and $Q_a = Q_b = Q_c = 0kVAr$ *(b)* $P_a = 2.3\ kW, P_b = -1.16kW, P_c = -1.16kW$ and $Q_a = 0kVAr, Q_b = -2.01kVAr, Q_c = 2.01kVAr$*]*

On observe que dans les deux conditions, la différence de tension entre ces deux tensions de condensateur du bus DC est inférieure à 5% de V_{DC}.

3.6 Méthode pour réduire davantage l'oscillation de la tension du bus DC

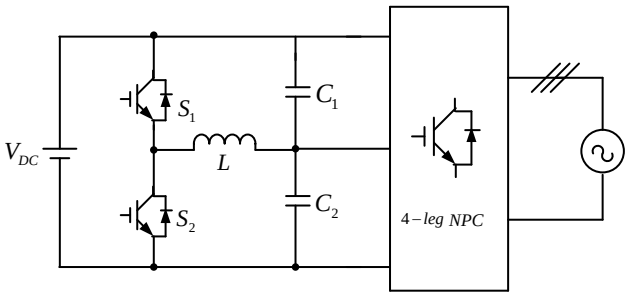

Fig. R.18 Configuration pour compenser davantage l'oscillation de la tension du bus DC

Avec cette configuration, un bras supplémentaire injectera le courant opposé au point médian du bus DC, en fonction de la différence de tension entre deux condensateurs de bus DC, ce qui réduira à son tour l'oscillation de tension par compensation de courant. Le tableau ci-dessous compare la variation de tension avec deux configurations.

Puissance active et reactive	dV avec NPC à 4 bras	dV avec NPC à 4 bras +5th bras
$P_a = 3kW\ P_b = 4kW\ P_c = 2kW \quad Q_a = Q_b = Q_c = 0\ kVAr$	±5V	±2.5V
$P_a = 2.3kW\ P_b = -1.16kW\ P_c = -1.16kW\ Q_a = 0kVAr \quad Q_b = -2.01kVAr \quad Q_c = 2.01kVAr$	±10V	±4V

Tableau R.1: Comparaison de l'oscillation de tension entre NPC à 4 bras et NPC à 4 bras + 5th bras

Cette nouvelle configuration est meilleure en termes de réduction de l'oscillation de tension du point médian capacitif qui à son tour réduit davantage la taille des condensateurs de bus DC. Cependant, une inductance basse fréquence supplémentaire, un bras supplémentaire avec deux IGBT et leurs circuits auxiliaires peuvent augmenter le volume global, le poids et les pertes du chargeur.

3.8 La conclusion

Dans ce chapitre, une stratégie de contrôle en boucle fermée avec le réglage des contrôleurs a été développée pour le convertisseur NPC à 4 bras, qui sera utilisé comme partie bidirectionnelle AC / DC du chargeur de batterie EV.

Avec la stratégie contrôlée développée, le convertisseur NPC peut fonctionner en mode quatre quadrants, comme le montre la Fig. R.19.

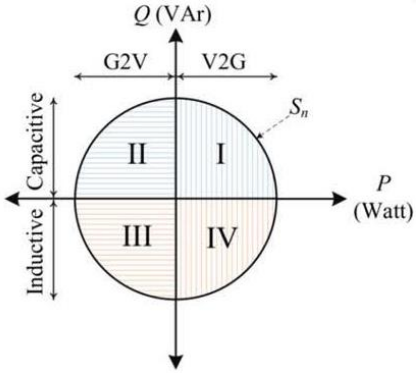

Fig. R.19 Point de fonctionnement G2V et V2G du chargeur de batterie bidirectionnel EV basé sur la puissance active et réactive de référence

Chapitre 4

4.1 L'Introduction

Pour un EV connecté au réseau, la partie électronique de puissance du chargeur de batterie comprend un convertisseur DC / DC bidirectionnel isolé, ce qui est essentiel pour l'application V2G. Cependant, un convertisseur DC / DC non isolé est moins lourd et plus simple dans sa structure qu'un convertisseur isolé et peut atteindre une meilleure efficacité, mais l'isolation galvanique dans la structure du convertisseur peut aider à résoudre les problèmes de sécurité. La configuration TAB a été choisie comme convertisseur DC/DC isolé bidirectionnel pour d'autres expériences.

4.2 Configuration du chargeur de batterie EV bidirectionnel intégré

La Fig. R.20 ci-dessous représente le chargeur de batterie bidirectionnel intégré, qui se compose d'un convertisseur NPC à 4 bras connecté avec TAB pour la conversion DC/DC. Différents échanges d'énergie entre le réseau et le chargeur et au sein du chargeur ont également été illustrés.

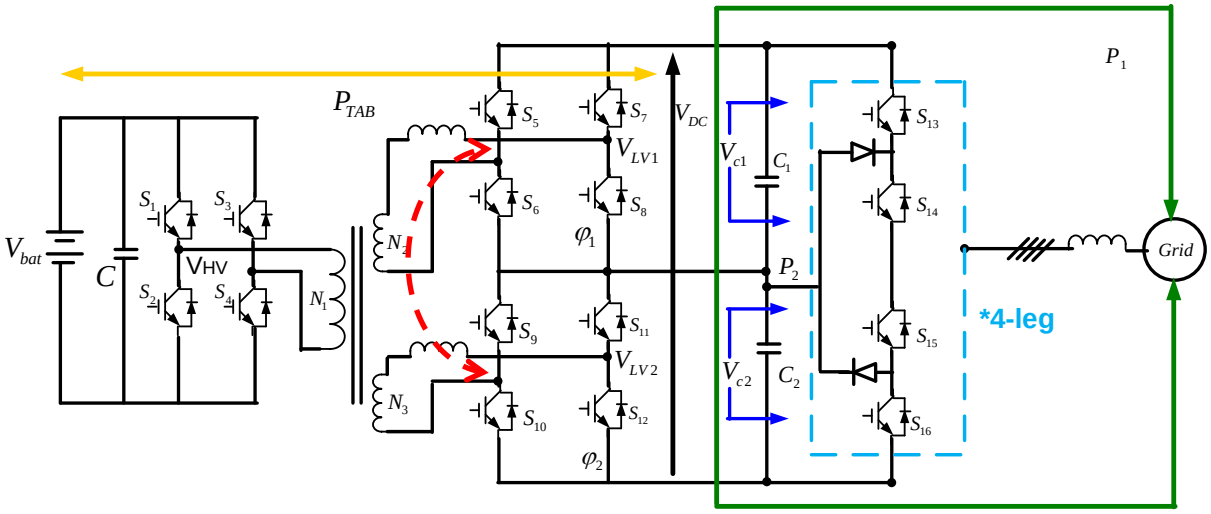

Fig. R.20 Chargeur de batterie EV intégré et flux de puissance à l'intérieur

4.3 Stratégie de contrôle pour TAB

La stratégie de contrôle du TAB doit garantir le contrôle de deux paramètres majeurs. Elles sont: 1. Une tension continue constante doit être garantie. 2. L'équilibrage de tension entre deux condensateurs de bus DC doit également être assuré.

En considérant la tension aux bornes du pont en H du côté haute tension de TAB (V_{HV}) comme référence, la Fig. R.21 représente le diagramme vectoriel de TAB. Où V_{LV1} et V_{LV2} sont les tensions aux bornes du pont en H supérieur et inférieur du côté convertisseur NPC de TAB respectivement.

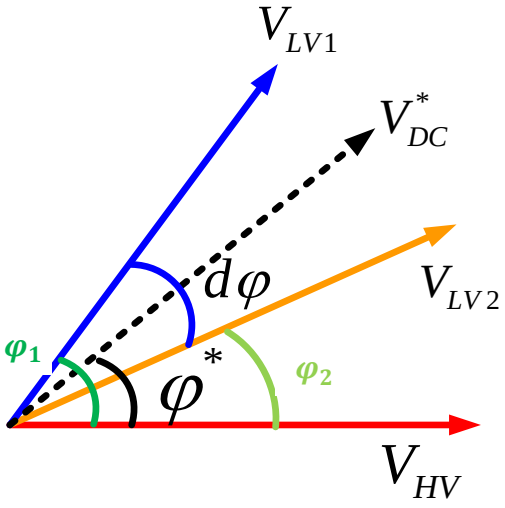

Fig. R.21 Diagramme vectoriel des tensions dans TAB

Nous allons contrôler le flux de puissance principal qui est lié à φ* et le déséquilibre de puissance entre les côtés secondaires du TAB qui est associé à dφ. De la Fig. R.21, φ_1 et φ_2 peuvent s'écrire:

$$\boldsymbol{\varphi_1 = \varphi^* + \frac{d\varphi}{2}}$$

$$\boldsymbol{\varphi_2 = \varphi^* - \frac{d\varphi}{2}}$$

Avec ces deux boucles de contrôle de *dV* et V_{DC}*, nous pouvons générer des angles de déphasage φ_1 et φ_2 qui peuvent contrôler le transfert d'énergie bidirectionnel TAB. La stratégie de contrôle globale de TAB a été illustrée sur la Fig. R.22.

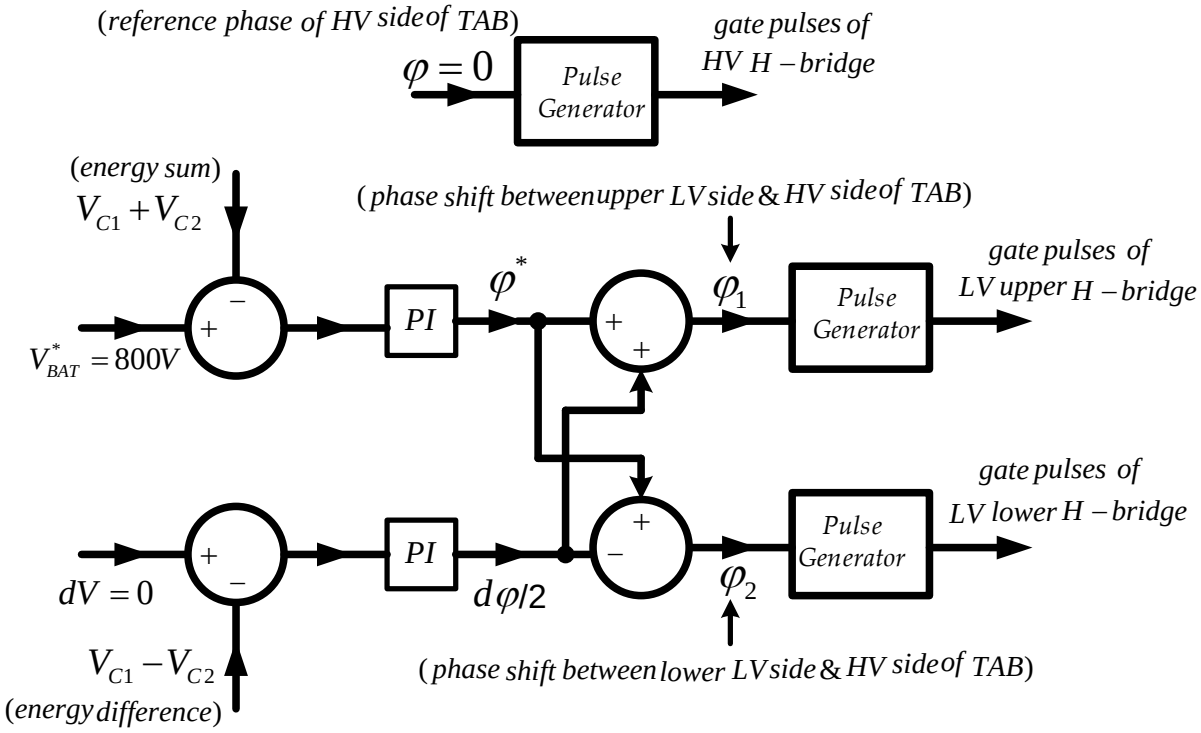

Fig. R.22 Stratégie de contrôle pour TAB

4.4 Stratégie de contrôle en boucle fermée du chargeur intégré en utilisant Matlab/Simulink avec résultats

Afin de justifier l'efficacité du convertisseur intégré de chargeur de batterie EV bidirectionnel proposé a été simulé à la fois sur les plateformes Matlab/Simulink et HIL dans des conditions d'échange de puissance à déséquilibre monophasé et triphasé (objectif principal de la thèse). Dans ce résumé français, les tensions supérieures et inférieures des condensateurs du bus DC ont été montrées pour vérifier dV ≤ 5% de V_{bat}.

$\boldsymbol{A.P_a = 7kW \;\; P_b = P_c = 0kW \qquad Q_a = Q_b = Q_c = 0kVAr}$
$\boldsymbol{B.P_a = 2.3kW \;\; P_b = -1.16kW \;\; P_c = -1.16kW \qquad Q_a = 0kVAr \;\; Q_b = -2.01kVAr \;\; Q_c = 2.01kVAr}$

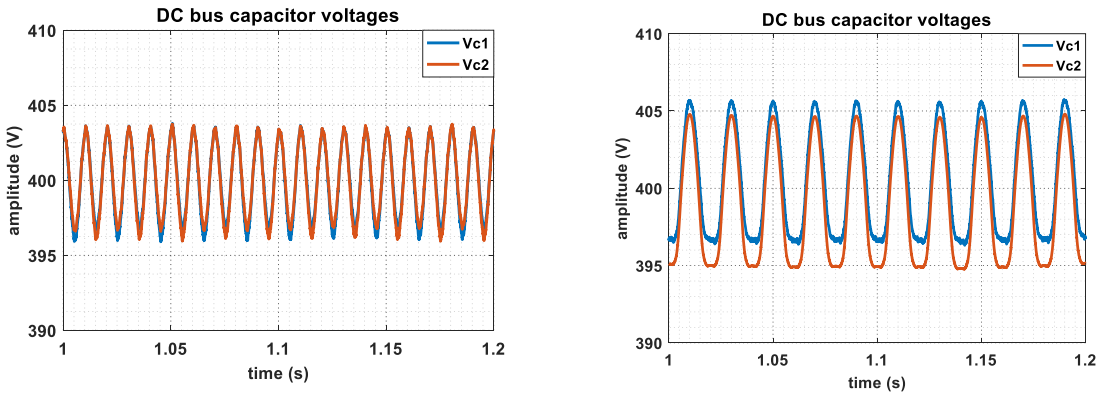

(a) *(b)*

Fig. R.23 Tensions des condensateurs du bus DC en mode AC de l'oscilloscope dans la simulation HIL a. monophasé b. Opération d'échange de puissance déséquilibrée triphasée du chargeur

4.5 La Conclusion

Grâce à tous les tests et aux résultats correspondants, on peut conclure que le chargeur de batterie embarqué bidirectionnel EV peut soutenir les objectifs de la thèse, qui sont:
a. Transfert de puissance monophasé.
b. Transfert de puissance bidirectionnel en condition de réseau triphasé équilibré.
c. Transfert de puissance bidirectionnel tout en compensant et en atténuant le déséquilibre des échanges de puissance active et réactive entre alimentation de trois phases.

Chapitre 5

5.1 L'Introduction

Les travaux, présentés dans cette thèse, concernent les exigences de l'application V2G et le développement du chargeur bidirectionnel embarqué pour les VE. Cette thèse a été réalisée avec la collaboration entre l'Institut VEDECOM et G2ELab, Université Grenoble Alpes. L'Institut VEDECOM est un Institut pour la Transition Energétique (ITE) qui œuvre dans le domaine des sources d'énergie bas carbone. Créée en 2014, elle rassemble à la fois la recherche académique (par exemple, UGA, Cetim, ESIGELEC, ESTACA etc.) et les compétences industrielles (par exemple PSA, Groupe Renault, Safran, Valeo etc.). Dans le domaine de l'électrification des véhicules et sous-domaine des systèmes de charge innovants, ces recherches ont été menées.

Dans **le Chapitre 1**, objectifs de la thèse, les topologies des parties d'électronique de puissance des chargeurs de batterie bidirectionnels EV et tous les avantages et services auxiliaires, fournis par l'application V2G, ont été discutés. Après avoir étudié les avantages et les inconvénients de différents convertisseurs AC / DC bidirectionnels, le NPC à 4 bras a été sélectionné au **Chapitre 2**. Dans le **Chapitre 3**, la stratégie de contrôle en boucle fermée du convertisseur NPC à 4 bras a été développée. Selon la stratégie de contrôle en boucle fermée développée du convertisseur NPC à 4 bras, des contrôleurs de tension et de courant ont été conçus. Avec l'aide des résultats Matlab / Simulink et HIL, la stratégie de contrôle développée a été validée. Au **Chapitre 4**, une stratégie de contrôle en boucle fermée de la configuration sélectionnée du convertisseur DC / DC bidirectionnel, qui est TAB, a été développée. Enfin, il a été validé par les résultats Matlab / Simulink.

5.2 Travaux futurs

Ci-dessous, des travaux peuvent être réalisés à l'avenir pour améliorer les objectifs de cette thèse:

1. Point de test avec le plus mauvais déséquilibre.
2. Optimisation des éléments passifs du convertisseur.
3. Test expérimental des stratégies de contrôle développées.
4. Étude d'autres types de structures de convertisseurs bidirectionnels AC/DC.

BIBLIOGRAPHY

[1] A. R. Dinde and S. R. Jagtap, "Maximum Power Point Tracking photovoltaic system for PWM inverter," *2015 International Conference on Computation of Power, Energy, Information and Communication (ICCPEIC)*, Chennai, 2015, pp. 0028-0032.

[2] R. Matsuo and H. Miwa, "Grid-Connected Electric-Power Control Algorithm for Promoting the Introduction of Renewable Energy," 2014 International Conference on Intelligent Networking and Collaborative Systems, Salerno, 2014, pp. 163-168.

[3] D. Bai, H. Cao and L. Wang, "Research and simulation of V2G technology in micro grid," 2016 China International Conference on Electricity Distribution (CICED), Xi'an, 2016, pp. 1-5.

[4] H. Turker, S. Bacha and D. Chatroux, "Impact of Plug-in Hybrid Electric Vehicles (PHEVs) on the French electric grid," *2010 IEEE PES Innovative Smart Grid Technologies Conference Europe (ISGT Europe)*, 2010, pp. 1-8, doi: 10.1109/ISGTEUROPE.2010.5638948.

[5] A. Juton, X. Rain, V. Sauvant-Moynot, F. Orsini, C. Saber, S. Bacha, O. Béthoux, E. Labouré, "Technologies des voitures électriques: Motorisations, batteries, hydrogène, recharge et interactions réseau. ISBN: 2100818066, Dunod, Edition: May, 2021.

[6] T. Shiramagond and W. Lee, "Integration of Renewable Energy into Electric Vehicle Charging Infrastructure," 2018 IEEE International Smart Cities Conference (ISC2), Kansas City, MO, USA, 2018, pp. 1-7.

[7] W. Jian, L. Zhizhen, W. Kuihua, W. Feng and Z. Yi, "Impact of plug-in hybrid electric vehicles on power distribution networks," 2011 4th International Conference on Electric Utility Deregulation and Restructuring and Power Technologies (DRPT), Weihai, Shandong, 2011, pp. 1618-1622.

[8] N. Koduri, S. Kumar and R. Y. Udaykumar, "On-board Vehicle-to-Grid (V2G) integrator for power transaction in smart grid environment," 2014 IEEE International Conference on Computational Intelligence and Computing Research, Coimbatore, 2014, pp. 1-4.

[9] A. Ovalle, A. Hably, S. Bacha and M. Ahmed, "Voltage support by optimal integration of plug-in hybrid electric vehicles to a residential grid," *IECON 2014 - 40th Annual Conference of the IEEE Industrial Electronics Society*, 2014, pp. 4430-4436, doi: 10.1109/IECON.2014.7049169.

[10] P. Kong and G. K. Karagiannidis, "Charging Schemes for Plug-In Hybrid Electric Vehicles in Smart Grid: A Survey," in *IEEE Access*, vol. 4, pp. 6846-6875, 2016.

[11] Chan, C. C. The state of the art of electric, hybrid, and fuel cell vehicles. *Proc. IEEE* **95**, 704–718 (2007).

[12] "Plug-in Fuel Cell Vehicle Technology and Value Analysis Phase 1; Preliminary Findings and Plan for Detailed Study", EPRI, Palo Alto, CA: 2010.1021482.

[13] B. Wahono, W.B. Santoso, A. Nur, Amina, "Analysis of range extender electric vehicle performance using vehicle simulator," 2nd International Conference on Sustainable Energy Engineering and Application, ICSEEA 2014.

[14] IEA, Electric car deployment in selected countries, 2013-2018, IEA, Paris https://www.iea.org/data-and-statistics/charts/electric-car-deployment-in-selected-countries-2013-2018.

[15] H. Turker, S. Bacha, D. Chatroux and A. Hably, "Modelling of system components for Vehicle-to-Grid (V2G) and Vehicle-to-Home (V2H) applications with Plug-in Hybrid Electric Vehicles (PHEVs)," *2012 IEEE PES Innovative Smart Grid Technologies (ISGT)*, 2012, pp. 1-8, doi: 10.1109/ISGT.2012.617565

[16] I. Subotic, N. Bodo, E. Levi, B. Dumnic, D. Milicevic and V. Katic, "Overview of fast on-board integrated battery chargers for electric vehicles based on multiphase machines and power electronics," in *IET Electric Power Applications*, vol. 10, no. 3, pp. 217-229, 3 2016.

[17] Lessons Learned on Early EV Fast-Charging Deployments https://www.theicct.org/sites/default/files/publications/ZEV_fast_charging_white_paper_final.pdf

[18] A. Khaligh and S. Dusmez, "Comprehensive Topological Analysis of Conductive and Inductive Charging Solutions for Plug-In Electric Vehicles," in *IEEE Transactions on Vehicular Technology*, vol. 61, no. 8, pp. 3475-3489, Oct. 2012.

[19] https://circuitdigest.com/article/electric-vehicle-on-board-chargers-and-charging-stations

[20] https://www.renault.fr/vehicules-electriques/zoe/batterie-recharge.html

[21] C. Liu, C. Jiang and C. Qiu, "Overview of coil designs for wireless charging of electric vehicle," *2017 IEEE PELS Workshop on Emerging Technologies: Wireless Power Transfer (WoW)*, Chongqing, 2017, pp. 1-6.

[22] S. S. Hosseini, A. Badri and M. Parvania, "The plug-in electric vehicles for power system applications: The vehicle to grid (V2G) concept," *2012 IEEE International Energy Conference and Exhibition (ENERGYCON)*, Florence, 2012, pp. 1101-1106.

[23] H. Turker and S. Bacha, "Optimal Minimization of Plug-In Electric Vehicle Charging Cost With Vehicle-to-Home and Vehicle-to-Grid Concepts," in *IEEE Transactions on Vehicular Technology*, vol. 67, no. 11, pp. 10281-10292, Nov. 2018, doi: 10.1109/TVT.2018.2867428.

[24] M. Pahlevaninezhad, J. Drobnik, P. K. Jain and A. Bakhshai, "A Load Adaptive Control Approach for a Zero-Voltage-Switching DC/DC Converter Used for Electric Vehicles," in *IEEE Transactions on Industrial Electronics*, vol. 59, no. 2, pp. 920-933, Feb. 2012.

[25] D. C. Erb, O. C. Onar and A. Khaligh, "Bi-directional charging topologies for plug-in hybrid electric vehicles," *2010 Twenty-Fifth Annual IEEE Applied Power Electronics Conference and Exposition (APEC)*, Palm Springs, CA, 2010, pp. 2066-2072.

[26] V. Nguyen, T. Tran-Quoc and S. Bacha, "Harmonic distortion mitigation for electric vehicle fast charging systems," *2013 IEEE Grenoble Conference*, 2013, pp. 1-6, doi: 10.1109/PTC.2013.6652435.

[27] B. LEE, J. LEE and D. KANG, "An Isolated PFC Converter with Harmonic Modulation Technique for EV Chargers," *2018 International Power Electronics Conference (IPEC-Niigata 2018 -ECCE Asia)*, Niigata, 2018, pp. 3030-3033.

[28] Y. Du, X. Zhou, S. Bai, S. Lukic and A. Huang, "Review of non-isolated bi-directional DC-DC converters for plug-in hybrid electric vehicle charge station application at municipal parking decks," *2010 Twenty-Fifth Annual IEEE Applied Power Electronics Conference and Exposition (APEC)*, Palm Springs, CA, 2010, pp. 1145-1151.

[29] K. K. Monfared, H. Iman-Eini and R. Razi, "Control of Single-Phase Bidirectional PEV/EV Charger Based on FCS-MPC Method for V2G Reactive Power Operation," *2019 10th International Power Electronics, Drive Systems and Technologies Conference (PEDSTC)*, Shiraz, Iran, 2019, pp. 641-646.

[30] S. Y. R. Hui, H. Chung and S. C. Yip, "A bi-directional AC-DC power converter with power factor correction," *PESC 98 Record. 29th Annual IEEE Power Electronics Specialists Conference (Cat. No.98CH36196)*, Fukuoka, 1998, pp. 1323-1329 vol.2.

[31] J. Rodriguez, Jih-Sheng Lai and Fang Zheng Peng, "Multilevel inverters: a survey of topologies, controls, and applications," in *IEEE Transactions on Industrial Electronics*, vol. 49, no. 4, pp. 724-738, Aug. 2002.

[32] N. Bhowmick, D. Frey, S. Bacha, M. Debbou and F. Colet, "A Comparative Study of Capacitive Middle Point Voltage Oscillations for 3 Phase 2-Level and 3-Level Converters in Unbalanced Current Injection," *2017 IEEE Vehicle Power and Propulsion Conference (VPPC)*, 2017, pp. 1-6, doi: 10.1109/VPPC.2017.8331033.

[33] O. Husev, C. Roncero-Clemente, E. Romero-Cadaval, D. Vinnikov and S. Stepenko, "Single phase three-level neutral-point-clamped quasi-Z-source inverter," in *IET Power Electronics*, vol. 8, no. 1, pp. 1-10, 1 2015.

[34] K. Fahem, D. E. Chariag and L. Sbita, "On-board bidirectional battery chargers topologies for plug-in hybrid electric vehicles," *2017 International Conference on Green Energy Conversion Systems (GECS)*, Hammamet, 2017, pp. 1-6.

[35] B. Singh, B. N. Singh, A. Chandra, K. Al-Haddad, A. Pandey and D. P. Kothari, "A review of single-phase improved power quality AC-DC converters," in *IEEE Transactions on Industrial Electronics*, vol. 50, no. 5, pp. 962-981, Oct. 2003.

[36] D. Yadeo, P. Chaturvedi and S. K. Saketi, "A New Five Level Dual Active Bridge DC-DC Converter for Solid State Transformer," *2018 IEEE International Conference on Power Electronics, Drives and Energy Systems (PEDES)*, Chennai, India, 2018, pp. 1-5.

[37] B. Zhao, Q. Song, W. Liu and Y. Sun, "Overview of Dual-Active-Bridge Isolated Bidirectional DC–DC Converter for High-Frequency-Link Power-Conversion System," in *IEEE Transactions on Power Electronics*, vol. 29, no. 8, pp. 4091-4106, Aug. 2014.

[38] A. Safaee, P. Jain and A. Bakhshai, "Time-domain analysis of a wide-range dual-active-bridge bidirectional series resonant converter," *IECON 2015 - 41st Annual Conference of the IEEE Industrial Electronics Society*, Yokohama, 2015, pp. 004139-004145.

[39] A. Ovalle, A. Hably, S. Bacha, G. Ramos and J. M. Hossain, "Escort Evolutionary Game Dynamics Approach for Integral Load Management of Electric Vehicle Fleets," in *IEEE Transactions on Industrial Electronics*, vol. 64, no. 2, pp. 1358-1369, Feb. 2017, doi: 10.1109/TIE.2016.2615042.

[40] https://v2g-clarity.com/knowledgebase/vehicle-to-grid/

[41] P. Frias, T. Gomez and D. Soler, "A Reactive Power Capacity Market Using Annual Auctions," in *IEEE Transactions on Power Systems*, vol. 23, no. 3, pp. 1458-1468, Aug. 2008.

[42] C. Wu, H. Mohsenian-Rad, J. Huang and A. Y. Wang, "Demand side management for Wind Power Integration in microgrid using dynamic potential game theory," *2011 IEEE GLOBECOM Workshops (GC Wkshps)*, Houston, TX, 2011, pp. 1199-1204.

[43] Mounir Marzouk. Développement de chargeurs intégrés pour véhicules hybrides plug-in. Energie électrique. Université Grenoble Alpes, 2015. Français. ⟨NNT : 2015GREAT088⟩. ⟨tel-01239349⟩

[44] J. A. Fernandez, S. Bacha, D. Riu and A. Hably, "Plug-in electric vehicle collaborative charging for current unbalance minimization: Ant system optimization application," *2015 IEEE International Conference on Industrial Technology (ICIT)*, 2015, pp. 2686-2691, doi: 10.1109/ICIT.2015.7125494.

[45] J. Fernandez, S. Bacha, D. Riu, H. Turker and M. Paupert, "Current unbalance reduction in three-phase systems using single phase PHEV chargers," *2013 IEEE International Conference on Industrial Technology (ICIT)*, 2013, pp. 1940-1945, doi: 10.1109/ICIT.2013.6505975.

[46] P. Frias, T. Gomez and D. Soler, "A Reactive Power Capacity Market Using Annual Auctions," in *IEEE Transactions on Power Systems*, vol. 23, no. 3, pp. 1458-1468, Aug. 2008.

[47] C. Wu, H. Mohsenian-Rad, J. Huang and A. Y. Wang, "Demand side management for Wind Power Integration in microgrid using dynamic potential game theory," *2011 IEEE GLOBECOM Workshops (GC Wkshps)*, Houston, TX, 2011, pp. 1199-1204.

[48] M. H. Albadi, A. S. A. Hinai, A. H. Al-Badi, M. S. A. Riyami, S. M. A. Hinai and R. S. A. Abri, "Unbalance in power systems: Case study," *2015 IEEE International Conference on Industrial Technology (ICIT)*, Seville, 2015, pp. 1407-1411.

[49] H. Dehghani Tafti *et al.*, "Study on the unbalanced current injection capability of grid-connected photovoltaic neutral-point-clamped inverter," *2016 IEEE Energy Conversion Congress and Exposition (ECCE)*, Milwaukee, WI, 2016, pp. 1-6.

[50] Battery Electric Vehicles vs. Internal Combustion Engine Vehicles http://www.adlittle.cn/sites/default/files/viewpoints/ADL_BEVs_vs_ICEVs_FINAL_November_292016.pdf.

[51] How long does it takes to charge an electric car? https://pod-point.com/guides/driver/how-long-to-charge-an-electric-car.

[52] Lliuyacca, R., Mauricioa, J. M., Gomez-Exposito, A., Savaghebi, M., & Guerrero, J. M.," Grid-forming VSC control in four-wire systems with unbalanced nonlinear loads". Electric Power Systems Research, 152, 249-256, 2017.

[53] D. Sreenivasarao, Pramod Agarwal, Biswarup Das, "Neutral current compensation in three-phase, four-wire systems: A review" Electric Power System Research, Volume 86, Pages: 1743–1753, Jan. 2012.

[54] M. Debbou, D. Frey, N. Bhowmick, F. Collet and S. Bacha, "Convertisseur NPC Quatre Bras pour les Véhicules électriques et Chargeur bidirectionnel comprenant une tel convertisseur", INPI [B7] WO2019186078A1 (A1), 2019.

[55] Weilun Warren Chen, "Bidirectional Three-phase AC-DC Power Conversion using DC-DC Converters and a Three-phase Unfolder," *PhD Thesis*, Utah State University, 2017.

[56] R.H. Baker and L.H. Bannister, 'Electric Power Converter,' U.S Patent 3 867 643, Feb, 1975.

[57] Ebrahim Babaei, Mohammad Farhadi Kangarlu, Farshid Najaty Mazgar, "Symmetric and asymmetric multilevel inverter topologies with reduced switching devices", Electric Power System Research, Vol. 86, pp122-130, 2012.

[58] L. M. Tolbert, F. Z. Peng, "Multilevel inverters for large automotive drives," All Electric Combat Vehicle Second International conference, pp. 209-214, June 8-12, 1997, Dearborn, Michigan.

[59] O. Husev et al., "Comparison of Impedance-Source Networks for Two and Multilevel Buck–Boost Inverter Applications," in IEEE Transactions on Power Electronics, vol. 31, no. 11, pp. 7564-7579, Nov. 2016.

[60] P. Enjeti and R. Jakkli, "Optimal power control strategies for neutral point clamped (NPC) inverter topology," Conference Record of the IEEE Industry Applications Society Annual Meeting, San Diego, CA, USA, 1989, pp. 924-930 vol.1.

[61] J. Rodriguez, J. S. Lai, and F. Z. Peng, "Multilevel inverters: A survey of topologies, controls and applications," IEEE Transactions of Industrial Electronics, vol.49, no. 4, pp. 724-738, Aug. 2002.

[62] A. Salem, E.M. Ahmed, M. Orabi and M. Ahmed, "Study and analysis of new three-phase modular multilevel inverter," in IEEE Transactions on Industrial Electronics, vol. 63, no. 12, pp 7804-7813, Dec. 2016.

[63] Rahim, N.A., Selvaraj, J., 'Multistring five-level inverter with novel PWM control scheme for PV application', IEEE Trans. Ind. Electron., 2010,57, (6), pp. 2111-2123.

[64] Banaei, M.R., Salary, E., 'New multilevel inverter with reduction of switches and gate driver', Energy Convers. Manage., 2011, 52, pp.1129-1136.

[65] Nisith Bhowmick, David Frey, Seddik Bacha, Mustapha Debbou, François Colet, "Evaluation des ondulations de tension au point milieu capacitif pour les convertisseurs à deux et à trois niveaux, " Symposium de Génie Electrique, Jul 2018, Nancy, France.

[66] Mohan, N., Undeland, T., and Robbins, W., Power Electronics Converters, Applications and Design, 2nd ed., New York: John Wiley & Sons, pp. 172–178, 1995.

[67] U. P. Yagnik and M. D. Solanki, "Comparison of L, LC & LCL filter for grid connected converter," *2017 International Conference on Trends in Electronics and Informatics (ICEI)*, Tirunelveli, 2017, pp. 455-458.

[68] Mounir Marzouk. Développement de chargeurs intégrés pour véhicules hybrides plug-in. Energie électrique. Université Grenoble Alpes, 2015. Français. NNT: 2015GREAT088. Tel-01239349.

[69] D. Ocnasu, S. Bacha, I. Munteanu, C. Dufour and D. Roye, "Real-time power-hardware-in-the-loop facility for shunt and serial power electronics benchmarking," *2009 13th European Conference on Power Electronics and Applications*, 2009, pp. 1-7.

[70] S. Calligaro, F. Pasut, R. Petrella and A. Pevere, "Modulation techniques for three-phase three-level NPC inverters: A review and a novel solution for switching losses reduction and optimal neutral-point balancing in photovoltaic applications," *2013 Twenty-Eighth Annual IEEE Applied Power Electronics Conference and Exposition (APEC)*, Long Beach, CA, 2013, pp. 2997-3004.

[71] Bin Wu, “High Power Converters and AC drives” Pg. no. 131-139, *A John Wiley & Sons, Inc., Publication.*

[72] Jayant J. Mane, Shubhada P. Muley, Mohan V. Aware “Performance of 5-level NPC inverter with Multi-Multicarrier Multi-Modulation technique", *2012 IEEE International Conference on Power Electronics, Drives and Energy Systems,* December16-19, 2012, Bengaluru.

[73] G. J. Rushiraj and P. N. Kapil, "Analysis of different modulation techniques for multilevel inverters," *2016 International Conference on* Electrical, *Electronics, and Optimization Techniques (ICEEOT)*, Chennai, 2016, pp. 3017-3024.

[74] R. Rojas, T. Ohnishi and T. Suzuki, "Neutral-point-clamped inverter with improved voltage waveform and control range," *Proceedings of IECON '93 - 19th Annual Conference of IEEE Industrial Electronics*, Maui, HI, USA, 1993, pp. 1240-1245 vol.2.

[75] A. Sahli, F. Krim and A. Belaout, "Energy Management and Power Quality Improvement in Grid-Connected Photovoltaic Systems," *2017 International Renewable and Sustainable Energy Conference (IRSEC)*, Tangier, 2017, pp. 1-7.

[76] A. Mortezaei, M. G. Simões, T. D. C. Busarello, F. P. Marafão and A. Al-Durra, "Grid-Connected Symmetrical Cascaded Multilevel Converter for Power Quality Improvement," in *IEEE Transactions on Industry Applications*, vol. 54, no. 3, pp. 2792-2805, May-June 2018.

[77] A. Kulkarni and V. John, "Mitigation of Lower Order Harmonics in a Grid-Connected Single-Phase PV Inverter," in *IEEE Transactions on Power Electronics*, vol. 28, no. 11, pp. 5024-5037, Nov. 2013.

[78] “IEEE standard for interconnecting distributed resources with electric power systems,” *IEEE Std. 1547-2003, 2003.*

[79] “Characteristics of the utility interface for photovoltaic systems,” *IEC Std 61727:2004, Dec. 2004.*

[80] K. Zhou, Z. Qiu, N. R. Watson and Y. Liu, "Mechanism and elimination of harmonic current injection from single-phase grid-connected PWM converters," in *IET Power Electronics*, vol. 6, no. 1, pp. 88-95, Jan. 2013.

[81] S. Chen, Y. M. Lai, S. -. Tan and C. K. Tse, "Analysis and design of repetitive controller for harmonic elimination in PWM voltage source inverter systems," in *IET Power Electronics*, vol. 1, no. 4, pp. 497-506, December 2008.

[82]Y. Wang, X. Chen, Y. Zhang, J. Chen and C. Gong, "Impedance Influence Analysis of Phase-Locked Loops on Three-Phase Grid-Connected Inverters," *2018 International Power Electronics Conference (IPEC-Niigata 2018 -ECCE Asia)*, Niigata, 2018, pp. 1177-1182.

[83] M. Boyra, J. L. Thomas, “A review on synchronization methods for grid-connected three-phase VSC under unbalanced and distorted conditions,” *in Proc. European Conf. on Power Electron. and Appli., 2011, pp. 1-10.*

[84] T. Sreekumar and K. S. Jiji, "Comparison of Proportional-Integral (P-I) and Integral-Proportional (I-P) controllers for speed control in vector controlled induction Motor drive," *2012 2nd International Conference on Power, Control and Embedded Systems*, Allahabad, 2012, pp. 1-6.

[85] S. K. Chung, "Phase-locked loop for grid-connected three-phase power conversion systems," in *IEEE Proceedings - Electric Power Applications*, vol. 147, no. 3, pp. 213-219, May 2000.

[86] M. Debbou, D. Frey, S. Bacha and N. Bhowmick, “Contrôleur de commande de convertisseur électrique et convertisseur électrique, notamment pour une intégration dans un véhicule électrique”, INPI [B9] WO2020188189 (A1), 2020.

[87] I. Etxeberria-Otadui, A. Lopez De Heredia, H. Gaztanaga, S. Bacha and M. R. Reyero, "A Single Synchronous Frame Hybrid (SSFH) Multifrequency Controller for Power Active Filters," in *IEEE Transactions on Industrial Electronics*, vol. 53, no. 5, pp. 1640-1648, Oct. 2006, doi: 10.1109/TIE.2006.881994.

[88] I. Etxeberria-Otadui, U. Viscarret, M. Caballero, A. Rufer and S. Bacha, "New Optimized PWM VSC Control Structures and Strategies Under Unbalanced Voltage Transients," in *IEEE Transactions on Industrial Electronics*, vol. 54, no. 5, pp. 2902-2914, Oct. 2007, doi: 10.1109/TIE.2007.901373.

[89] N. Golbon, G. Moschopoulos and S. A. Khajehoddin, "A control strategy for a solar grid-connected inverter," *2013 26th IEEE Canadian Conference on Electrical and Computer Engineering (CCECE)*, Regina, SK, 2013, pp. 1-4.

[90] Seddik Bacha, Iulian Munteanu, Antoneta Iuliana Bratcu, *et al.* Power electronic converters modeling and control. *Advanced textbooks in control and signal processing*, 2014, vol. 454, p. 454.

[91] Chabakata Mahamat, Mickaël Petit, François Costa, Rym Marouani, Abdelkader Mami," Balanced Active and Reactive Control Applied to a Grid Connected Five Level Inverter," *International journal of advanced computer science and applications (IJACSA), The Science and Information Organization, 2017*, 8 (10), pp.207-216.

[92] Lliuyacca, R., Mauricioa, J. M., Gomez-Exposito, A., Savaghebi, M., & Guerrero, J. M. "Grid-forming VSC control in four-wire systems with unbalanced nonlinear loads," *Electric Power Systems Research*, 2017, 152, 249-256.

[93] A. L. de Heredia, H. Gaztanaga, I. Etxeberria-Otadui, S. Bacha and X. Guillaud, "Analysis of Multi-Resonant Current Control Structures and Tuning Methods," *IECON 2006 - 32nd Annual Conference on IEEE Industrial Electronics*, 2006, pp. 2156-2161, doi: 10.1109/IECON.2006.347276.

[94] PS. Kumar and CL. Reddy, "A New Control Method for Balancing of DC-Link Voltage and Elimination of Common Mode Voltage in Multi-level Inverters," *National Power Systems Conference (NPSC)*, Kanpur, 2012.

[95] C. Graf, J. Maas, T. Schulte and J. Weise-Emden, "Real-time HIL-simulation of power electronics," *2008 34th Annual Conference of IEEE Industrial Electronics*, Orlando, FL, 2008, pp. 2829-2834.

[96] Fan Ji, Hongtao Fan and Yaojie Sun, "Modelling a FPGA-based LLC converter for real-time hardware-in-the-loop (HIL) simulation," *2016 IEEE 8th International Power Electronics and Motion Control Conference (IPEMC-ECCE Asia)*, Hefei, 2016, pp. 1016-1019.

[97] A. Florescu, S. Bacha, A. Rumeau, I. Munteanu and A. I. Bratcu, "PHIL simulation for validating power management strategies in all-electric vehicles," *2013 15th European Conference on Power Electronics and Applications (EPE)*, 2013, pp. 1-6, doi: 10.1109/EPE.2013.6634712.

[98] A. Zama, A. Benchaib, S. Bacha, D. Frey and S. Silvant, "High Dynamics Control for MMC Based on Exact Discrete-Time Model With Experimental Validation," in *IEEE Transactions on Power Delivery*, vol. 33, no. 1, pp. 477-488, Feb. 2018, doi: 10.1109/TPWRD.2017.2707343.

[99] *https://www.opal-rt.com/hardware-in-the-loop/*

[100] Y. Song, U. K. Madawala, D. J. Thrimawithana and M. Vilathgamuwa, "Three-phase bi-directional wireless EV charging system with high tolerance to pad misalignment," in *IET Power Electronics*, vol. 12, no. 10, pp. 2697-2705, 28 8 2019.

[101] Y. Liu, U. K. Madawala, R. Mai and Z. He, "A New Bi-directional Wireless EV Charging Controller Tolerant to Large Pad Misalignments," *2019 IEEE Energy Conversion Congress and Exposition (ECCE)*, Baltimore, MD, USA, 2019, pp. 3363-3367.

[102] R. Zgheib, I. Kamwa and K. Al-Haddad, "Comparison between isolated and non-isolated DC/DC converters for bidirectional EV chargers," *2017 IEEE International Conference on Industrial Technology (ICIT)*, Toronto, ON, 2017, pp. 515-520.

[103] Hamid R. Karshenas, Hamid Daneshpajooh, Alireza Safaee, Praveen Jain and Alireza Bakhshai, "Bidirectional DC - DC Converters for Energy Storage Systems, Energy Storage in the Emerging Era of Smart Grids", *2011 Prof. Rosario Carbone (Ed.)*, ISBN: 978-953-307-269-2

[104] R. W. A. A. De Doncker, D. M. Divan and M. H. Kheraluwala, "A three-phase soft-switched high-power-density DC/DC converter for high-power applications," in *IEEE Transactions on Industry Applications*, vol. 27, no. 1, pp. 63-73, Jan.-Feb. 1991.

[105] M. Neubert, A. Gorodnichev, J. Gottschlich and R. W. De Doncker, "Performance analysis of a triple-active bridge converter for interconnection of future dc-grids," *2016 IEEE Energy Conversion Congress and Exposition (ECCE)*, Milwaukee, WI, 2016, pp. 1-8.